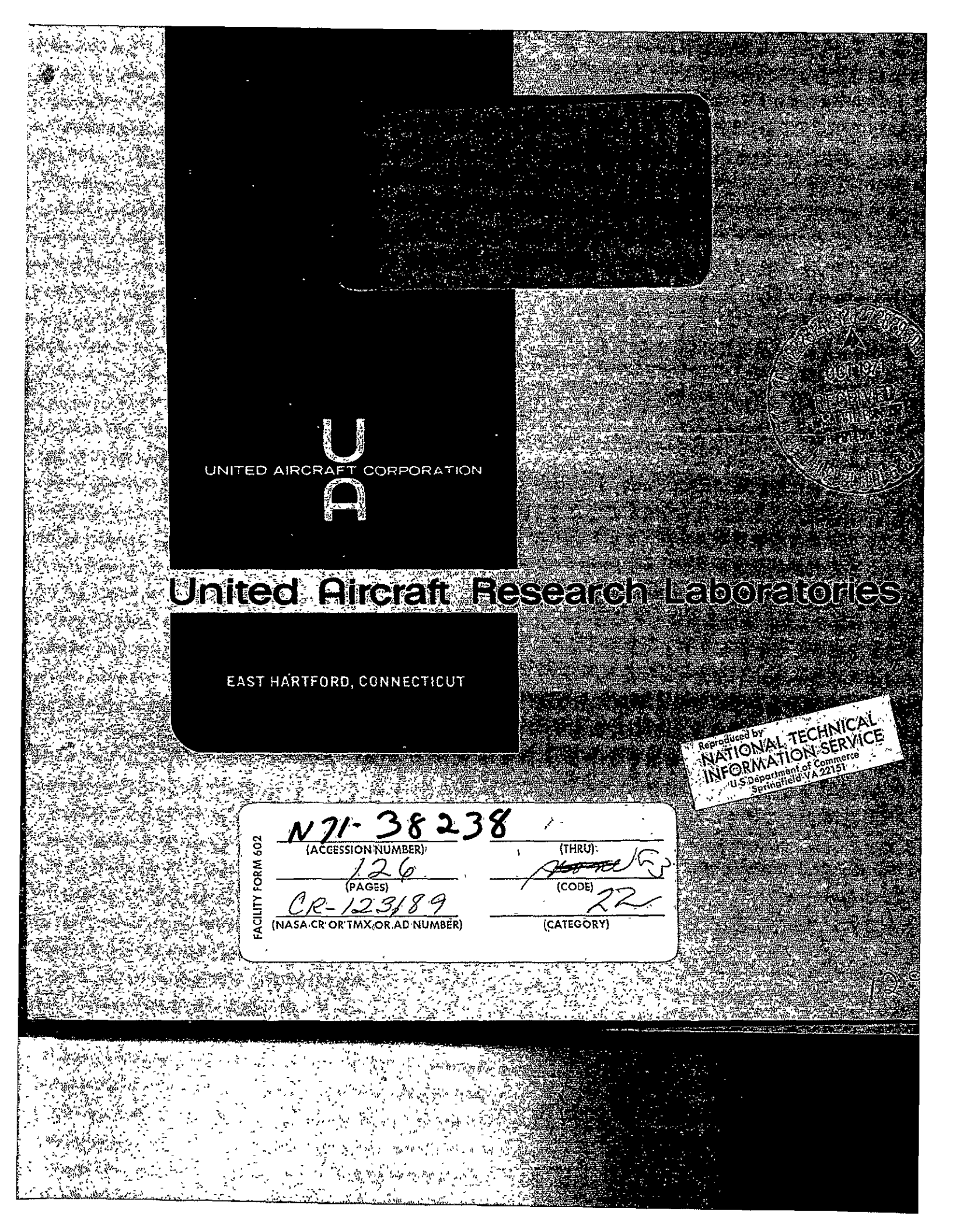
UNITED AIRCRAFT CORPORATION
United Aircraft Research Laboratories
EAST HARTFORD, CONNECTICUT
Reproduced by
NATIONAL TECHNICAL
INFORMATION SERVICE
U.S. Department of Commerce
Springfield VA 22151
FACILITY FORM 602
N71-38238
(ACCESSION NUMBER)
126
(PAGES)
CR-123189
(NASA CR OR TMX OR AD NUMBER)
(THRU)
(CODE)
22
(CATEGORY)

United Aircraft Research Laboratories

UNITED AIRCRAFT CORPORATION

EAST HARTFORD, CONNECTICUT 06108

K-910900-10

Analytical Studies of Nuclear Light Bulb Engine Radiant Heat Transfer and Performance Characteristics

NASA Contract No. SNPC-70

REPORTED BY Richard J. Rodgers

Richard J. Rodgers

Thomas S. Latham

Thomas S. Latham

Harold E. Bauer

Harold E. Bauer

APPROVED BY James W. Clark

James W. Clark, Chief
Fluid and Systems Dynamics

DATE September 1971

NO. OF PAGES 126

COPY NO. 20

FOREWORD

An exploratory experimental and theoretical investigation of gaseous nuclear rocket technology is being conducted by the United Aircraft Research Laboratories under Contract SNPC-70 with the joint AEC-NASA Space Nuclear Systems Office. The Technical Supervisor of the Contract for NASA was Captain C. E. Franklin (USAF) for the first portion of the contract performance period and was Dr. Karlheinz Thom for the last portion of the contract performance period. Results obtained during the period September 16, 1970 and September 15, 1971 are described in the following seven reports (including the present report) which comprise the required second Interim Summary Technical Report under the Contract:

1. Roman, W. C. and J. F. Jaminet: Experimental Investigations to Simulate the Thermal Environment and Fuel Region in Nuclear Light Bulb Reactors Using an R-F Radiant Energy Source. United Aircraft Research Laboratories Report K-910900-7, September 1971.

2. Klein, J. F.: Experiments to Simulate Heating of the Propellant in a Nuclear Light Bulb Engine Using Thermal Radiation from a D-C Arc Radiant Energy Source. United Aircraft Research Laboratories Report K-910900-8, September 1971.

3. Bauer, H. E.: Initial Experiments to Investigate Condensation of Flowing Metal-Vapor/Heated-Gas Mixtures in a Duct. United Aircraft Research Laboratories Report K-910900-9, September 1971.

4. Rodgers, R. J., T. S. Latham and H. E. Bauer: Analytical Studies of Nuclear Light Bulb Engine Radiant Heat Transfer and Performance Characteristics. United Aircraft Research Laboratories Report K-910900-10, September 1971. (present report)

5. Latham, T. S. and H. E. Bauer: Analytical Design Studies of In-Reactor Tests of a Nuclear Light Bulb Unit Cell. United Aircraft Research Laboratories Report K-910900-11, September 1971.

6. Krascella, N. L.: Spectral Absorption Coefficients of Helium and Neon Buffer Gases and Nitric Oxide-Oxygen Seed Gas Mixture. United Aircraft Research Laboratories Report K-910904-2, September 1971.

7. Palma, G. E. and R. M. Gagosz: Effect of 1.5 Mev Electron Irradiation on the Transmission of Optical Materials. United Aircraft Research Laboratories Report K-990929-2, September 1971.

Report K-910900-10

Analytical Studies of Nuclear Light Bulb Engine

Radiant Heat Transfer and Performance Characteristics

TABLE OF CONTENTS

Report K-910900-10

Analytical Studies of Nuclear Light Bulb Engine

Radiant Heat Transfer and Performance Characteristics

SUMMARY

The analytical studies of nuclear light bulb engine characteristics were divided into two major sections: (1) a continuing analysis of engine operating and transient response characteristics, with an emphasis on engine shutdown and (2) a detailed study of the radiation heat transfer characteristics of the fuel and buffer-gas regions. Emphasis in the radiation heat transfer calculations was placed on calculations of the spectral distribution of radiated energy emitted from the nuclear fuel region over a wide range of engine power levels and calculations of the effectiveness of seed systems in altering the spectral distribution of radiant energy.

It was determined that engine shutdown may be accomplished by stopping the fuel injection to the cavity region. Total power drops to 10 percent of the steady-state value in approximately 0.2 sec and decreases to zero in 6 sec. The propellant flow rate may be reduced to 10 percent of its steady-state value in 36 sec, but must be maintained at that value for approximately 160 sec in order to avoid overtemperatures in the beryllium oxide regions. Residual heat remaining after approximately 200 sec may be rejected by means of a space radiator.

The investigations of the dynamic response of the controlled engine to various perturbations indicated that a control response proportional to the difference between the instantaneous value of the neutron flux level and the desired steady-state value resulted in smaller variations in power than the control response proportional to the rate-of-change of neutron flux previously investigated. The studies also indicated that changes in the heat loads due to radiation and conduction in the moderator and structure will necessitate revisions to the order in which principal engine components are cooled. These modifications, plus the inclusion of a space radiator circuit, should be incorporated in the dynamic simulation program so that any variations in the responses to various perturbations during steady-state operation may be determined.

Spectral distributions of radiant energy emitted from the nuclear fuel region and incident on the transparent wall structure were calculated using a neutron transport theory code. The spectral heat fluxes and corresponding radial temperature distributions were used to calculate the heat loads in the buffer gas and

transparent walls due to absorption of radiant energy. These calculations were limited to the special case in which the temperature at the edge of the fuel with buffer seed is set approximately equal to the calculated edge-of-fuel temperature without buffer seed, the nuclear fuel partial pressure distribution within the nominal edge-of-fuel region is fixed, and convection takes place in the buffer-gas region bounded by the transparent wall and the nominal edge-of-fuel region. The fraction of ultraviolet energy incident on the transparent walls increases with increasing power level. For the reference engine power level of 4600 megw, it is necessary to either increase propellant flow rate or employ space radiators to reject the ultraviolet radiated energy absorbed by the transparent walls. This ultraviolet energy can be blocked by employing nitric oxide and oxygen seed gases in the fuel and buffer-gas regions. However, this results in increased ultraviolet absorption in the buffer gas which also requires either an increase in propellant flow rate or space radiators to reject the heat load. An increase in propellant flow rate reduces specific impulse and increases engine thrust-to-weight ratio, whereas the addition of space radiators allows specific impulse to remain constant and the engine thrust-to-weight ratio to decrease. It is concluded that investigations of seeding systems for the fuel and buffer-gas regions should be continued to identify seeds which will block ultraviolet radiation emitted from the fuel region more effectively than the nitric oxide and oxygen seed gases, and thereby minimize both the convection heat load in the buffer gas and the radiation absorption by the transparent walls.

RESULTS AND CONCLUSIONS

1. The performance of the nuclear light bulb engine, based on an extrapolation of previously reported reference engine operating conditions, is estimated to extend over a range of specific impulse from 1100 to 3200 sec with corresponding thrust-to-weight ratios from 0.4 to 6.9. Extension to the higher specific impulses requires further research on alternate transparent wall materials, techniques for the transpiration cooling of the exhaust nozzles and minimization of the thermal radiation absorption in the buffer gas and transparent walls.

2. A control which causes a variation in the fuel control valve flow area proportional to the difference between the desired steady-state neutron flux level and the instantaneous value of neutron flux results in much smaller variations in relative power during perturbations than the rate-of-change of neutron flux control previously investigated.

3. Engine shutdown may be accomplished by stopping the fuel injection to the cavity region. Total power drops to 10 percent of the steady-state value in approximately 0.2 sec and decreases to zero in 6 sec. The propellant flow rate may be reduced to 10 percent of its steady-state value in 36 sec, but must be maintained at that value for approximately 160 sec in order to avoid overtemperatures in the beryllium oxide regions. Residual heat remaining after 200 sec may be rejected by means of a space radiator.

4. The use of space radiators is necessary to avoid the expenditure of large amounts of hydrogen propellant for cooldown after each engine run. The total afterheat which must be removed is on the order of 10^8 kw-sec for a 1000-sec engine run and would require the expenditure of 12,000 kg of hydrogen for cooldown after each run. A lightweight aluminum radiator weighing approximately 4000 kg would be sufficient to remove the afterheat.

5. Dose rates from residual radioactivity in the engine after shutdown are dependent upon the location of the fission products within the engine after shutdown which is dependent on the efficiency of the separators and the amount and location of fuel plating, if any, which occurs during operation and shutdown. If all the fission products are separated out and removed from the engine system or shielded, dose rates at 1 ft from a point source equivalent to the induced radioactivity in the engine components would be less than 1 rad/hr 5000 sec after a 1000-sec run at 4600 megw.

6. Calculations of spectral heat flux emitted from the fuel region were made for multiples from 1 to 100 times the reference engine heat flux with neon as the buffer gas and with no seed in the buffer gas. The fractions of spectral heat

flux in the uv wavelength range below the uv absorption cutoff for beryllium oxide transparent walls at 0.125 microns were 0.054, 0.081, and 0.340 for 1, 10, and 100 times the reference engine heat fluxes, respectively (values of specific impulse of 1870, 2580, and 3600 sec, respectively). The fractions of spectral heat flux in the uv wavelength range below the uv absorption cutoff for fused silica walls at 0.18 microns were 0.135, 0.190, and 0.680 for 1, 10, and 100 times the reference engine heat fluxes, respectively.

7. Calculations of the energy below the uv cutoff for both beryllium oxide and fused silica transparent walls for engine power levels in the range from 1 to 100 times that of the reference engine indicate that, without seeds, the heat loads due to uv energy absorption are such that neither the fused silica nor beryllium oxide walls can be cooled sufficiently without modification of the engine design or operating conditions. The increase in energy deposited in the transparent structure would require an increase in propellant weight flow or the addition of a space radiator.

8. Calculations of spectral heat fluxes in the edge-of-fuel and buffer-gas regions were made for the reference engine with partial pressures of nitric oxide/oxygen seed in the fuel and buffer-gas regions ranging from 0.01 to 200.0 atm. These calculations were limited to the special case in which the temperature at the edge of the fuel with buffer seed is set approximately equal to the calculated edge-of-fuel temperature without buffer seed, the nuclear fuel partial pressure distribution within the nominal edge-of-fuel region is fixed, and convection takes place in the buffer-gas region bounded by the transparent wall and the nominal edge-of-fuel region. Buffer-gas weight flows and temperature distributions were calculated for the buffer-gas region such that the energy absorbed in the seeded buffer gas was convected away. The seeding of 0.01 atm of nitric oxide/oxygen results in an approximately linear temperature distribution in the buffer region. Higher seed pressures result in steepening temperature gradients in the buffer region near the edge of fuel, and a leveling off to approximately 2000 R (the assumed wall temperature) through the outer portion of the buffer region. For seed partial pressures in excess of 0.10 atm, the buffer-gas flow required to convect radiant energy absorbed by the seeded buffer gas resulted in an axial pressure drop in excess of a limiting value of approximately 1 atm based on structural considerations. The effects of varying the nuclear fuel partial pressure distribution or the thickness of the convection region on these results have not been investigated.

9. Based on the current calculations, the nitric oxide/oxygen seed system does not block the uv energy emitted from the fuel region adequately. Studies should be continued to identify seeds or seed systems with strong uv absorption coefficients in the wavelength range below 0.18 microns for fused silica and in the wavelength range below 0.125 microns for beryllium oxide. In order to block the uv radiation before reaching the buffer gas, the strong absorption coefficients must persist at temperatures above 7000 K.

INTRODUCTION

Investigations of various phases of gaseous nuclear rocket technology are being conducted at the United Aircraft Research Laboratories under Contract SNPC-70 administered by the joint AEC-NASA Space Nuclear Systems Office. Previous investigations were conducted under NASA Contracts NASw-847, NASW-768, and NAS3-3382; under Air Force Contracts AF 04(611)-7448 and AF 04(611)-8189; and under Corporate-sponsorship.

The principal research effort is presently directed toward the closed-cycle, vortex-stabilized nuclear light bulb engine. As discussed subsequently, this engine concept is based on the transfer of energy by thermal radiation from gaseous fissioning uranium, through a transparent wall, to hydrogen propellant. The basic design of this engine is described in Ref. 1. Subsequent investigations performed to supplement and investigate the basic design and to investigate other phases of nuclear light bulb engine component development are reported in Refs. 2 through 7. References 8 through 11 describe the results of related nuclear light bulb research conducted through September 1971.

Prior to 1969, studies of the design and operating characteristics of the nuclear light bulb engine were concerned primarily with characteristics of the engine operating at full-power, steady-state conditions. During 1969, a digital computer simulation model of the engine was formulated to investigate the transient response of the engine to perturbations about full-power steady-state design conditions. The engine dynamics model is described in Ref. 2. During 1970, the studies of the transient operating characteristics of the engine were extended to investigate the transient operating conditions during reactor start-up. Also, the engine dynamic simulation program was modified to include changes in the reference design and to investigate the effects of various types of control systems on the dynamic response of the engine. Results of the engine characteristics studies performed during 1970 are described in Ref. 4.

During the present year, studies of radiant heat transfer characteristics in the reference engine were combined with studies of engine design and dynamic operating characteristics. Previous calculations (see Refs. 12 and 13) performed at United Aircraft Research Laboratories have indicated that the spectral distribution of radiated energy emitted from the nuclear fuel region differs appreciably from that of a black-body at an effective radiating temperature of 15,000 R. These studies reveal that with no seed approximately 17 percent of the total radiated flux is emitted at wave numbers greater than about 55,000 cm^{-1} where the fused silica transparent containment wall becomes essentially opaque. Thus, it is necessary to find an effective seed to add to the fuel and buffer-gas regions to prevent ultraviolet radiation from impinging upon the transparent containment walls. During the 1970

contract period, investigations of the effectiveness of nitric oxide/oxygen (NO/O_2) seed systems were investigated. The results of these investigations are reported in Ref. 12. The addition of seeds to the fuel and buffer-gas region, in addition to blocking the ultraviolet radiation from reaching the transparent wall, also tends to cause radiant energy absorption in the buffer-gas region. It is therefore necessary to determine the amount of radiant energy which is absorbed by the buffer gas due to the presence of a seed system because this energy must be convected into the fuel recirculation system.

The objectives of the work described herein were (1) to continue analysis of the engine operating characteristics and responses to various perturbations, with an emphasis on operating characteristics during engine shutdown, and (2) a detailed study of the radiant heat transfer characteristics in the fuel and buffer-gas regions of the engine, with emphasis on the effectiveness of seeds added to the fuel and buffer-gas regions in blocking uv radiation from reaching the transparent walls and simultaneously minimizing radiant energy absorption in the buffer gas. The radiant heat transfer studies with seeds in the fuel and buffer-gas regions were limited to the special case in which the temperature at the edge of the fuel with buffer seed is set approximately equal to the calculated edge-of-fuel temperature without buffer seed, the nuclear fuel partial pressure distribution within the nominal edge-of-fuel region is fixed, and convection takes place in the buffer-gas region bounded by the transparent wall and the nominal edge-of-fuel region. The program and the results of the analytical calculations are described in the succeeding sections of this report.

DESCRIPTION OF ENGINE CHARACTERISTICS

Discussion of Engine Performance

Calculations were made to determine the approximate operating conditions and performance levels of nuclear light bulb engines over a wide range of fuel radiating temperatures. The objectives of the study were to determine the variations in the performance level and to provide information on engine operating conditions which would aid in the identification of design limitations and specific areas in which further research would be required to extend the performance.

The engine operating characteristics and performance were based on modifications of the reference nuclear light bulb engine described in Ref. 1. Important design characteristics of this engine are given in Table I. The principal assumptions used in the calculations discussed below are (1) the propellant exit temperature, T_p, is equal to 0.8 times the fuel radiating temperature, T^*, (2) the power deposited in the moderator and structure is equal to 15 percent of the total engine power, (3) moderator and structure weight is constant regardless of radiating temperature, and (4) engine operating pressure is equal to 2.5 times the required uranium partial pressure in the fuel region. The engine power level is directly proportional to the fourth power of the fuel radiating temperature, T^*. Using assumption (4) above and the data in Ref. 14, the relation between the engine operating pressure and the total power radiated is $P_C = 52.2\ Q^{0.268}$. The variation in total engine weight was then calculated on the basis of a constant moderator and structure weight (assumption (3) above) and the variation of required pressure vessel weight with operating pressure. The total enthalpy of the propellant exiting the reactor was taken from Ref. 15. Propellant flow rates were calculated by dividing the engine power level by the propellant enthalpy associated with the assumed propellant exit temperature.

The calculation procedure described always results in a maximum value of the specific impulse for the selected fuel radiating temperature. The calculated value of the propellant flow rate may not be sufficient to remove the power deposited in the moderator and structure (15 percent of the total as noted in assumption (2)) without exceeding the maximum allowable temperatures in the moderator materials. For these cases a space radiator could be used to reject the excess heat. [3]

The calculated specific impulse and thrust-to-weight ratio for a range of fuel radiating temperatures is shown in Fig. 1. The variations in total power, operating pressure, propellant flow rate, total engine weight, and thrust with fuel radiating temperature are shown in Fig. 2.

Effects of Variations in Radiating Temperatures

As the fuel radiating temperature increases both the specific impulse and thrust-to-weight ratio increase as seen on Fig. 1. All quantities shown in Fig. 2 also increase with increasing radiating temperature. When it becomes necessary to use space radiators, the total engine weight begins to increase much more rapidly as seen in Fig. 2. The rate of increase is dependent upon the assumed radiator weight per unit of power rejected. The fuel radiating temperature above which radiators would be used is dependent upon both the maximum allowable moderator temperature and the radiator material. The more rapid increase in total engine weight when radiators are added causes the peak in thrust-to-weight ratio shown in Fig. 1.

Design Limitations

It is not possible to vary the fuel radiating temperature over the entire range investigated without considering modifications to the basic engine design. The principal limitations on performance and the fuel radiating temperature ranges associated with the limitations were considered in order to define the areas in which additional research is required if higher engine performance levels are to be achieved. The limits considered include (1) maximum radiation absorption in the buffer region, (2) maximum heat loads to the transparent wall, (3) space radiator requirements and their effect on total engine weight, and (4) transpiration cooling limitations in the exhaust nozzle.

Radiation Absorption in the Buffer Region

As the fuel radiating temperature is increased, the edge-of-fuel temperature also increases. When the temperature at the edge of the fuel region becomes high enough to induce significant opacity in the buffer gas, primarily due to the onset of ionization, a significant fraction of the emitted thermal radiation will be absorbed and convected away with the buffer-gas flow.

Based on the calculated spectral absorption coefficients for neon in Ref. 5 and the calculated imbalances in the buffer-gas region at high temperatures, this limit is estimated to occur at edge-of-fuel temperatures of 12,200 to 13,900 K (22,000 to 25,000 R) corresponding to equivalent black-body radiating temperatures of 15,900 to 18,000 K (28,600 to 32,400 R).

Transparent Structure

The limitations on performance imposed by the transparent structure are related to both the spectral heat flux incident on the transparent wall and the wavelength below which all uv energy is assumed to be absorbed in the walls, or the uv cutoff.

The uv cutoff for fused silica is about 0.18 microns, and the calculated fraction of energy emitted below this wavelength from the reference engine without seeds is 13.5 percent of the total radiant energy. Two possible methods of reducing the energy deposition in the transparent structure are (1) seeding of the buffer gas with a material which will absorb the uv energy before it reaches the wall or (2) using an alternate material in the transparent wall with a uv cutoff at a shorter wavelength than 0.18 microns. A material which has been considered for use as a transparent wall, other than fused silica, is single-crystal beryllium oxide (BeO). The uv cutoff for single-crystal BeO is about 0.12 microns. The calculated fraction of energy emitted below this wavelength from the reference engine without seeds is 5.3 percent of the total radiant energy. Thus, it appears that the use of a seed material is required to limit the radiant energy absorbed by the transparent walls. Details of the radiation spectrum from unseeded uranium plasma and uranium seeded with a mixture of NO and O_2 are discussed in the section titled RADIANT HEAT TRANSFER.

Radiator Requirements

The requirement for use of space radiators during steady-state operation is determined by the total amount of power deposited in the moderator and structure and the maximum allowable moderator temperature. The performance characteristics and operating conditions (Figs. 1 and 2) were calculated for two values of the maximum moderator temperature and two values of radiator weight per unit of power rejected.

The assumption, previously mentioned, that 15 percent of the total power in the engine is deposited in the moderator was based on the detailed calculation of the engine heat balance as discussed in Ref. 4. In these calculations it was assumed that the uv energy from the fuel region was blocked by the addition of a seed material to the buffer gas so that the total energy deposited in the buffer gas and transparent wall was equal to 3 percent of the total engine power.

If, due to the limitations on radiation from the cavity or absorption in the transparent structure, the total energy deposited in the buffer gas and transparent wall is greater than about 3 percent of the total power, space radiators must be employed at lower fuel radiating temperatures than shown in Figs. 1 and 2. The effect of the space radiator heat rejection would, in general, be a slight reduction in specific impulse due to the loss of energy which is available for deposition in the propellant by radiation and an increase in total engine weight due to the increased size of the radiator.

Nozzle Cooling

The high temperatures present in the exhaust nozzle require that the nozzle be transpiration cooled with hydrogen. In the reference engine, the transpiration

cooling flow is approximately 12 percent of the primary hydrogen propellant flow and causes a 6 percent reduction in the specific impulse. As the propellant temperature increases, a higher transpiration coolant flow is required which causes a more significant decrease in specific impulse. It is shown in Ref. 16, that the limiting value of specific impulse would be between 2500 and 5000 sec or at fuel radiating temperatures above 11,000 K (19,800 R).

Engine Dynamics and Control

Studies of the dynamic responses of the controlled engine were continued using the engine dynamic simulation program described in Refs. 2 and 4. A flow diagram of the three coolant circuits and their interrelation is shown in Fig. 3. A block diagram of the control system proposed for use during start-up and steady-state operation is shown in Fig. 4. Recent studies were concerned primarily with various types of controls to determine the type of control, response times and control gain that would give a satisfactory response to all of the perturbations to the steady-state conditions.

The heat loads to the various components of the engine were recalculated based on revised estimates of fission product heat deposition and radiation and convection heating in various structural components. Details of the results of these calculations are discussed in a subsequent subsection titled "Engine Heat Loads". The results of these studies indicated that the maximum allowable temperatures in some of the engine components will be exceeded if the cooling sequence shown in Fig. 3 is used. A revision of the cooling circuitry, possibly to include a space radiator system, is necessary and will necessitate a revision of the dynamic simulation program. Extensive studies of various types of engine controls were, therefore, deferred pending revision of the simulation program.

Investigations of Control Responses

The dynamic response of the uncontrolled engine and the response with a control of the fuel injection valve based on the rate-of-change of neutron flux are described in Ref. 4. The dynamic response studies discussed herein are concerned with the response of the engine using a control of the fuel injection valve based on the difference between the instantaneous value of neutron flux and the desired steady-state value of neutron flux. The perturbations investigated were the same as those reported in Ref. 4 with the exception of the turbopump wheel speed variation. The dynamic simulation program was modified to permit the investigation of step changes in turbine control valve area and turbine nozzle area instead of the previously imposed wheel speed ramp. It was determined from studies of the response to step changes in these two areas that it was not possible to generate a ramp in the turbopump wheel speed of the magnitude previously used as an input, due to the inertia

of the turbopump. Substitution of the turbine control valve and turbine nozzle perturbations for the turbine wheel speed ramp results in a more realistic perturbation and also introduces the possibility of using the turbine control valve as a secondary control mechanism for damping pressure fluctuations.

Rate-of-Change of Neutron Flux Level

The response of the engine to perturbations using a control based on the rate-of-change of neutron flux was discussed in Ref. 4. The principal disadvantage of this type of control is the undamped oscillation caused by the control. Since it is necessary to assume some minimum value of the rate-of-change of neutron flux to which the control will not respond, the control usually results in a finite ramp in power. It becomes necessary to impose a secondary control based on the absolute value of neutron flux to terminate the ramp. This combination of controls results in a controlled response of the engine which is a triangular wave oscillation with frequency depending on the allowable rate-of-change of neutron flux and the amplitude depending on the absolute limit of neutron flux allowed by the secondary control.

Absolute Value of Neutron Flux Level

A sensor is included in the control circuit to measure the instantaneous value of neutron flux (see Fig. 4). The response of the engine to a change in fuel control valve area which is directly proportional to the difference in the instantaneous and steady-state values of the neutron flux was investigated. The equation relating the control valve area change to the neutron flux level is

$$\delta A = (A_F)_o C_V (N_o - N) \qquad (1)$$

where δA is the variation in the fuel control valve area after each time increment, $(A_F)_o$ is the steady-state value of the fuel control valve area, C_V is a proportionality constant, N_o is the steady-state value of neutron flux, and N is the instantaneous value of the neutron flux after each time increment. The fuel control valve area, A_F, may be expressed as

$$A_F = (A_F)_o + \delta A_{F_1} + \delta A_{F_2} \qquad (2)$$

where δA_{F_1} is the imposed perturbation in the fuel control valve area, when applicable, and δA_{F_2} is the cumulative change in the fuel control valve area due to control respons

Then, δA_{F_2} is equal to the summation of the δA values calculated from Eq. (1). Initial calculations were made using various values of the proportionality constant, C_V, and the dead band width (values of N_o-N for which no control response occurs). From these results a proportionality constant of 0.002 and a dead band width of ±0.5 percent was selected and used for the data described herein. A 50-msec time delay was assumed between the time of the neutron flux measurement and the time the valve area correction was initiated.

The responses of the controlled engine, using the absolute value of neutron flux, to step changes in imposed reactivity, fuel control valve area and exhaust nozzle area are shown in Figs. 5, 6 and 7, respectively. With the exception of the negative step change in exhaust nozzle area, the controlled responses are low-frequency, damped oscillations. In the case of the negative step change in exhaust nozzle area, a higher-frequency oscillation occurs as shown in Fig. 7(b). This oscillation is initiated by the control system since a response of this type does not occur in the uncontrolled case. Investigations of the use of secondary control mechanisms to eliminate this higher-frequency oscillation were deferred pending modifications to the dynamic simulation program.

Engine Heat Loads

The component heat loads in the reference engine were recalculated based on revised estimates of fission product heat deposition and the radiation and convection to the end walls and liner tubes. A comparison of the revised values (referred to as Modification I) and the reference engine values are shown in Table II. The revised values (Modification I) are based on the following assumptions: (1) any increase in fission product power during operation due to the build-up of fission products before an equilibrium concentration is reached must be offset by a decrease in fission power so that the total engine power will remain constant; (2) the convective heat load to the transparent structure and cavity liner may be reduced by a factor of three by introducing relatively cool, unseeded buffer layers adjacent to the walls; (3) the cavity end walls and cavity liner are aluminum with a reflectivity of 0.9 and the radiation to the cavity liner may be reduced by a factor of two by controlling the distribution of the seed material in the propellant duct. Variations in the heat deposited in the buffer gas and transparent structure, as discussed in the section of this report titled RADIATION HEAT TRANSFER, are not included in the revised heat loads shown in Table II. It may be noted from Table II that the increase in the total heating in the components is less than 10 percent. The increase is concentrated in components which must be maintained at a temperature below 835 K (1500 R) and there is not a sufficient quantity of coolant flow (low-temperature heat sink) to accomplish the cooling required at this temperature level.

Three possible methods of revising the coolant circuits were investigated (1) increasing the propellant flow rate to provide additional heat sink capacity, (2) adding space radiators to reject a portion of the heat, and (3) substituting a tungsten-coated graphite cavity liner for the aluminum liner currently used.

The propellant flow rate required to reduce the component temperatures to the desired level is approximately 26.6 kg/sec. An increase to this flow rate would cause a reduction in specific impulse of the reference engine from 1870 sec to the order of 1600 sec.

The addition of space radiators, or the utilization of the space radiators required for afterheat removal, would provide sufficient cooling capability with no decrease in specific impulse. The radiator weight required would be dependent upon the amount of heat to be rejected and the rejection temperature levels.

If the cavity liners are made from tungsten-coated graphite rather than aluminum, the radiation heat load is increased due to the lower reflectivity of tungsten (0.6 as compared to 0.9 for aluminum, see Ref. 1). The tungsten-graphite liner may be operated at a considerably higher temperature, allowing this component to be cooled after the solid moderator regions.

Selection of the preferred method of revising the engine design was not made at this time due to the uncertainties in the buffer gas and transparent wall heat loads as discussed in the section of this report titled RADIANT HEAT TRANSFER. After a determination of all of the changes which may be caused by variations in the radiation heat loads, it will be necessary to reconsider the possible revisions in engine design and then select a new configuration to be incorporated in the engine dynamics program.

Engine Shutdown

The calculation of engine operating characteristics during shutdown is dependent upon both the variation in power due to fission in the fuel region and the quantity of afterheat (heat from the decay of radioactive fission products and induced radioactivity in structural components) which must be removed. Immediately after the power due to fission in the fuel region has been reduced to zero by removing the uranium fuel, the afterheat generated is approximately 2.5 percent of the full-power operating level. This afterheat, and the sensible heat which must be removed from the moderator, is the primary factor in determining the operating conditions and cooling requirements during shutdown. Therefore, the engine shutdown schedule is based on a power ramp which is determined by the fuel containment characteristics of the vortex and the decay of fission products and radioisotopes generated during operation rather than an imposed power ramp similar to that used in the start-up studies.

Possible Shutdown Schedule

The sequence of events required for a shutdown which is initiated by terminating the fuel injection to the cavity region is shown in Table III. The controls required during shutdown are similar to those used during start-up and steady-state operation as shown in Fig. 4. The fuel flow is terminated by closing the fuel injection valve, V_1, the desired flow rate in the primary hydrogen circuit and radiator circuit is controlled through valves V_5 and V_7, and the exhaust nozzle, V_6, is closed after the flow of primary propellant is stopped. Since the neutron flux level is reduced to a very low level after the first 5 to 10 seconds, the sensors of the neutron flux level and rate of change, S_1 and S_2 would not be used during the shutdown to provide any feedback to the control valves. Pressure and temperature levels and coolant flow rates are monitored by sensors S_3 through S_7 (see Fig. 4) and any required flow rate changes are made by varying the flow area of the appropriate control valve.

Heat Sources After Shutdown

After the power due to fission in the fuel region has been reduced to zero, there is approximately 100 to 150 megw of power generated in the engine due to the decay of fission products and radioisotopes formed by neutron irradiation of the structural materials. In addition to these power sources, it is also necessary to remove a portion of the sensible heat in the moderator to avoid overheating internal structural components adjacent to the moderator regions. The coolant flow requirements during the majority of the shutdown ramp (for $t_s > 5$ sec) are determined by the fission product afterheat power level.

Fission Product Afterheat

The power released due to the decay of radioactive fission products is a function of the engine run time and the time elapsed since shutdown. The calculated fission product power is shown in Fig. 8 for various engine run times. The instantaneous value of fission product power is between 100 and 150 megw and the time required for the power to decay to 10 kw is between 1 and 15 days. The total heat released by the fission products (equal to the integral of the power with respect to time) is between 1.5×10^7 and 1.5×10^8 kw-sec as shown in Fig. 9.

The required shutdown schedule is dependent not only on the magnitude of the fission product power but also on the location of the fission products within the engine after shutdown and the location within the engine where the decay energy is deposited. All of the fission products are contained in some part of the fuel and neon circuit after shutdown, but since they decay by emitting gamma-rays or high-energy particles, the decay energy may be deposited in other regions of the engine. For the calculations described above, it was assumed that the breakdown of fission

product decay energy was 20 percent in the fuel and neon circuit, 20 percent in structural components cooled by the secondary circuit, 40 percent in the solid moderator, and that the remaining 20 percent passed through the pressure vessel without depositing any heat in the engine.

Induced Radioactivity Heating

During engine operation, certain materials in the engine become radioactive due to neutron absorption. The primary sources of induced radioactivity, as described in Ref. 6, are oxygen-18, aluminum-27, tungsten-184, and nickel-15. The total power level immediately after shutdown is approximately 5.5 megw and decays to the order of 10 kw in approximately 20 min as shown on Fig. 8. The total heat release from induced radioactivity is approximately 7×10^5 kw-sec as shown in Fig. 9. Since the majority of the materials which become activated are in the moderator or internal structure, it was assumed that the induced radioactivity power would be deposited in the solid moderator.

Sensible Heat

The steady-state operating temperatures of the solid moderator materials are 1500 K (2700 R) in the beryllium oxide and 2110 K (3800 R) in the graphite. The low-temperature materials (primarily beryllium or aluminum) in the structural components adjacent to the moderator (flow divider, tie rods and liner tubes) must be maintained at a temperature of not more than 833 K (1500 R). It is therefore necessary to continue cooling these structural components after shutdown until the moderator temperatures are reduced to 833 K. The total quantity of sensible heat which must be removed is on the order of 1.64×10^7 kw-sec (1.55×10^7 Btu). If this heat is removed by internally cooling the structural components so that the maximum temperatures do not exceed 833 K (1500 R), the rate of heat removal immediately after shutdown is 4.05 megw.

Removal of Heat After Shutdown

Two methods of removing the heat generated after shutdown were investigated, (1) direct cooling of the engine by continuing the flow of primary hydrogen propellant and (2) rejection of the heat through an auxiliary space radiator system. A summary of the total weight of hydrogen which must be expended during shutdown and the required weight of an auxiliary space radiator is shown in Table IV. If direct hydrogen cooling is used, the weight required is based on the total quantity of heat to be removed as shown in Fig. 9. A similar amount of hydrogen would be required at the end of each engine run if multiple engine runs are required. The weight of the space radiator required is dependent upon the heat rejection rate or power level immediately after shutdown and the radiator inlet and outlet temperatures. The variations of radiator weight and pressure drop with radiator temperature

level for a radiator capable of rejecting 115 megw are shown in Figs. 10 and 11, respectively. Since it is necessary to maintain the beryllium structural components at a temperature of 833 K (1500 R) or below, an aluminum radiator with an inlet temperature of 833 K (1500 R) and an outlet temperature of 389 K (700 R) was selected. Since the radiator is reusable, the weight required does not vary with the number of engine runs.

Calculations of engine operating characteristics during shutdown, as discussed in the following sections, indicated that a combination of direct hydrogen cooling and space radiators is required.

Operating Conditions During Shutdown

The minimum shutdown time possible is achieved by terminating the fuel injection to the cavities and allowing the power to decrease proportional to the amount of fuel remaining in the fuel region. The initial power ramp was determined using the dynamic simulation program described in Ref. 4. The variation in the relative power level is shown in Fig. 12. The power drops to 1 percent of the full-power value in approximately 0.8 sec. During this time the contained mass of fuel decreased from the steady-state value of 13.65 kg (30 lb) to 11.5 kg (25.3 lb). It was assumed that the power variation from 1 percent to zero would be linear, reaching zero power at t_s = 6 sec.

The temperature in the fuel region was calculated using the same heat balance equations used in the calculation of the temperature levels during start-up (see Ref. 4). The variation in average fuel temperature is shown in Fig. 13. It can be seen that although the power has been reduced to zero in 6 sec, the heat capacity of the gases and fuel in the vortex extends the time of the temperature ramp to the order of 40 sec.

The coolant flow rate variations were based on the time required for the average fuel temperature to reach 333 K (600 R). It was assumed that the flow rates in the neon circuit and the secondary circuit would remain at their steady-state values during the shutdown ramp and that the primary propellant flow would be reduced as the radiator flow was increased as shown in Fig. 14. Two coolant flow schedules were investigated as shown in Fig. 14, one with a linear decrease in propellant flow rate to zero in 40 sec and one with an extended cooling period at 10 percent of the design flow rate. The total hydrogen expended during shutdown is 385 kg (846 lb) for the 40 sec ramp and approximately 618 kg (1360 lb) for the 200 sec ramp.

The calculated power deposition in the fuel and neon circuit and the secondary circuit are shown in Figs. 15 and 16, respectively. It may be noted that shortly after shutdown (5 to 10 sec) the majority of the power deposited in these circuits is due to fission product decay and induced radioactivity heating.

The calculated temperature variations in the beryllium oxide moderator region are shown in Fig. 17 for the two coolant flow schedules. If the propellant flow is reduced to zero in 40 sec, the heating due to fission products and induced radioactivity is higher than that which can be removed through the secondary cooling circuit and the temperature rises to a value of about 1700 K (3060 R) which is above the level allowable in the beryllium oxide (1500 K (2700 R)). If the propellant flow is continued at 1.97 kg/sec (4.32 lb/sec) from 36 sec after shutdown to 190 sec and then reduced to zero between 190 and 200 sec, the maximum temperature in the beryllium oxide does not exceed 1500 K (2700 R).

The temperature levels in the graphite moderator during shutdown are shown in Fig. 18. Maximum allowable temperatures in the graphite are not exceeded with either flow schedule so that the temperature levels in the beryllium oxide moderator are the determining factor with regard to the desired flow schedule. The large mass of moderator material in the engine tends to keep the internal temperatures at a relatively constant level during the shutdown.

The engine operating pressure during shutdown shown in Fig. 19 was calculated on the basis of the assumed propellant flow schedule (shown in Fig. 14), the calculated propellant exit temperature, and a constant exhaust nozzle area equal to the steady-state operating value. During the early phases of shutdown (0 to 2 sec), when the fuel is still in vapor form, the pressure levels shown in Fig. 19 are sufficiently high to insure containment of the fuel ($\rho_{B6} > \bar{\rho}_{F6}$). More detailed information regarding fuel density during the later phases of shutdown are necessary before the required containment parameters can be specified.

Design Modifications to Improve Accessibility and Reusability

Calculations of the estimated radiation dose rates in various components of the engine were made to determine the effect of the activity levels on engine accessibility and reusability. The factors which influence the dose rate in a specific component are related to engine run time, cool-down time (time after shutdown required to remove afterheat) and the location of radioactive fission products after shutdown. The principal assumptions employed in the calculation are:

1. After engine operation, a cool-down time of between 5×10^5 sec (5.8 days) and 2×10^6 sec (23.2 days) is necessary in order to remove fission product decay heat before disassembly can begin.

2. The heat and radiation dosage from induced activity in the moderator and structure is negligible at times greater than 5×10^5 sec ($Q < 10^{-7}$ kw, $DR < 10^{-1}$ r/hr at 1 ft after 5×10^3 sec).

3. The approximate distribution of fission products after engine operation (based on data from Ref. 17) is: 58.7 percent will condense with the fuel, 20 percent will condense in the H_2-Ne heat exchanger (if no multiple stage condenser-separator units are employed) and 21.3 percent will be in gaseous form and not condense but be carried with the neon.

4. The energy deposition and dose rates are directly proportional to the quantity of fission products in a location so that the heat and radiation doses in various regions will follow the same distribution as assumed in 3 above.

5. The rate of burn-up of uranium and production of fission products is 0.063 gm/sec of operating time.

6. Variations in the physical properties of fission products with time are not considered.

Three specific cases were investigated based on the assumption of (1) perfect fuel separation, (2) 80 percent efficient fuel separation, and (3) a 5-Å-thick deposition of fuel and fission products on the cavity end walls and transparent structure. In the first case, all of the fission products which condense with the fuel are assumed to be in the fuel storage container. In case (2) fuel and fission products which are not separated are assumed to condense in the heat exchanger. In both cases (1) and (2) no plating of fuel or fission products occurs in the cavity region so that there is no activation of the end walls or transparent structure.

The radiation dose rate from each component was calculated from a relation between the decay energy and the dose rate. For an unshielded point source in air the dose rate, DR, is

$$DR = 6 \times 10^3 \frac{C E_P}{f^2} \tag{3}$$

where C is the specific activity in curies, E_P is the energy of the decay photon in Mev, and f is the distance from the source in ft. Since the specific activity and decay photon energy for each radioisotope present is not accurately known, these terms were related to the total energy release from all of the fission products. The specific activity, C, can be expressed as:

$$C = \frac{1.13 \times 10^{13} M_I}{(AA)\, t_{1/2}} e^{\frac{-0.693\, t}{t_{1/2}}} \tag{4}$$

where M_i is the mass of the radioisotope present in grams, AA is the atomic weight in grams, $t_{1/2}$ is the radioactive half-life in sec, and t is the total elapsed time after the production of the isotope. The total energy released by the radioisotope, Q_T, is

$$Q_T = \frac{6.688 \times 10^7 M_I E_P}{(AA)\, t_{1/2}} e^{\frac{-0.693\, t}{t_{1/2}}} \qquad (5)$$

Substituting Eq. (5) and Eq. (4) into Eq. (3) yields

$$DR = 10^6 \frac{Q_T}{f^2} \qquad (6)$$

where DR is in roentgens (r) per hour, Q_T in kw and f in ft. The radiation dose rates calculated for the three cases are shown in Table V.

In Case I of Table V, the dose rates in the neon gas heat exchanger and fuel storage container are extremely high, and access to other parts of the engine would require removal and storage of these components. It would be possible to reduce the activity level in the heat exchanger by using a hot purge gas to vaporize and remove the low-boiling-point fission products if desired. The fuel and neon could be stored and replaced in the engine when accessibility was no longer required.

In Case II of Table V, the only effect of imperfect fuel separation is the deposition of high-boiling-point fission products in the heat exchanger which increases the activity level and a corresponding decrease in the activity level in the fuel storage container. In this case a hot purge gas will not remove all of the activity in the heat exchanger so that this component will have to be removed if access to the internal regions of the engine is desired.

In Case III of Table V, the activity level of the transparent structure and end walls with a 5-Å coating of fuel and fission products is shown. The activity levels in the other components will be the same as in Case I or II depending upon the assumptions about fuel separation efficiency. The activity levels in the transparent structure and end walls are much lower so that short-time inspection of these components would be possible. They could be removed for cleaning or replacement after an additional 15 to 30 day cool-down.

The results of these studies indicate that if a design modification to improve accessibility is desired, some provision for simplifying the removal of the fuel

storage container, hydrogen-neon heat exchanger and the neon gas contained in the fuel and neon circuit is required. It should be noted that the dependence of the results of this study on the location of fission products after shutdown would indicate that further investigations of the types of fission products formed and their distribution after shutdown should be conducted.

RADIANT HEAT TRANSFER

Analytical Model

The analytical model used in fuel and buffer region radiant heat transfer calculations is shown in Fig. 20. In the nuclear light bulb concept a fissioning gaseous uranium plasma is contained in the fuel region within a vortex of neon buffer gas. The nuclear fuel emits thermal radiation which must pass through the surrounding neon buffer region. The region of analysis is defined to include the outer section of a cylindrical fuel-containment region along with the neon buffer region which extends to the inside edge of the transparent wall as shown in Figs. 20(a) and 20(b). The partial pressure distributions of the nuclear fuel, neon buffer gas, and NO/O_2 seed gas are shown in Fig. 21. The distributions shown are for an engine (seeded with 10 atm of NO/O_2 seed gas) with a total engine power of 4600 megw. The total pressure is 500 atm in the engine fuel cavity. The fuel partial pressure distribution is assumed to be constant at 200 atm from the cavity centerline out to one half the fuel cloud radius and then to decrease linearly to zero at the edge-of-fuel location. The neon and NO/O_2 seed (if present) then account for the difference between the total pressure and the fuel partial pressure.

Source Description

The mechanism of radiation transport in the fuel region of the nuclear light bulb engine is by the absorption and re-emission of thermal energy. The radiation transport problem can be solved by neutron transport theory computer programs (Refs. 18 and 19). Since scattering is negligible, these are "source-sink" problems with the specification of the source being the vital requirement. The emission of energy is characterized by the black-body spectrum at the local temperature. The black-body spectral energy intensity is given by

$$I(\lambda T) = \frac{2\pi c^2 h}{\lambda^5} \quad \frac{1}{e^{ch/\lambda kT} - 1} \tag{7}$$

where c is the speed of light, h is Planck's constant, k is Boltzmann's constant, λ is the wavelength, and T is the temperature. Dividing by T^5 and integrating over λT, we have for constant temperature, T,

$$\int \frac{I(\lambda T)}{T^5} d(\lambda T) = \frac{1}{T^4} \int I(\lambda T) d\lambda \tag{8}$$

By definition, the total energy intensity is

$$e_{TOT} = \int I(\lambda T)\, d\lambda = \sigma T^4 \tag{9}$$

where σ is the Stefan-Boltzmann constant. Hence

$$\int \frac{I(\lambda T)}{T^5}\, d(\lambda T) = \sigma \tag{10}$$

The total energy density (Ref. 20) is defined to be

$$\epsilon_{TOT} = \frac{4 e_{TOT}}{c} = \frac{4T^4}{c} \int \frac{I(\lambda T)}{T^5}\, d(\lambda T) \tag{11}$$

The wavelength spectrum is divided into any desired number of wavelength bands or groups with which the "multi-group" method of solution is applied over the entire wavelength range. Since the neutron transport theory equations are cast in a conservation-of-particle-form, it is desirable to convert the energy-density source into a photon-density source. The photon source strength in the interval from λT to $\lambda T + \delta(\lambda T)$ can be represented by dividing the corresponding energy source strength by the average energy of a photon of wavelength $\bar{\lambda}$. Using $\bar{E} = hc/\bar{\lambda}$, the photon source is given by

$$\chi\left[\lambda T \rightarrow \lambda T + \delta(\lambda T)\right] = \frac{4T^4}{c} \int_{\lambda T}^{\lambda T + \delta(\lambda T)} \frac{I(\lambda T)}{T^5}\, d(\lambda T) \Big/ \frac{hc}{\bar{\lambda}} \tag{12}$$

where

$$\bar{\lambda} = \left[\lambda T + (\lambda T + \delta(\lambda T))\right] \Big/ 2T \tag{13}$$

In Eq. (12), $\chi(\lambda T \rightarrow \lambda \dot{T} + \delta(\lambda T))$ is expressed in units of photons per unit volume, a time independent function. A source which is a time-rate function is required. Each photon moves with velocity c cm/sec, and λ_{mfp} is the mean free path for the absorption process in the medium, that is, the average distance a photon will travel from the time it is re-emitted until it is absorbed. Then, on the average, c/λ_{mfp} is the photon interaction probability per sec. If the photon density, i.e., the number of photons per cubic centimeter of the beam is $\chi(\lambda T \rightarrow \lambda T + \delta(\lambda T))$, then the number of photons absorbed is $\chi(\lambda T \rightarrow \lambda T + \delta(\lambda T))\ (c/\lambda_{mfp})$ per cm^3 per sec. Since $\lambda_{mfp} = 1/a_\omega$, where a_ω is the spectral absorption coefficient, this can be written as $a_\omega c\ \chi(\lambda T \rightarrow \lambda T + \delta(\lambda T))$. When a system is in thermodynamic equilibrium, the absorption rate is equal to the source strength. Hence, the photon source strength as a time-rate function is given by

$$\chi'\left[\lambda T \rightarrow \lambda T + \delta(\lambda T)\right] = 4a_\omega T^4 \int_{\lambda T}^{\lambda T + \delta(\lambda T)} \frac{I(\lambda T)}{T^5}\, d(\lambda T) \Big/ \frac{hc}{\bar{\lambda}} \qquad (14)$$

$\chi'\ (\lambda T \rightarrow \lambda T + \delta(\lambda T))$ is the photon source strength in the form to be used in the neutron transport theory computer program (Ref. 18) and is in units of photons per unit volume per unit time.

Fuel Region Temperature Iteration Technique

A discussion of the flux equations used in the two computer programs, ANISN (Ref. 18) and TAXSI, which iterates on a temperature distribution, is given in APPENDIX A. Also included in APPENDIX A is a method of weighting absorption coefficients. The radiation transport problem solved in one-dimensional cylindrical geometry for the nuclear light bulb engine requires that the product of the radiation heat flux and the cylindrical surface area remain constant throughout the portion of the fuel region in the region of analysis. This is consistent with the assumption of no fission sources in the region of analysis. A spectral heat flux boundary condition is specified at the inner cylindrical surface of the region of analysis, along with an initial temperature distribution. Since the total energy across any cylindrical surface must be constant, a balance between energy sources (reradiated) and the energy absorbed is required in each different temperature interval. The initial temperature distribution must be perturbed until the energy absorbed and reradiated becomes equal. This can be accomplished by singularly modifying the temperature in one interval in which the following perturbation is applied.

$$\text{Energy Source - Energy Absorbed} = 0$$

$$\left(S_\ell - \frac{dS}{dT}\,\Delta T\right) - \left(\left(\Sigma_a \phi V\right)_\ell - \frac{d(\Sigma_a \phi V)}{dT}\,\Delta T\right) = 0 \tag{15}$$

If $\Delta T = T_\ell - T_{\ell+1}$, then rewriting and combining terms we have

$$T_{\ell+1} = T_\ell + \frac{S_\ell - \left(\Sigma_a \phi V\right)_\ell}{\left[\dfrac{d(\Sigma_a \phi V)}{dT} - \dfrac{dS}{dT}\right]} \tag{16}$$

In the above equation, the terms apply for the i^{th} interval and T_ℓ, S_ℓ, and $(\Sigma_a \phi V)_\ell$ are the temperature, energy source, and energy absorbed in the ℓ^{th} iteration; $T_{\ell+1}$ is the new interval temperature for the $\ell+1$ iteration; dS/dT and $d(\Sigma_a \phi V)/dT$ are the derivatives of the energy source and energy absorption with respect to temperature. The convergence procedure starts at the innermost interval and proceeds outward toward the edge-of-fuel requiring convergence to a degree ϵ in each interval before proceeding out to the next interval. When the outermost fuel interval and all inner intervals satisfy convergence within a level ϵ, then ϵ is reduced to $\epsilon/2$ and the iteration returns to the innermost fuel interval and the iteration procedure is resumed. After convergence of a temperature distribution has been achieved in TAXSI, the sources and opacities of the converged temperature distribution are used in ANISN to compute in more detail, and with more accuracy, the flux distributions. If the resulting agreement between ANISN and TAXSI flux distributions is not satisfactory, the updated transport properties from ANISN are introduced into TAXSI and the iteration of the temperature distribution is resumed. This sequence continues until the convergence is satisfactory in both ANISN and TAXSI.

Convection Region Temperature Iteration Technique

A discussion of the equations used in the convection analysis is given in APPENDIX A. As in the fuel region, the buffer-gas region was divided into small radial intervals. The assumed buffer-gas flow pattern is shown in Fig. 22. The buffer gas enters the region by tangential injection at the transparent wall. The flow moves radially inward and gradually turns until it is moving axially such that at the stagnation surface there is no net radial buffer weight flow. The flow is assumed to travel in stream tubes as indicated in Fig. 22. In the solution of the one-dimensional problem, each interval represents a stream tube in the application of a finite-difference method of calculation where the temperature, velocity, and density of the gas are assumed constant over the interval. Initially, a piecewise linear temperature distribution is assumed in the buffer-gas region as shown in

Fig. 23. Properties are evaluated at the midpoint of each interval and the flux calculation is performed. The sum of the convected energy and the energy re-emitted must equal the energy absorbed in each interval for a converged temperature distribution. In practice each interval is required to satisfy convergence of the energy balance to a degree ϵ. When convergence is not satisfied in the buffer region, a new temperature distribution in the buffer gas is calculated such that a linear temperature gradient across each interval will correct the energy imbalance between the energy absorbed and the energy reradiated for the current temperature in each region. Perturbations of the temperature in each interval are made when the convergence parameter, ϵ, is not satisfied. Convergence on a temperature distribution results when the imbalance between energy absorbed and energy reradiated and convected becomes essentially zero. The sequence of events which typically results as the temperature distribution converges in each buffer region interval is illustrated in Fig. 23 (progressing from iteration 1 to iteration 2 and finally iteration 3 which would represent the final temperature distribution converged to degree, ϵ). A further constraint is the requirement that the temperature at the edge of the transparent wall must be approximately 1100 K. This constraint imposes another level in the buffer region temperature convergence, since a different converged temperature distribution exists for each axial pressure drop assumed in the buffer region.

Establishment of the Spectral Heat Flux Boundary Condition

The radiant heat transfer calculation for the nuclear light bulb engine need only be performed for the narrow outer layer of the fuel region. This occurs because the absorption coefficients for the mixture of buffer gas and nuclear fuel near the edge-of-fuel region are sufficiently high to cause the optical depth, τ_ω, to be generally greater than 1.0 over the wavelength range of interest in an annular region approximately 1-cm thick at the edge of the fuel cloud. Furthermore, it is assumed that the uranium mass density near the edge-of-fuel location is low, therefore, fission energy deposition near the edge-of-fuel location is negligible compared to the radiant energy passing through the region. On this basis, the presence of a fission source is neglected in the region of analysis. Since the calculation does not encompass the entire fuel region, but rather a narrow section near the edge-of-fuel location, a boundary condition must be specified at the inner boundary of the region of analysis. The present method employed is to impose a black-body spectral energy heat flux calculated at the temperature of the inner boundary and normalized to the desired edge-of-fuel total heat flux. This satisfies the constraint of constant total energy at any cylindrical surface in the outer layer of the fuel region when a converged temperature distribution is obtained.

Discussion of Results

Temperature Distribution in Fuel Region

Fuel region temperature distributions for radiant heat fluxes of 1, 5, 10, and 100 times the reference engine heat flux (q_o = 2.73 x 10^{11} erg/cm^2-sec) are shown in Fig. 24 for the outer layer of the fuel region. Unseeded neon buffer gas was present in the buffer region, and there was assumed to be no back radiation from the propellant stream or from wall reflections. The total engine pressures of 500, 750, 880, and 1850 atm correspond to the 1, 5, 10, and 100 q_o power levels, respectively, and are taken from Ref. 14 assuming a constant average fuel density in the fuel region. The edge-of-fuel temperatures for these cases are 6400, 9540, 11,850, and 20,400 K, respectively, and the effective black-body radiating temperatures for these power levels are 8330, 12,460, 14,820, and 26,350 K, respectively. The corresponding values of T_e/T^* are 0.77, 0.77, 0.80, and 0.77 for the specified power levels; T_e/T^* would be equal to 0.84 if the gas opacities at a given temperature were independent of wavelength.

Calculated Flux Distribution

The spectral heat flux distribution at the edge-of-fuel location for total heat fluxes from 1 to 100 times the reference engine heat flux are shown in Fig. 25 as a function of wave number. The wave number band of interest (10^6 to 10^3 cm^{-1}) was divided into 80 wave number groups, the widths of which varied as indicated on the spectral plots. The peaks in the spectra at approximately 75,000 and 120,000 cm^{-1} are persistent at 1, 5, and 10 q_o with the tendency for the spectra to fill in the valleys in the wave number range between 20,000 to 70,000 cm^{-1} with increasing heat flux for these cases. At 100 q_o, the spectral valleys are essentially filled. The corresponding fractional heat flux variations as a function of wave number are given in Fig. 26. The half energy fraction shifts from a wave number of 20,000 cm^{-1} for the 1 q_o (reference engine) calculation, to 28,000 cm^{-1}, 32,000 cm^{-1} and 68,000 cm^{-1} for the 5, 10, and 100 q_o calculations, respectively. In view of the significant fractions of uv energy reaching the transparent walls, a NO/O_2 seed gas with high uv absorption coefficients was introduced into the fuel and buffer gas to reduce the uv radiation content.

The thickness at the outer fuel region which influences the spectral radiation flux at the edge-of-fuel location is determined by the optical depth variation with wave number. The optical depth at a given wave number, ω, is given by

$$\tau_\omega = \int_0^{\Delta R} a_\omega \, dR \qquad (17)$$

where ΔR is the distance measured from the edge-of-fuel, R is the radius, and a_ω is the spectral absorption coefficient as a function of ω and R. Figure 27 contains plots of optical depth, τ_ω for the reference engine calculation in the wave number intervals as indicated. Optical depths are also shown in Fig. 28 for the 10 q_o calculation over the same wavelength bands. These optical depth plots correspond to fuel and neon mixtures in the fuel region with temperature distributions as shown in Fig. 24.

The effective spectral black-body radiating temperature distribution, T_ω^{bb}, for 1, 5, and 10 times the reference engine heat flux is shown in Fig. 29. T_ω^{bb} is defined as that temperature for which the spectral heat flux at the edge-of-fuel location, q_ω, is equal to a black-body spectral heat flux, q_ω^{bb}. The effective black-body radiating temperatures, T^*, for the 1, 5, and 10 times q_o calculations are 8330, 12,460, and 14,820 K, respectively. These results clearly show that the fuel region is not radiating as a black body at the same temperature over all wavelengths. However, the effective black-body radiating temperature, T^*, for each multiple of reference engine heat flux is shown to pass through each of the spectral black-body radiating temperature distributions.

Ultraviolet Cutoffs of Transparent Walls and Buffer Gas Cooling Capability

Two of the more promising candidate materials for use as transparent wall structures for the nuclear light bulb engine are fused silica and single-crystal beryllium oxide. Fused silica becomes opaque to uv radiation at wave numbers greater than 55,500 cm^{-1} (wavelengths less than 0.18 microns) while beryllium oxide becomes opaque to uv radiation at wave numbers greater than 80,000 cm^{-1} (wavelengths less than 0.125 microns). In this study it is assumed that radiant energy at wave numbers greater than the uv cutoffs of the transparent wall materials under consideration is absorbed totally by the transparent structure.

Studies of the characteristics of the reference engine described previously have shown that the transparent wall structure should be maintained at temperatures less than approximately 1100 K (2000 R). In addition, it has been shown that the mixture of fuel and buffer gas ejected from each unit cell of the engine into a fuel recirculation system should be cooled to a temperature of approximately 1100 K to insure condensation of gaseous fuel prior to separation and recirculation. These constraints require that energy absorbed by the buffer gas and the transparent wall structures be rejected to a working fluid at temperatures less than 1100 K. The low temperature heat sink for rejected energy is the primary propellant. The propellant leaves a storage tank at approximately 100 K, passes through heat exchangers to absorb energy deposited in the fuel recirculation system and various structural components, including the transparent walls. Within these constraints, it was determined that for the reference engine power level of 4600 megw, the primary propellant would be capable of absorbing a combined heat load to the

transparent walls and buffer gas of approximately 3 percent of the total reference engine power. Heat loads to these two components above the 3 percent level must be rejected by either increasing primary propellant weight flow or by employing space radiators. Increasing primary propellant weight flow will result in an increase in engine thrust-to-weight ratio and a decrease in specific impulse. The addition of space radiators causes a decrease in engine thrust-to-weight ratio while maintaining the specific impulse constant. These space radiators have been estimated to weigh 1500 kg for each percent of reference engine power rejected. Another limiting factor in the cooling of transparent-wall structures is the ability to conduct heat through the internally-cooled walls, a property related directly to the material thermal conductivity and the maximum allowable temperature gradient through the wall. Any additional constraint on the ability to remove heat from the buffer gas region is based on a limiting axial pressure drop resulting from the buffer-gas flow rate required to convect away absorbed energy. This axial pressure drop was chosen to be 1.0 atm on the basis of assumed structural properties of the transparent wall.

The fractions of energy below the uv cutoffs for both BeO and SiO_2 transparent walls for engine power levels in the range from 1 to 100 times that of the reference engine are shown in Fig. 30. The opacity of neon buffer gas without NO/O_2 seed is very low in the wave number range of interest in the buffer-gas region and, therefore, the fraction of energy absorbed in the buffer gas is a relatively small convection load. Also shown on Fig. 30 are the temperature drops across the two transparent-wall materials required to conduct the absorbed uv energy into the coolant stream. Due to the relatively low thermal conductivity of SiO_2, wall temperature differences in excess of 600 K (1080 R) across a wall 0.0127-cm (0.005-in.) thick are required to remove the uv energy absorbed at all engine power levels. BeO however, has a thermal conductivity ten times that of SiO_2 and absorbed uv energy can be removed for power levels up to 13.5 times the reference engine power level with a temperature difference of 600 K (1080 R) across a wall 0.0127-cm (0.005-in.) thick. In all cases, some of the uv energy absorbed by the transparent walls would have to be rejected either by increasing primary propellant weight flow such that the propellant exit temperature was less than 0.8 times the equivalent black-body radiating temperature ($T_E < 0.8\ T^*$) or by employing space radiators and maintaining $T_E = 0.8\ T^*$.

Temperature Distribution in Seeded Buffer Gas

In order to reduce the uv heat load on the transparent wall, an NO/O_2 seed mixture was introduced into the buffer-gas and fuel regions. The temperature distributions in the buffer-gas region which result from adding 0.01, 0.10, and 1.0 atm of NO/O_2 seed are shown in Fig. 31. These calculations were limited to the special case in which the temperature at the edge of the fuel with buffer seed is set approximately equal to the calculated edge-of-fuel temperature without buffer seed, the nuclear fuel partial pressure distribution within the nominal

edge-of-fuel region is fixed, and convection takes place in the buffer-gas region bounded by the transparent wall and the nominal edge-of-fuel region. The temperature distributions vary from approximately 6400 K at the edge of fuel to approximately 1100 K at the transparent wall. The temperature of 1100 K at the transparent wall was a constraint required for each different NO/O_2 seed partial pressure. Except for small variations in the edge-of-fuel temperature, T_E, the temperature distribution in the fuel region for all NO/O_2 seed pressures is essentially the same as that of the reference engine, 1 q_o, shown in Fig. 24. The effects of varying the nuclear fuel partial pressure distribution or the thickness of the convection region on these results were not investigated.

Spectral Flux With NO/O2 Seed

The reference engine spectral flux at the edge-of-fuel location for NO/O_2 seed pressures of 0.01, 0.10, and 1.0 atm are indicated in Fig. 32. The corresponding fractional heat flux variations as a function of wave number are shown in Fig. 33. The effect of the seed is to reduce the fraction of energy radiated at wave numbers greater than approximately 100,000 cm^{-1} for seed pressures of 0.10 and 1.0 atm. The spectrum at the edge-of-fuel location with 0.01 atm of seed is nearly identical to that for no seed. The peak at 120,000 cm^{-1} wave numbers has been greatly reduced as the seed pressure is varied from no seed to 1.0 atm. However, the spectral peak at approximately 75,000 cm^{-1} wave numbers is not significantly altered by the seed system. The optical depths, τ_ω, for NO/O_2 seed partial pressures of 0.0, 0.01, 0.10, and 1.0 atm are given in Fig. 34 for the wave number interval 120,500 to 119,500 cm^{-1}. Figures 35 and 36 show the optical depth at seed pressures of 0.0 and 1.0 atm for the wave number intervals 75,000 to 72,500 cm^{-1} and 32,500 to 30,000 cm^{-1}, respectively. The small effect on the opacity at wave numbers less than 100,000 cm^{-1} (wavelengths greater than 0.10 microns) with the addition of NO/O_2 seed pressures ranging from 0.0 to 1.0 atm is indicated by results shown in Figs. 35 and 36. This accounts for the spectral flux results shown in Fig. 32.

The effective spectral black-body radiating temperature distribution, T_ω^{bb}, for the reference engine heat flux with 0.01, 0.10, and 1.0 atm of NO/O_2 seed added to the fuel and buffer regions is shown on Fig. 37. The distributions begin to significantly diverge at a wave number of approximately 100,000 cm^{-1}. The effect of adding seed results in a lower effective radiating temperature in the wave number range above approximately 100,000 cm^{-1}.

Attenuation of UV Energy by NO/O2 Seeds in Buffer Region

The fractional attenuation of the reference engine energy in the uv portion of the spectrum with NO/O_2 seed partial pressures of 0.01, 0.10, and 1.0 atm as a function of radius in the seeded buffer-gas region is indicated in Fig. 38. The fractions shown are relative to the total heat flux at the edge-of-fuel location. The variation of energy above the single-crystal BeO and fused silica uv cutoffs

of 0.125 and 0.18 microns, respectively, are shown for the NO/O_2 seed pressures mentioned. The results indicate that the uv energy emitted from the fuel region can be effectively blocked before this energy can reach and be absorbed by either BeO or SiO_2 transparent walls. For example, the uv energy reaching either transparent wall is effectively reduced to zero with the addition of 1.0 atm of NO/O_2 seed. For SiO_2 transparent walls (wavelengths less than 0.18 microns), the uv energy emitted from the fuel region is shown to be reduced from 0.135 to 0.1205 to 0.1135 for the seed pressures of 0.01, 0.10, and 1.0 atm, respectively. Correspondingly, for the BeO transparent walls (wavelength less than 0.125 microns), the fraction of uv energy is reduced from 0.0531 to 0.0375 to 0.031 for the same NO/O_2 seed partial pressures. A summary of the uv energy fractions at the edge-of-fuel location for SiO_2 and BeO transparent-wall wavelength cutoffs are tabulated at various engine power levels and various NO/O_2 seed partial pressures for the reference engine in Table VI. As the seed pressure was varied in the reference engine, the temperature distribution in the fuel region was held constant out to 0.10 cm from the edge-of-fuel location. The temperature in this region was allowed to change so that imbalances in energy source and energy absorption could adjust. This resulted in small changes in the temperature, the greatest of which was approximately 50 K.

Convection Parameters in Seeded Buffer Region

Figures 39, 40, and 41 show the variation of buffer-gas weight flow, convected energy, and axial velocity with radius in the buffer region for NO/O_2 seed partial pressures of 0.01, 0.10, and 1.0 atm, respectively. These distributions correspond to the buffer-gas-region temperature distributions shown in Fig. 31. For seed pressures of 0.01, 0.10, and 1.0 atm, respectively, total neon buffer weight flows per cell of 25.6, 272, and 1510 kg/sec were calculated; total power convected per cell of 40.8, 69.6, and 75.5 megw were calculated; and axial velocities at the edge-of-fuel location were 16.8, 116, and 632 m/sec, respectively. Figure 42 shows the variation of buffer weight flow per cm of cell length with the buffer-gas temperature at the edge of the transparent wall for NO/O_2 seed partial pressures of 0.01, 0.10, and 1.0 atm. In all cases, a small change in the buffer flow rate results in a larger change in the buffer-gas temperature at the edge of the transparent wall. For a 10 percent change in total buffer weight flow, approximately 67, 27, and 21 percent changes in buffer-gas temperature at the transparent wall occur for seed pressures of 0.01, 0.10, and 1.0 atm, respectively.

As has been previously stated, for the reference engine a limiting axial pressure drop of 1.0 atm in the buffer region was assumed based on assumed structural limits on the transparent wall. Figure 43 shows the variation of axial dynamic pressure in the buffer-gas region as the NO/O_2 seed partial pressure is increased over the range from 0.01 to 200.0 atm. As the seed pressure is increased, energy is absorbed at locations nearer the edge-of-fuel boundary. When this occurs, steep temperature gradients occur in the inner layer of the buffer gas located near the edge-of-fuel location. Figure 31 shows the steepening of the temperature gradient in the buffer region as NO/O_2 seed pressure is increased, and the tendency of the convected energy in the buffer region to be preferentially convected in the layer near the edge-of-fuel

location as seed pressure is increased from 0.01 to 1.0 atm is shown in Figs. 39, 40, and 41. As more NO/O_2 seed is added, less uv energy is emitted from the fuel region as indicated in Table VI, and therefore, there is less uv energy which can be absorbed in the seeded buffer region. However, there is a tendency for the seeded buffer gas to absorb more energy from the visible portion of the spectrum as more seed is added. These two competing effects result in the expectation of a local minimum occurring in the buffer gas convected energy prior to the onset of massive absorption in the visible portion of the spectrum. This results in the decrease in the axial pressure drop (see Fig. 43) in changing the seed pressure from 10.0 to 200.0 atm. The detailed shape of the axial pressure drop between seed pressures of 1.0 and 200.0 atm is not completely determined, but it is reasonably certain that an axial pressure drop less than 1.0 atm does not exist between NO/O_2 seed pressures of 1.0 and 200.0 atm. The reason for the steepness of the temperature gradient in the buffer region near the edge-of-fuel location is given in Fig. 44, where the convected energy density or the volumetric convected energy rate is shown as a function of NO/O_2 seed pressure in that region. The greater the amount of radiant energy which is absorbed in a given volume of buffer gas, which in turn must be partially removed by convection, the greater is the temperature drop across that volume. Since a constant axial dynamic pressure is assumed, extremely high axial velocities result near the edge-of-fuel location along with high buffer weight flows.

Buffer Convection and Transparent-Wall Heat Loads

The effect on the convective and transparent wall heat loads are shown in Fig. 45 for NO/O_2 seed pressures ranging from 0.0 to 1.0 atm. For a SiO_2 transparent wall, the combined convection and transparent wall heat loads expressed as a fraction of the total radiated power (upper plot in Fig. 45) decrease from 0.135 to 0.115 as seed partial pressure is varied from 0.0 to 1.0 atm. However, for a BeO transparent wall heat load increases from 0.053 to 0.115 over the range of seed partial pressures. This is because NO/O_2 seeds absorb uv radiation below the uv cutoff for BeO causing absorption of energy by the seeded buffer gas which is not necessary for protection of the wall. Thus, the NO/O_2 is a very poor seed mixture when BeO is used for the transparent wall. A qualitative desired behavior of an unspecified seed gas with combined convection and transparent wall heat loads is shown in the upper plot of Fig. 45 as dashed curves for both BeO and SiO_2 transparent walls. The variation with the absolute magnitude of seed partial pressure is uncertain; however, the desire to reduce the combined fraction of both heat loads to less than 0.01 at the relatively low seed pressures as depicted is to be sought. In the lower plot of Fig. 45, the fraction of the transparent wall heat load relative to the combined convection and transparent wall heat loads is indicated for both the SiO_2 and BeO wall structures. It can be seen from Fig. 45 that the transparent wall can be protected from the uv portion of the energy by addition of NO/O_2 seeds to the fuel and buffer-gas regions. In particular, the

addition of 1 atm of seed essentially reduces the transparent wall heat load to zero. However, the convection heat load in the buffer-gas region becomes approximately equal to the fraction of uv energy which is emitted above wave numbers greater than 55,500 cm^{-1} (wavelengths less than 0.18 microns) from the edge-of-fuel location. The NO/O_2 seed system does limit the fraction of uv energy deposited in the transparent wall but does not effectively minimize the energy convected from the buffer-gas region. It is important to use seeds which shift the spectrum away from the uv in the edge-of-fuel region, thereby blocking the uv from the buffer gas. Studies must be continued to identify seeds with strong uv absorption coefficients in the wave number range above 55,500 cm^{-1} (wavelengths less than 0.18 microns) for SiO_2 and in the wave number range above 80,000 cm^{-1} (wavelengths less than 0.125 microns) for BeO. To block the uv radiation before reaching the buffer gas, the strong absorption coefficients must persist at temperatures above 7000 K.

If NO/O_2 was the only seed system available, the use of 0.1 atm of NO/O_2 seed and space radiators would have the effect of reducing engine thrust-to-weight ratio by about 30 percent, relative to the reference engine or would require an increase in primary propellant flow such that specific impulse would be reduced to 1500 sec and thrust-to-weight ratio would be increased to 103 percent of that of the reference engine.

Again, the effects of varying the nuclear fuel partial pressure distribution or the thickness of the convection region on these results were not investigated.

REFERENCES

1. McLafferty, G. H. and H. E. Bauer: Studies of Specific Nuclear Light Bulb and Open-Cycle Vortex-Stabilized Gaseous Nuclear Rocket Engines. United Aircraft Research Laboratories Report F-910093-37, prepared under Contract NASw-847, September 1967. Also issued as NASA CR-1030.

2. Latham, T. S., H. E. Bauer, and R. J. Rodgers: Studies of Nuclear Light Bulb Start-Up Conditions and Engine Dynamics. United Aircraft Research Laboratories Report H-910375-4, prepared under Contract NASw-847, September 1969.

3. McLafferty, G. H.: Investigation of Gaseous Nuclear Rocket Technology - Summary Technical Report. United Aircraft Research Laboratories Report H-910093-46, prepared under Contract NASw-847, November 1969.

4. Bauer, H. E., R. J. Rodgers, and T. S. Latham: Analytical Studies of Start-Up and Dynamic Response Characteristics of the Nuclear Light Bulb Engine. United Aircraft Research Laboratories Report J-910900-5, prepared under Contract SNPC-70, September 1970.

5. Krascella, N. L.: Spectral Absorption Coefficients of Helium and Neon Buffer Gases and Nitric Oxide-Oxygen Seed Gas Mixture. United Aircraft Research Laboratories Report K-910904-2, prepared under Contract SNPC-70, September 1971.

6. Latham, T. S.: Nuclear Studies of the Nuclear Light Bulb Rocket Engine. United Aircraft Research Laboratories Report G-910375-3, prepared under Contract NASw-847, September 1968. Also issued as NASA CR-1315.

7. McLafferty, G. H.: Gas Core Nuclear Rocket Engine Technology Status. Journal of Spacecraft and Rockets, Vol. 7, No. 12, December 1970, p. 1391.

8. Roman, W. C. and J. F. Jaminet: Experimental Investigations to Simulate the Thermal Environment and Fuel Region in Nuclear Light Bulb Reactors Using an R-F Radiant Energy Source. United Aircraft Research Laboratories Report K-910900-7, prepared under Contract SNPC-70, September 1971.

9. Klein, J. F.: Experiments to Simulate Heating of Propellant by Thermal Radiation in a Nuclear Light Bulb Engine. United Aircraft Research Laboratories Report K-910900-8, prepared under Contract SNPC-70, September 1971.

10. Bauer, H. E.: Initial Experiments to Investigate the Condensation of Flowing Heated-Gas/Metal-Vapor Mixtures in a Circular Duct. United Aircraft Research Laboratories Report K-910900-9, prepared under Contract SNPC-70, September 1971.

REFERENCES (Continued)

11. Palma, G. E. and R. Gagosz: Effect of 1.5 Mev Electron Irradiation on the Transmission of Optical Materials. United Aircraft Research Laboratories Report K-990929-2, prepared under Contract SNPC-70, September 1971.

12. Krascella, N. L.: Analytical Study of the Spectral Radiant Flux Emitted from the Fuel Region of a Nuclear Light Bulb Engine. United Aircraft Research Laboratories Report J-910904-1, prepared under Contract SNPC-70, September 1970.

13. Krascella, N. L.: Theoretical Investigation of the Radiant Emission Spectrum from the Fuel Region of a Nuclear Light Bulb Engine. United Aircraft Research Laboratories Report H-910092-12, prepared under Contract NASw-847, September 1969.

14. Kesten, A. S. and N. L. Krascella: Theoretical Investigation of Radiant Heat Transfer in the Fuel Region of a Gaseous Nuclear Rocket Engine. United Aircraft Research Laboratories Report E-910092-9, prepared under Contract NASw-847, September 1966. Also issued as NASA CR-695.

15. Roback, R.: Theoretical Performance of Rocket Engines Using Gaseous Hydrogen in the Ideal State at Stagnation Temperatures Up to 200,000 R. United Aircraft Research Laboratories Report E-910093-30, prepared under Contract NASw-847, October 1966. Also issued as NASA CR-696.

16. McLafferty, G. H.: Limitations on Gaseous Nuclear Rocket I_{sp} Due to Nozzle Coolant Requirements. Journal of Spacecraft and Rockets, Vol. 3, No. 10, October 1966, pp. 1515-1522.

17. McLafferty, G. H.: Coolant Recycle System for Nuclear Light Bulb Reactor. United Aircraft Research Laboratories Report E-110224-5, June 9, 1966.

18. Engle, W. W., Jr.: A User's Manual for ANISN, A One-Dimensional Discrete Ordinates Transport Code with Anisotropic Scattering. Union Carbide Corporation Report K-1693, 1967.

19. Mynatt, F. R., F. J. Muckenthaler, and P. N. Stevens: Development of Two-Dimensional Discrete Ordinates Transport Theory for Radiation Shielding. Union Carbide Corporation Report CTC-INF-952, 1969.

20. Chandrasekhar, S.: Radiative Transfer. Dover Publications, Inc., New York, New York, 1960.

21. Carlson, B. G. and G. I. Bell: Solution of the Transport Equation by the S_n Method. Proceedings of the Second United Nations International Conference on the Peaceful Uses of Atomic Energy. International Atomic Energy Agency, Geneva, 1958, p. 2386.

LIST OF SYMBOLS

A	Element of area, cm^2
A^*	Exhaust nozzle area, cm^2
A_F	Fuel injection control valve area, cm^2
AA	Atomic weight, gm
$\bar{a}\ (\lambda_1 \rightarrow \lambda_2, T)$	Averaged absorption coefficient between wavelengths λ_1 and λ_2 at temperature T, cm^{-1}
a_ω	Spectral absorption coefficient, cm^{-1}
$\bar{a}_\omega$	Averaged absorption coefficient, cm^{-1}
C	Specific activity of radioisotope, curies
C_P	Specific heat, ergs/gm - deg K
C_V	Control proportionality constant
c	Speed of light, 3×10^{10} cm/sec
DR	Dose Rate, mR/hr
dA	Differential area element, cm^2
$d\Omega$	Differential element of solid angle, steradian
E	Total heat release, kw-sec
$\bar{E}$	Average photon energy, ergs/photon
E_{FP}	Total heat release from fission products, kw-sec
E_{IR}	Total heat release from induced reactivity, kw-sec
E_P	Energy of decay photon, Mev
e_{TOT}	Total black-body energy intensity, $ergs/cm^2$-sec

LIST OF SYMBOLS (Continued)

F	Engine thrust, lb
F/MT	Engine thrust-to-weight ratio
f	Distance from radioactive source, ft
g	Gravitational acceleration constant, 981 cm/sec^2
h	Planch's constant, 6.625 x 10^{-27} ergs-sec
I (λT)	Black-body spectral energy intensity, ergs/cm^2-sec-cm
I_{SP}	Specific impulse, sec
k	Boltzmann's constant, 1.38 x 10^{-16} ergs/deg K
L_1	Photon leakage out of an interval, photons/sec
L_2	Photon leakage into an interval, photons/sec
M_I	Mass of radioisotope, gm
M_T	Total engine weight, lb
N	Instantaneous value of neutron flux, neutrons/cm^2-sec
NN	Photon angular flux, photons/cm^2-sec-unit solid angle
n	Order of Sn calculation
P	Pressure, atm
P_F	Fuel partial pressure, atm
P_I	Fuel injection pressure, atm
P_N	Neon partial pressure, atm
P_S	Seed partial pressure, atm
P_T	Total engine pressure, atm
Q	Engine power, megw

LIST OF SYMBOLS (Continued)

Q_C	Energy convected by buffer gas, ergs/sec
Q_{FP}	Fission product power, kw
Q_{IR}	Power from induced reactivity, kw
Q_R	Total radiant energy at edge-of-fuel location, ergs/sec
Q_T	Total energy released by radioactive isotope decay, kw
Q_{TW}	Energy absorbed at transparent wall below λ_{CUTOFF}, ergs/sec
$Q_{\lambda<\lambda_{CUTOFF}}$	Energy below wavelength, λ_{CUTOFF}, ergs/sec
q_T	Heat flux at edge-of-fuel location, ergs/cm^2-sec
q_ω	Spectral heat flux at edge-of-fuel location, ergs/cm-sec
q_ω^{bb}	Black-body spectral heat flux, ergs/cm-sec
R	Radius, cm
R_1	Inner radial boundary of region of analysis, cm
R_2	Inner radial boundary of transparent wall, cm
R_6	Radius of fuel region, cm
S	Photon source strength, photons/cm^3-sec
T	Temperature, deg K or deg R
T^*	Effective black-body fuel radiating temperature, deg K or deg R
T_{BeO}	Temperature in beryllium oxide moderator, deg K or deg R
T_E	Temperature at edge-of-fuel location, deg K or deg R
T_F	Average fuel region temperature, deg K or deg R
T_G	Temperature in graphite moderator, deg K or deg R

LIST OF SYMBOLS (Continued)

T_M	Maximum moderator temperature, deg K or deg R
T_P	Propellant exit temperature, deg K or deg R
$(T_R)_{IN}$	Radiator inlet temperature, deg K or deg R
$(T_R)_{OUT}$	Radiator outlet temperature, deg K or deg R
T_{TW}	Buffer-gas temperature at transparent wall, deg K or deg R
T_ω^{bb}	Effective spectral black-body radiating temperature, deg K or deg R
t	Time, sec
t_R	Engine run time, sec
t_S	Time after shutdown, sec
$t_{1/2}$	Radioactive half-life, sec
V	Element of volume, cm^3
V_Z	Axial velocity in buffer region, cm/sec
W_{BR}	Radial buffer weight flow, kg/sec
W_{BZ}	Axial buffer weight flow, kg/sec
W_H	Propellant flow rate, kg/sec
W_{H_S}	Secondary hydrogen coolant flow rate, kg/sec
$(W_T)_{RAD}$	Total radiator weight, gm
W_d	Weight associated with Sn discrete directions
X	Distance, cm
α	Angular redistribution coefficient, cm^2-unit solid angle
β	Reciprocal of photon flux-weighted polar angle cosine

LIST OF SYMBOLS (Continued)

$\Delta Q/Q_o$	Power level change
$\Delta Q_C/\Delta V$	Convected energy density, ergs/cm^3-sec
ΔP_R	Pressure loss in radiator, atm
ΔP_Z	Axial pressure drop in buffer region, atm
ΔR	Distance from edge-of-fuel location, cm
ΔT	Temperature drop across a buffer interval, deg K or deg R
ΔT_{TW}	Transparent wall temperature difference, deg K or deg R
δA	Variation in fuel injection control valve area during time increment, cm^2
δA_{F_1}	Imposed change in fuel injection control valve area, cm^2
δA_{F_2}	Change in fuel injection control valve area caused by control system, cm^2
δk	Total reactivity change
δk_o	Reactivity required to compensate for loss of delayed neutrons
δk_1	Imposed reactivity change
δk_2	Feedback reactivity change
ϵ	Convergence parameter
ϵ_{TOT}	Total black-body energy density, ergs/cm^3
λ	Wavelength of photon, microns
$\bar{\lambda}$	Average photon wavelength, cm
λ_{CUTOFF}	Wavelength below which transparent wall material is considered highly absorbing, microns

LIST OF SYMBOLS (Continued)

λ_{mfp}	Average photon mean free path, cm
μ	Polar angle cosine with respect to X-axis or R-axis
μ_d	Discrete polar angle cosine with respect to X-axis or R-axis
ρ	Density, gm/cm^3
ρ_{B6}	Buffer-gas density at injection, gm/cm^3
$\bar{\rho}_{F6}$	Average fuel density at edge-of-fuel location, gm/cm^3
Σ_T	Photon collision probability, cm^{-1}
Σ_a	Photon absorption probability, cm^{-1}
ΣQ_{FC}	Power deposited in fuel and neon circuit, kw
ΣQ_S	Power deposited in secondary hydrogen circuit, kw
σ	Stefan-Boltzmann constant, 0.56686×10^{-4} ergs/cm^2-sec-deg K
τ_ω	Optical depth, dimensionless
ϕ	Photon angular flux, photons/cm^2-sec-steradian
$\bar{\phi}$	Total photon flux at interval midpoint, photons/cm^2-sec
$\bar{\phi}^-$	Photon angular flux in negative R direction at interval midpoint, photons/cm^2-sec-unit solid angle
$\bar{\phi}^+$	Photon angular flux in positive R direction at interval midpoint, photons/cm^2-sec-unit solid angle
ϕ^-	Photon angular flux in negative R direction at interval boundary, photons/cm^2-sec-unit solid angle
ϕ^+	Photon angular flux in positive R direction at interval boundary, photons/cm^2-sec-unit solid angle

LIST OF SYMBOLS (Continued)

χ	Photon source density between λT and $\lambda T + \delta\lambda T$, photons/$cm^3$
χ'	Photon source density per unit time between λT and $\lambda T + \delta\lambda T$, photons/$cm^3$-sec
Ω	Unit direction vector
ω	Wave number, cm^{-1}

Subscripts

i	i^{th} region or interval
ℓ	ℓ^{th} temperature iteration
m	m^{th} Sn angular direction
o	Denotes reference condition

Superscript

j	j^{th} wave number group or wavelength group

APPENDIX A

EQUATIONS USED IN RADIANT HEAT TRANSFER ANALYSES

Flux Equations

The radiant heat transfer problem is solved using the steady-state Boltzmann transport equation. The generalized form of the transport equation is

$$\int_V \int_\Omega \Omega \cdot \nabla \phi(R,\Omega)\, d\Omega\, dV + \int_V \int_\Omega \Sigma_T(R)\, \phi(R,\Omega)\, d\Omega\, dV = \int_V \int_\Omega S(R,\Omega)\, d\Omega\, dV \quad \text{(A-1)}$$

The techniques used in deriving the difference equations for Eq. (A-1) were developed in the early 1950's and are referred to as the "Sn" method (Ref. 21). More recently, digital computer solutions of Eq. (A-1) have been extended by the "discrete ordinates Sn" method. The digital computer program employed in the present study is the one-dimensional code, ANISN (Ref. 18). The "discrete ordinates Sn" method used in the transport code is described in detail in Ref. 19. The principal assumption made in the method of discrete ordinates is that the integral of the flux over angle can be approximated by a Gaussian quadrature scheme.

$$\int_{-1}^{+1} \phi(X,\mu)\, d\mu = \sum^{\text{ANGLE}} \phi(X,\mu_d) W_d \quad \text{(A-2)}$$

where ϕ is the particle flux, X is the position in space, μ is the polar angle cosine, μ_d is the discrete polar angle cosine, and w_d is the weight associated with the direction whose cosine is μ_d. The quadrature scheme requires that the flux be calculated only at discrete angles.

For each of a specified number of wavelength groups, ANISN calculates particle angular fluxes, the directions of which are predetermined by an input set of constants. Consider a unit sphere with vectors extending radially outward along the "Sn" flux directions. In one-dimensional geometry, because of symmetry conditions, only one quadrant of the unit sphere is required in the flux calculation. For a given specified "Sn", the quadrant is divided into $n(n+4)/4$ solid angles with given weights, w_d. The "Sn" cosines (μ_d) extend from the + X direction to the -X direction and the weights, w_d, are the fraction of the surface area of the sphere which surrounds the point of intersection of the vector associated with the direction cosines and the unit sphere surface.

For each wavelength group, solid angle, and spatial mesh interval, ANISN solves a finite difference equation of the type .

$$\mu_d (A_{i+1} NN_{i+1,m} - A_i NN_{i,m}) + \frac{\alpha_{m+1/2}}{W_d} NN_{i+1/2,m+1/2} - \frac{\alpha_{m-1/2}}{W_d} NN_{i+1/2,m-1/2} + \Sigma_T V NN_{i+1/2,m} = SV \quad \text{(A-3)}$$

where m is a direction index, i is a spatial mesh index, N is the angular particle flux, A is an area element, V is a volume element, Σ_T is the collision probability, and S is the source. A linear approximation for the flux at the interval midpoint is assumed such that

$$NN_{i,m} = 2NN_{i+1/2,m} - NN_{i+1,m} ; \quad \text{FOR } \mu_d < 0 \quad \text{(A-4)}$$

or

$$NN_{i+1,m} = 2NN_{i+1/2,m} - NN_{i,m} ; \quad \text{FOR } \mu_d > 0 \quad \text{(A-5)}$$

It is also assumed that the flux is linear over angle at the interval midpoint such that

$$NN_{i+1/2,m+1/2} = 2NN_{i+1/2,m} - NN_{i+1/2,m-1/2} \quad \text{(A-6)}$$

During the process in which a particle traverses a curved mesh interval, the cosine, μ_d, associated with the particle's direction of travel is constantly changing. The terms containing the α coefficients in Eq. (A-3) account for the resulting angular redistribution. The entire flux distribution is then determined by successively sweeping over the spatial mesh, the discrete angular directions, and the wavelength groups.

A second computer program, TAXSI (temperature and cross-section source iteration) was written to calculate temperature dependent group absorption coefficients which

are averaged over each wavelength band. This same computer program, TAXSI, calculates the black-body source as a function of wavelength band, temperature and composition. The sources and absorption coefficients are required for the transport solution using the ANISN code. Iteration between the two programs (ANISN and TAXSI) is necessary to obtain a converged temperature distribution.

In addition to calculating sources and averaged absorption coefficients, TAXSI iterates until an energy balance between total energy source and total energy absorption in each different temperature interval is produced. This is accomplished by applying a perturbation technique either singularly or collectively to the different temperature intervals in the process of converging towards an energy balance. In applying the perturbation technique, a flux calculation less refined than that done by ANISN is done in TAXSI. The TAXSI flux calculation uses information calculated by ANISN related to the average cosine of the flux as a function of radius, direction and wavelength group. Whereas ANISN calculates the flux for many directions, TAXSI calculates perturbation fluxes for only two directions; radially inward and radially outward. ANISN also calculates the flux in a fine radial mesh while TAXSI is usually limited to calculating the flux in a more coarse spatial mesh. Simply stated, TAXSI imposes a less refined spatial and direction mesh than does ANISN for the flux calculation.

To calculate fluxes in the TAXSI program, the transport equation, Eq. (A-1), is rewritten in the form

$$L_1 - L_2 + \Sigma_T \phi V = SV \tag{A-7}$$

where L_1 is the particle leakage out of an interval and L_2 is the particle leakage into an interval. L_1 and L_2 are leakages associated with an interval's boundaries and are the product of the flux, ϕ, cosine of the polar angle, $(\frac{1}{\beta})$, and surface area, A. Since photons may traverse the interval in either direction, a set of equations were formulated for both basic directions. For the i^{th} interval, the outward directed flux, ϕ^+_{i+1}, was calculated from the equation

$$\frac{\phi^+_{i+1} A_{i+1}}{\beta^+_{i+1}} - \frac{\phi^+_i A_i}{\beta^+_i} + (\Sigma_T)_i \bar{\phi}^+_i V_i = S_i V_i \tag{A-8}$$

where it is assumed the average outward flux of the i^{th} interval, $\bar{\phi}^+_i$, is linear across the interval such that

$$\bar{\phi}^{+}_{i} = \left(\phi^{+}_{i+1} + \phi^{+}_{i}\right)/2 \qquad \text{(A-9)}$$

For the i^{th} interval, the inward directed flux, ϕ^{-}_{i}, was calculated from the equation

$$\frac{\bar{\phi}^{-}_{i} A_i}{\bar{\beta}_i} - \frac{\bar{\phi}^{-}_{i+1} A_{i+1}}{\bar{\beta}_{i+1}} + \left(\Sigma_T\right)_i \bar{\phi}^{-}_{i} V_i = S_i V_i \qquad \text{(A-10)}$$

where the average inward directed flux of the i^{th} interval, $\bar{\phi}^{-}_{i}$, is assumed linear across the interval such that $\bar{\phi}^{-}_{i} = (\phi^{-}_{i+1} + \phi^{-}_{i})/2$. The values of β are functions of wavelength group, radius and direction, and calculated from the detailed flux calculation of ANISN where

$$\beta^{+} = \frac{\int_{0}^{+1} \phi(\mu)\, d\mu}{\int_{0}^{+1} \phi(\mu)\mu\, d\mu} \quad \text{AND} \quad \beta^{-} = \frac{\int_{-1}^{0} \phi(\mu)\, d\mu}{\int_{-1}^{0} \phi(\mu)\mu\, d\mu} \qquad \text{(A-11)}$$

$\phi(\mu)$ is the angular flux as a function of polar angle, μ.

The value of the total flux in the i^{th} interval is then given as

$$\bar{\phi}_i = \left(\bar{\phi}^{+}_{i} + \bar{\phi}^{-}_{i}\right)/2 \qquad \text{(A-12)}$$

Opacity Weighting Technique

In the solution of the radiant heat transfer problem using the equations described herein, an integral mode of calculation is employed. The "multi-group" method is applied where the entire wavelength range of interest is divided into a finite number of smaller wavelength groups. In performing the flux calculation, the fundamental quantities which must be predetermined are the radiant energy source

and the opacity. The source is calculated as an integral quantity over the particular wavelength range of each wavelength group as discussed in a previous section. Note that the radiation source is transformed into a photon source for the transport calculation performed by ANISN. It is also necessary then to calculate opacities which are representative of the absorption coefficient averaged over each wavelength group. Three different averaging processes can be used for this purpose. The first is called a constant-flux weighting process given by

$$\bar{a}(\lambda_1 \rightarrow \lambda_2, T) = \int_{\lambda_1}^{\lambda_2} a(\lambda,T)\, d\lambda \Big/ \int_{\lambda_1}^{\lambda_2} d\lambda \qquad \text{(A-13)}$$

where $\bar{a}(\lambda_1 \rightarrow \lambda_2, T)$ is the wavelength group averaged opacity, and $a(\lambda,T)$ is the spectral absorption coefficient at temperature, T, as a function of wavelength, λ. This method is employed when the flux distribution is unknown for the interval in which this opacity is used.

A second method is a spectral-energy-flux weighting process given by

$$\bar{a}(\lambda_1 \rightarrow \lambda_2, T) = \int_{\lambda_1}^{\lambda_2} a(\lambda,T)\, I(\lambda T)\, d\lambda \Big/ \int_{\lambda_1}^{\lambda_2} I(\lambda T)\, d\lambda \qquad \text{(A-14)}$$

where $I(\lambda T)$ is the black-body spectral energy intensity as a function of wavelength. A similar weighting is a photon-number-flux weighting process given by

$$\bar{a}(\lambda_1 \rightarrow \lambda_2, T) = \frac{\frac{1}{hc} \int_{\lambda_1}^{\lambda_2} a(\lambda,T)\, I(\lambda T)\, \lambda\, d\lambda}{\frac{1}{hc} \int_{\lambda_1}^{\lambda_2} I(\lambda T)\, \lambda\, d\lambda} \qquad \text{(A-15)}$$

The last two weighting techniques are employed when it is known that the spectral distribution in the interval in which this opacity is to be used, is similar to black-body distributions at local temperatures. The spectral number flux weighted opacity is used in the transport calculation done by ANISN and TAXSI because the sources are constructed as photon rather than energy sources.

Convection Equations

A convection model was formulated to include the removal of radiant energy absorbed in the buffer region in the energy balance. The principal assumption employed in the convection flow model is that of constant axial dynamic pressure in the buffer region. This condition is expressed as

$$\Delta P_z = 9.68 \times 10^{-4} \frac{\rho V_z^2}{2g} \qquad \text{(A-16)}$$

where ρ, V_z and g are the local buffer-gas density, local gas axial velocity and gravitational constant. The local gas density is obtained from the ideal gas law. The axial buffer-gas weight flow is given by

$$W_{BZ} = 2\pi \int_{R_6}^{R_2} \rho V_z^2 \, R \, dR \qquad \text{(A-17)}$$

where R_2 and R_6 are the radial boundaries of the buffer-gas region. From continuity of mass relations, the total radial buffer-gas weight flow, W_{BR}, is equivalent to the total axial buffer-gas weight flow. The energy convected by the buffer-gas flow rate can then be evaluated from

$$Q_C = W_{BR} \, c_p(T) \Delta T \qquad \text{(A-18)}$$

where c_p (T) is the specific heat as a function of temperature for the buffer gas and ΔT is the radial temperature drop in the buffer-gas region.

TABLE I

REFERENCE ENGINE DESIGN CHARACTERISTICS

The reference nuclear light bulb engine design has the following characteristics:	
Cavity Configuration	Seven separate, 6-ft-long cavities having a total overall volume of 170 ft^3
Cavity Pressure	500 atm
Specific Impulse	1870 sec
Total Propellant Flow (including seed and nozzle transpiration coolant flow)	49.3 lb/sec
Thrust	92,000 lb
Engine Power	4600 megw
Engine Weight	70,000 lb
Ratio of Average Density in Fuel-Containment Region to Neon Density at Edge of Fuel	0.7
Equivalent Axial-Flow Reynolds Number in Neon Vortex	5500

TABLE II

FULL-POWER, STEADY-STATE MODERATOR AND STRUCTURE HEAT DEPOSITION RATES

Fuel - U-233

Region	Mechanism of Heating	Reference Engine Heat Deposition Rate, Megw (Ref. 4)	Modification I Heat Deposition Rate, Megw**
Pressure Vessel	Neutron and Gamma	11.55*	11.55
Nozzles	Neutron and Gamma	0.08	0.08
Flow Divider	Neutron and Gamma and Conduction	7.15	7.15
Tie Rods	Neutron and Gamma and Conduction	5.39	5.39
Cavity End Walls	Thermal Radiation and Conduction	6.40	73.0
Cavity Liner	Thermal Radiation and Conduction	81	112.0
Transparent Structure	Thermal Radiation and Conduction	119	65.5
Fuel Recycle System	Removal of Heat from Fuel	64	70.7
Upper and Lower End Moderator	Neutron and Gamma	70.0	70.0
Beryllium Oxide Moderator	Neutron and Gamma	89.5	89.5
Graphite Moderator	Neutron and Gamma	48.6	48.6
Direct Hydrogen Heating	Neutron and Gamma	58.9	58.0
TOTAL		561.57	612.37
PERCENT OF TOTAL POWER		12.2	13.3

*Total heating in pressure vessel is 16.5 megw. It is assumed that only 2/3 of the total will be removed by the closed secondary hydrogen coolant circuit and the remaining 1/3 will be removed by the hydrogen which is used for transpiration cooling of the exhaust nozzles.

**Assumes seed material in fuel and buffer regions which blocks uv radiation.

TABLE III

SHUTDOWN SCHEDULE

I.	Time After Initiation of Shutdown, $t_s = 0$
	1. Close Fuel Injection Control Valve, $W_F = 0$
	2. Begin Linear Decrease in Propellant Flow Rate, $W_P = 18.6 - .465\ t_s$ kg/sec
	3. Begin Linear Increase in Radiator Flow Rate, $W_R = .465\ t_s$ kg/sec
	4. Maintain Secondary Circuit and Cavity Neon Flow at Full Power Value
II.	Time After Initiation of Shutdown, $t_s = 6$ sec
	1. No Power Generated Due to Fission in Fuel Region
III.	Time After Initiation of Shutdown, $t_s = 36$ sec
	1. Hold Constant Value of Propellant Flow, $W_P = 1.86$ kg/sec
	2. Hold Constant Value of Radiator Flow, $W_R = 16.74$ kg/sec
IV.	Time After Initiation of Shutdown, $t_s = 200$ sec
	1. Reduce Propellant Flow Rate, W_P, to Zero
	2. Increase Radiator Flow Rate, W_R, to 18.6 kg/sec
	3. Close Exhaust Nozzle to Maintain Engine Pressure at $\approx$ 18 atm
V.	Time After Initiation of Shutdown, $t_s > 200$ sec
	1. Continue to Remove Afterheat Through Neon and Secondary Circuits and Reject Through Heat Exchangers to Radiator

Power Variation with Time	Fig. 11
Coolant Flow Schedule, Propellant and Radiator	Fig. 12
Average Fuel Temperature Variation with Time	Fig. 13
Beryllium Oxide Temperature Variation with Time	Fig. 16
Graphite Temperature Variation with Time	Fig. 17
Pressure Variation with Time	Fig. 18
Afterheat Power Variation with Time	Fig. 7

TABLE IV

HEAT REMOVAL REQUIREMENTS AFTER SHUTDOWN

Heat Removal by Direct Net Hydrogen Coolant Flow Out of Engine, No Space Radiator	
Moderator Sensible Heat, kw-sec (Btu)	1.64×10^7 (1.554×10^7)
Induced Radioactivity Heat, kw-sec (Btu)	5.36×10^5 (5.09×10^5)
Fission Product Heat, kw-sec (Btu)	
Engine Run Time, sec	
100	1.82×10^7 (1.725×10^7)
300	4.35×10^7 (4.11×10^7)
500	6.46×10^7 (6.13×10^7)
1000	1.098×10^8 (1.04×10^8)
1500	1.5×10^8 (1.42×10^8)
Total Hydrogen Required for all Heat Sources Per Engine Run, kg (lb)	
Engine Run Time, sec	
100	3330 (7350)
300	5715 (12,620)
500	8065 (17,800)
1000	12,000 (26,400)
1500	17,600 (38,800)
Heat Removal by Space Radiator, No Net Hydrogen Flow	
Required Rate of Sensible Heat Removal From Moderator, kw (Btu/sec)	4050 (3860)
Maximum Power Due to Induced Radioactivity, kw (Btu/sec)	6017 (5700)
Maximum Power Due to Fission Products, kw (Btu/sec)	
Engine Run Time, sec	
100	1.045×10^5 ($.99 \times 10^5$)
300	1.37×10^5 (1.30×10^5)
500	1.50×10^5 (1.42×10^5)
1000	1.65×10^5 (1.56×10^5)
1500	1.72×10^5 (1.63×10^5)
Required Radiator System Weight, kg (lb) Based on Aluminum Radiator, Inlet Temperature 833 K (1500 R), Outlet Temperature 389 K (700 R)	
Engine Run Time, sec	
100	3340 (7350)
300	4390 (9650)
500	4800 (10,500)
1000	5290 (11,600)
1500	5500 (12,100)

TABLE V

RADIATION DOSE RATE AFTER ENGINE SHUTDOWN

Values Shown are for 1000 sec Engine Run Time

Each Component is Considered to Emit Radiation as an Unshielded Point Source

CASE I

Assumptions: (1) Perfect Separation of Fuel and High Temperature Fission Products,
(2) No Plating of Fission Products or Fuel in Cavity Region

Time After Engine Shutdown, sec	0.5×10^6	1.0×10^6	2.0×10^6
LOCATION			
Dose Rate, r/hr at 1 ft:			
Neon Gas	1.92×10^6	1.52×10^6	0.720×10^6
Heat Exchanger	1.80×10^6	1.42×10^6	0.676×10^6
Fuel Storage	5.3×10^6	4.19×10^6	1.99×10^6

CASE II

Assumptions: (1) Separation of Fuel and Fission Products 80 Percent Efficient Remainder of Fuel and Fission Products in Heat Exchanger,
(2) No Plating of Fission Products or Fuel in Cavity Region

Time After Engine Shutdown, sec	0.5×10^6	1.0×10^6	2.0×10^6
LOCATION			
Dose Rate, r/hr at 1 ft:			
Neon Gas	1.92×10^6	1.52×10^6	0.720×10^6
Heat Exchanger	2.86×10^6	2.26×10^6	1.066×10^6
Fuel Storage	4.24×10^6	3.35×10^6	1.60×10^6

CASE III

Assumptions: (1) 5-Å-Thick Coating of Fuel and Fission Products Plated on Transparent Structure and End-Wall Surfaces

Time After Engine Shutdown, sec	0.5×10^6	1.0×10^6	2.0×10^6

TABLE V (Continued)

LOCATION			
Dose Rate, r/hr at 1 ft:			
Transparent Structure and End Walls	13.4	10.6	5.04
Neon Gas	Same as Case I or Case II		
Heat Exchanger	Depending on Assumptions Made		
Fuel Storage	Relative to Location of Fuel Deposition		

TABLE VI

VARIATION OF FRACTION OF RADIANT ENERGY AT EDGE OF FUEL BELOW WAVELENGTH CUTOFFS OF BeO AND SiO_2 WITH ENGINE POWER AND NO/O_2 SEED PRESSURE

Relative Power $\frac{Q}{Q_o}$	Effective Radiating Temperature T^*, deg K	NO/O_2 Seed Pressure - atm	Energy Fraction Below BeO $\lambda_{CUTOFF} = .125$	Energy Fraction Below SiO_2 $\lambda_{CUTOFF} = .18$
1	8330	0.0	0.0531	0.135
1	8330	0.01	0.0531	0.135
1	8330	0.10	0.0375	0.1205
1	8330	1.0	0.031	0.1135
1	8330	10.0	0.022	0.092
1	8330	200.0	0.0018	0.0085
5	12460	0.0	0.0548	0.138
10	14820	0.0	0.0812	0.188
100	26350	0.0	0.341	0.677

FIG. 1

NUCLEAR LIGHT BULB PERFORMANCE CHARACTERISTICS

PROPELLANT EXIT TEMPERATURE EQUAL TO 0.8T*

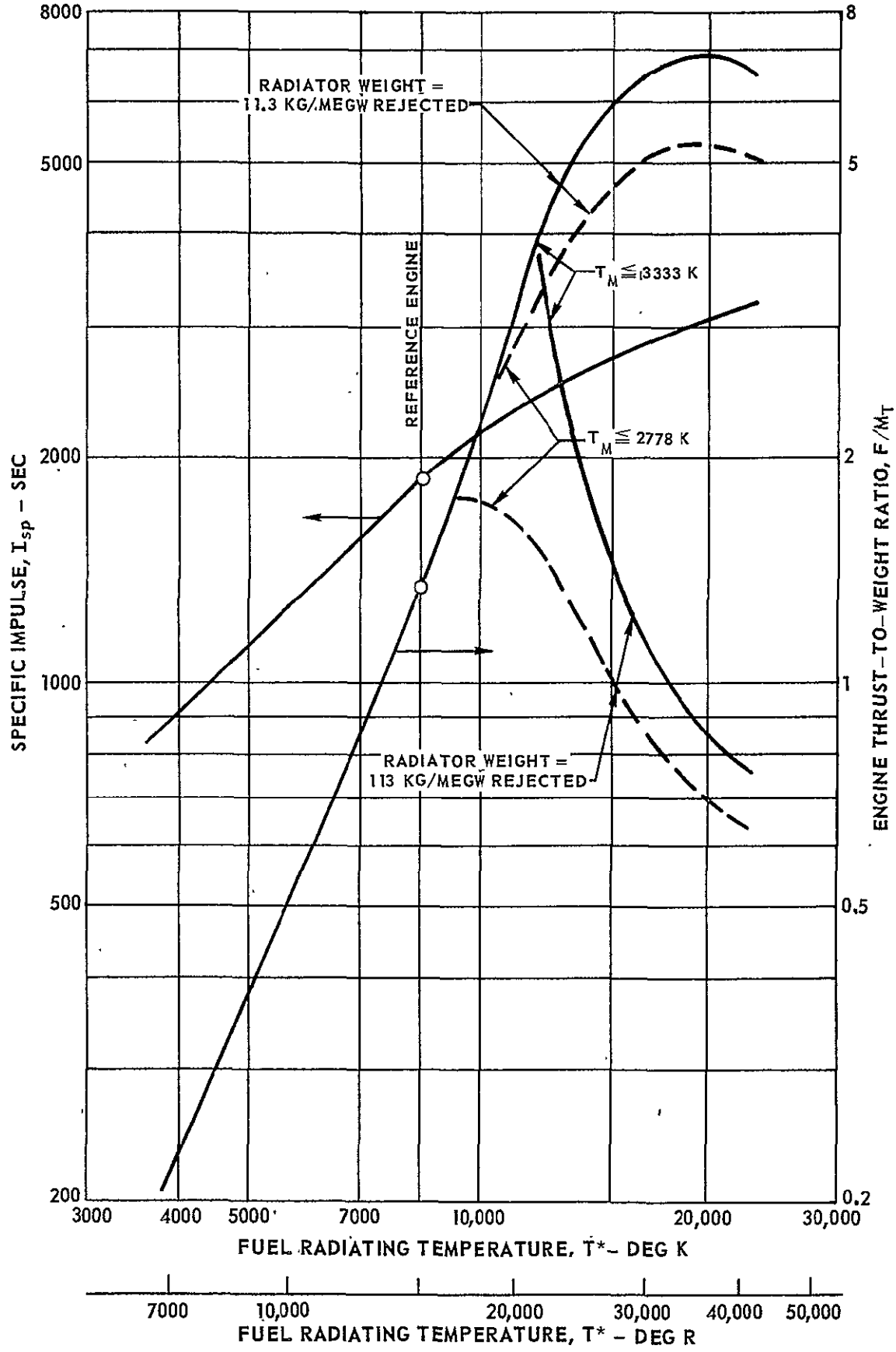

FIG. 2

VARIATION OF ENGINE POWER, THRUST, WEIGHT, OPERATING PRESSURE AND PROPELLANT WEIGHT FLOW WITH FUEL RADIATING TEMPERATURE

PROPELLANT EXIT TEMPERATURE EQUAL TO 0.8T*

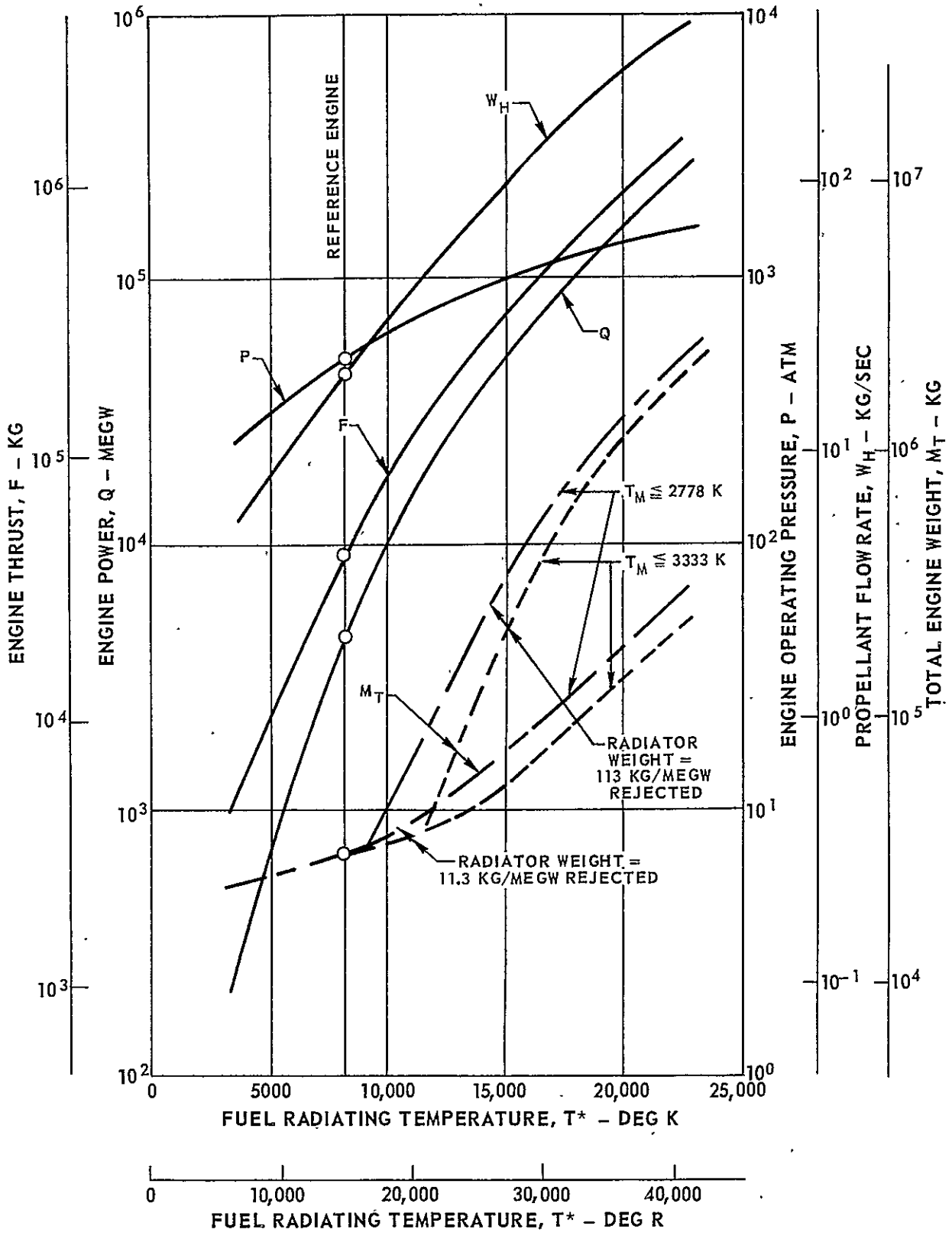

NUCLEAR LIGHT BULB FLOW DIAGRAM USED FOR ENGINE DYNAMICS STUDIES

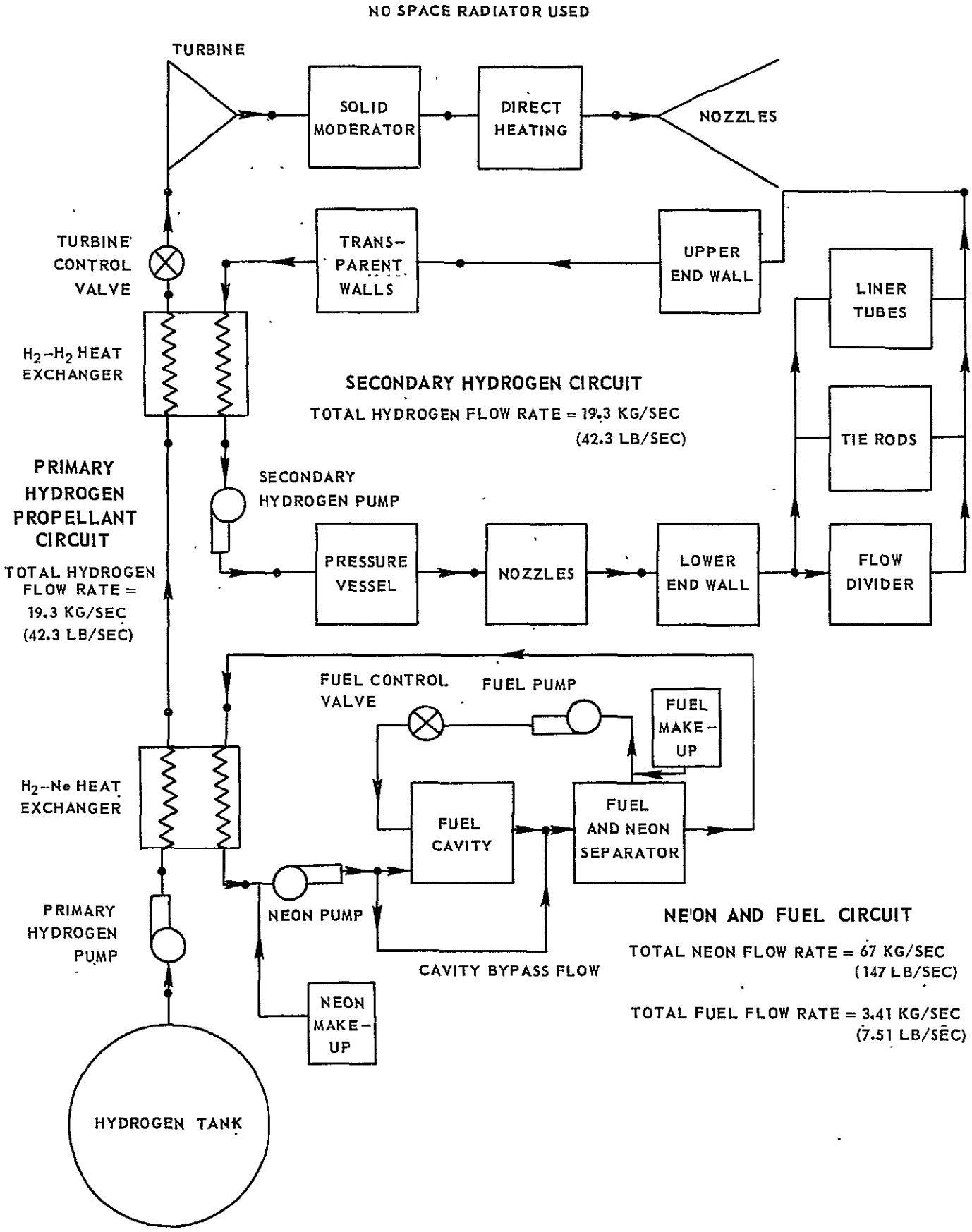

BLOCK DIAGRAM OF ENGINE CONTROL SYSTEM

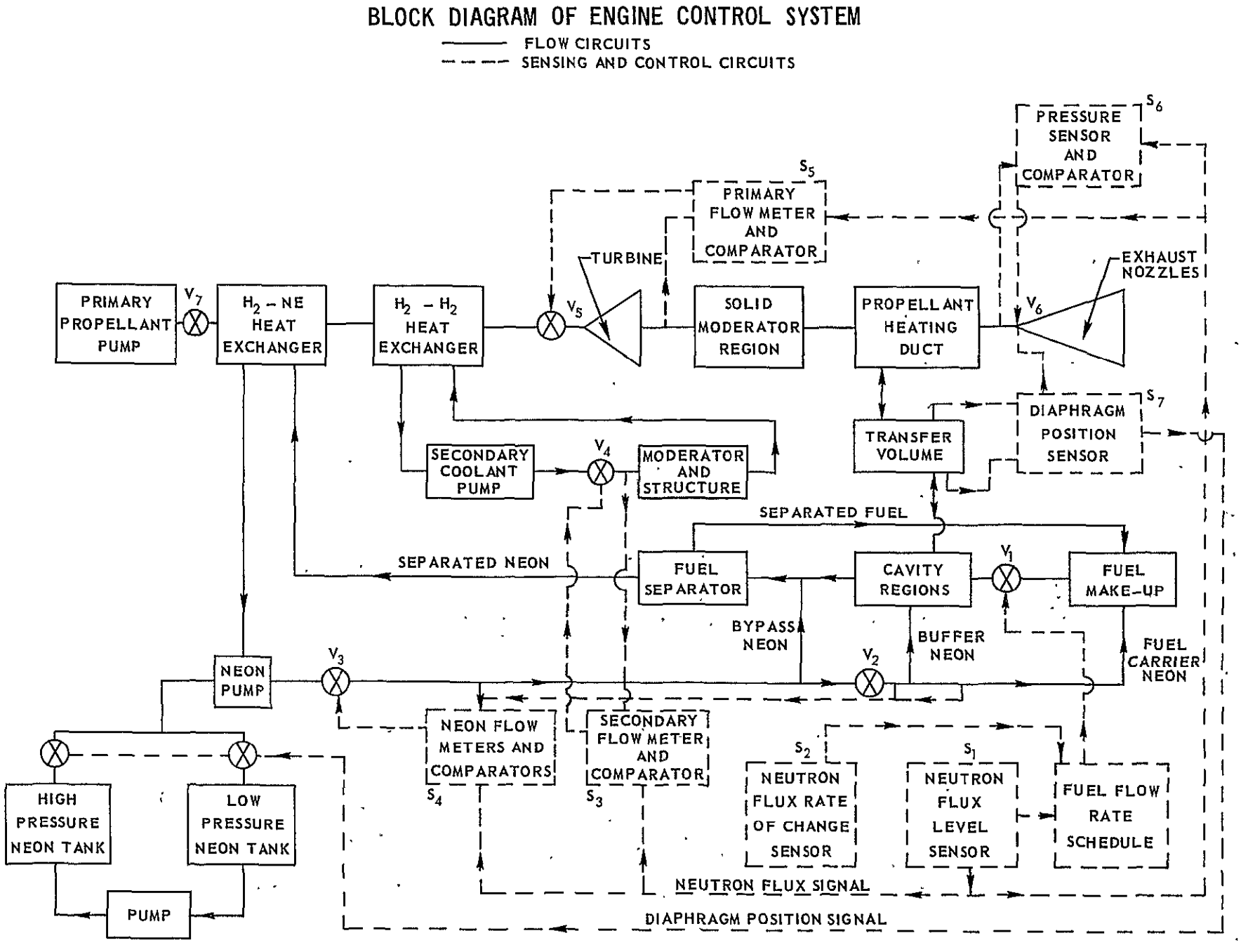

FIG. 4

POWER LEVEL RESPONSES OF CONTROLLED ENGINE TO STEP CHANGES IN IMPOSED REACTIVITY

$$\delta K = \delta K_0 + \delta K_1 + \delta K_2$$

SEE TEXT FOR DESCRIPTION OF δK_0, δK_1, δK_2 AND CONTROL METHOD

(a) STEP INCREASE IN IMPOSED REACTIVITY

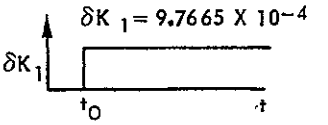

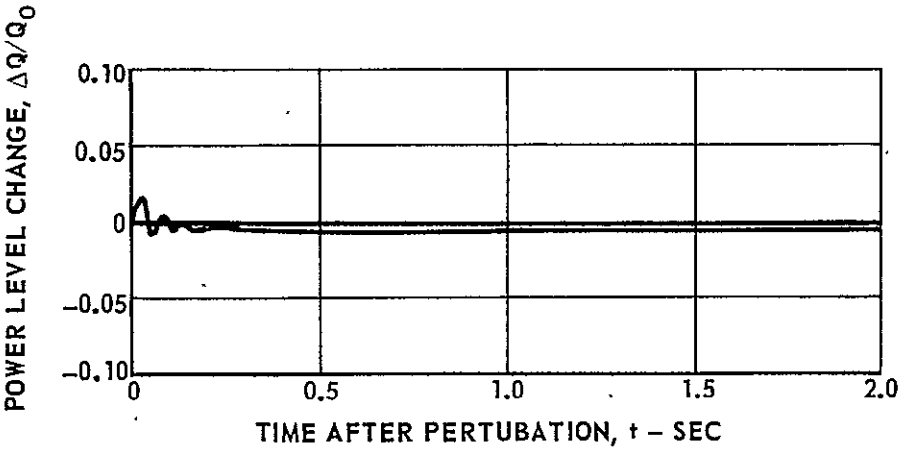

(b) STEP DECREASE IN IMPOSED REACTIVITY

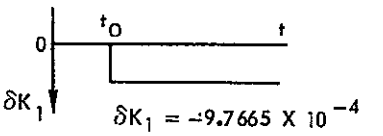

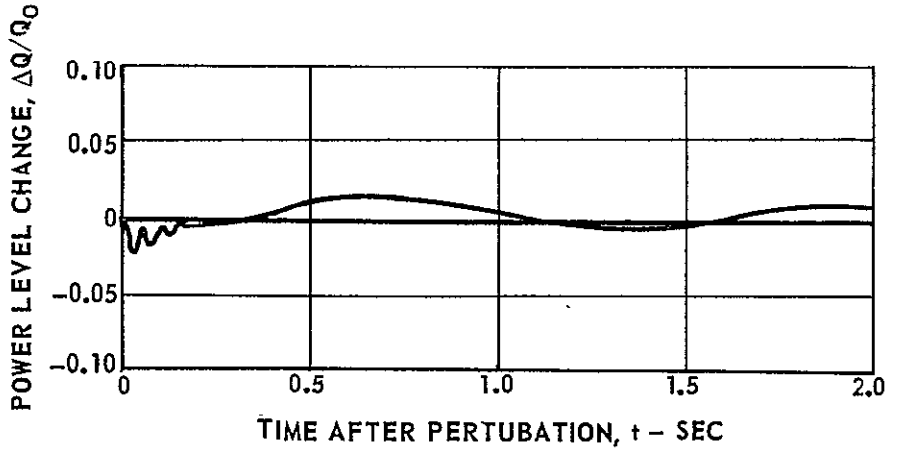

POWER LEVEL RESPONSES OF CONTROLLED ENGINE TO STEP CHANGES IN FUEL INJECTION CONTROL VALVE AREA

$$W_F = K_F A_F \left(\frac{P_I - P_T}{0.25}\right)^{1/2}$$

$$A_F = (A_F)_0 + \delta A_{F1} + \delta A_{F2}$$

SEE TEXT FOR DESCRIPTION OF δA_{F1} , δA_{F2} AND CONTROL METHOD

(a) INITIAL STEP INCREASE IN CONTROL VALVE AREA

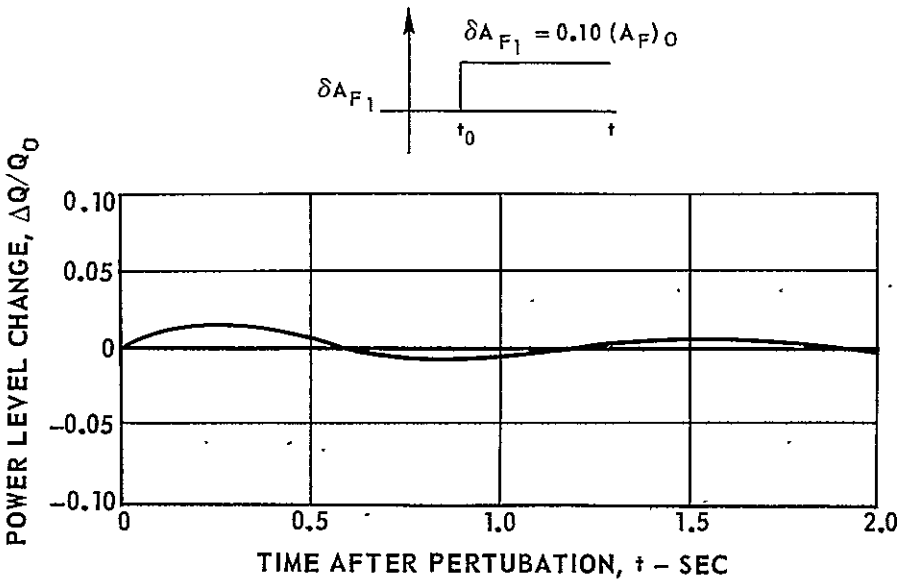

(b) INITIAL STEP DECREASE IN CONTROL VALVE AREA

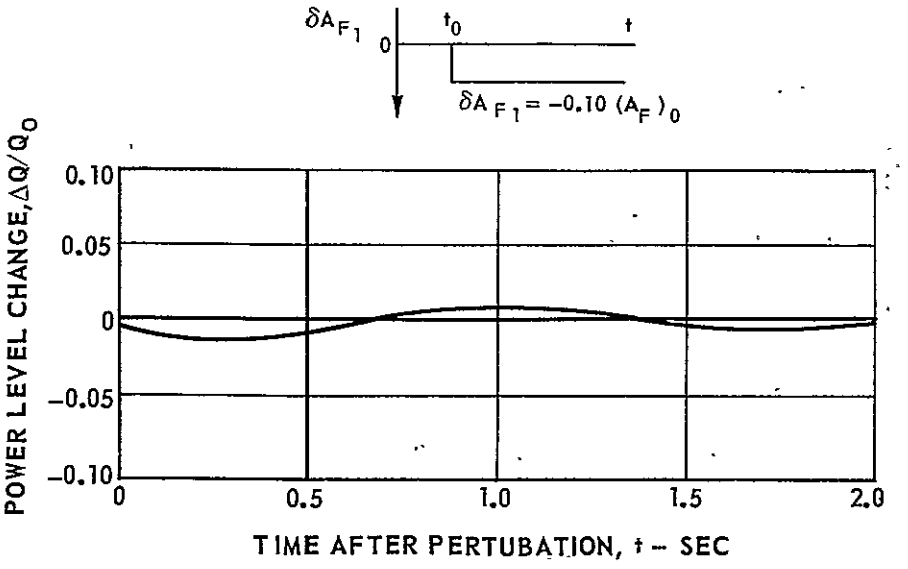

POWER LEVEL RESPONSES OF CONTROLLED ENGINE TO STEP CHANGES IN EXHAUST NOZZLE AREA

$A^*_O = 37.1\ CM^2\ (4.004 \times 10^{-2}\ FT^2)$

SEE TEXT FOR DESCRIPTION OF CONTROL METHOD

(a) STEP INCREASE IN NOZZLE AREA

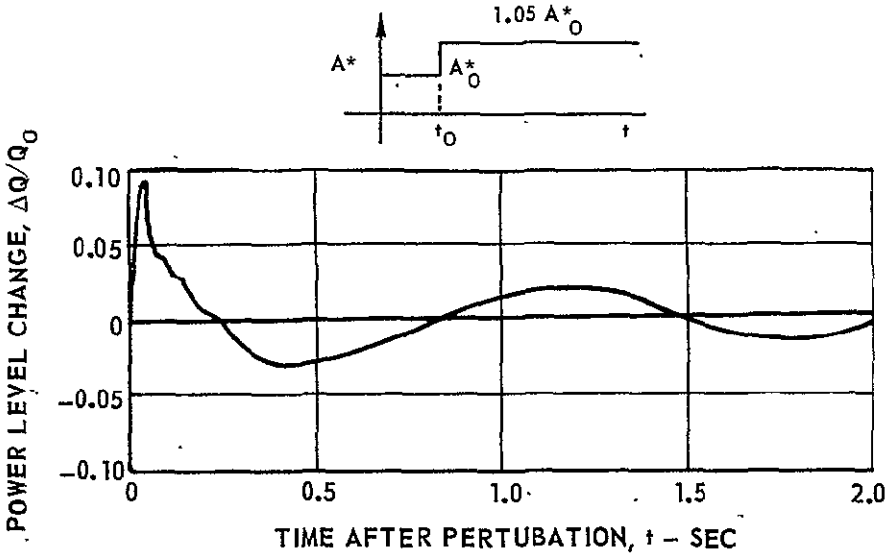

(b) STEP DECREASE IN NOZZLE AREA

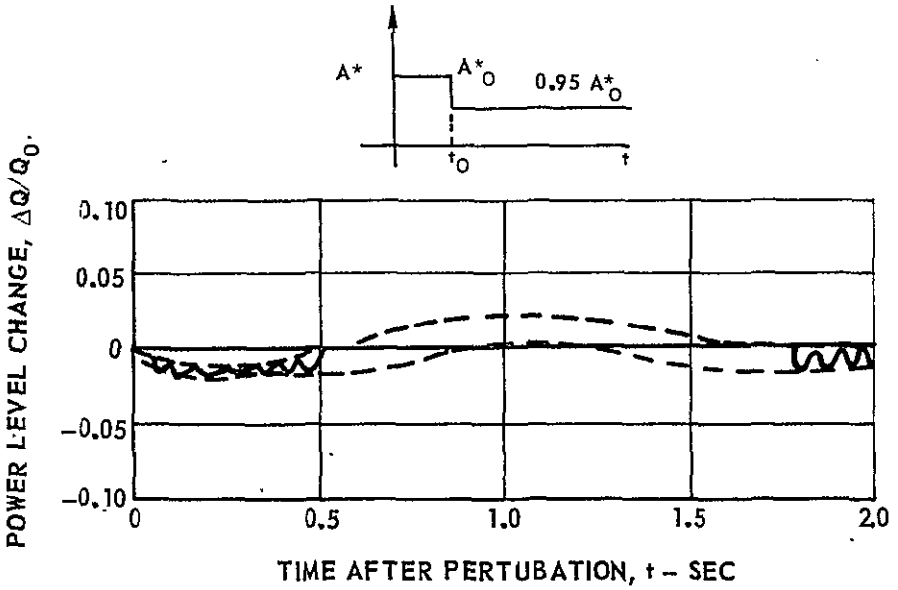

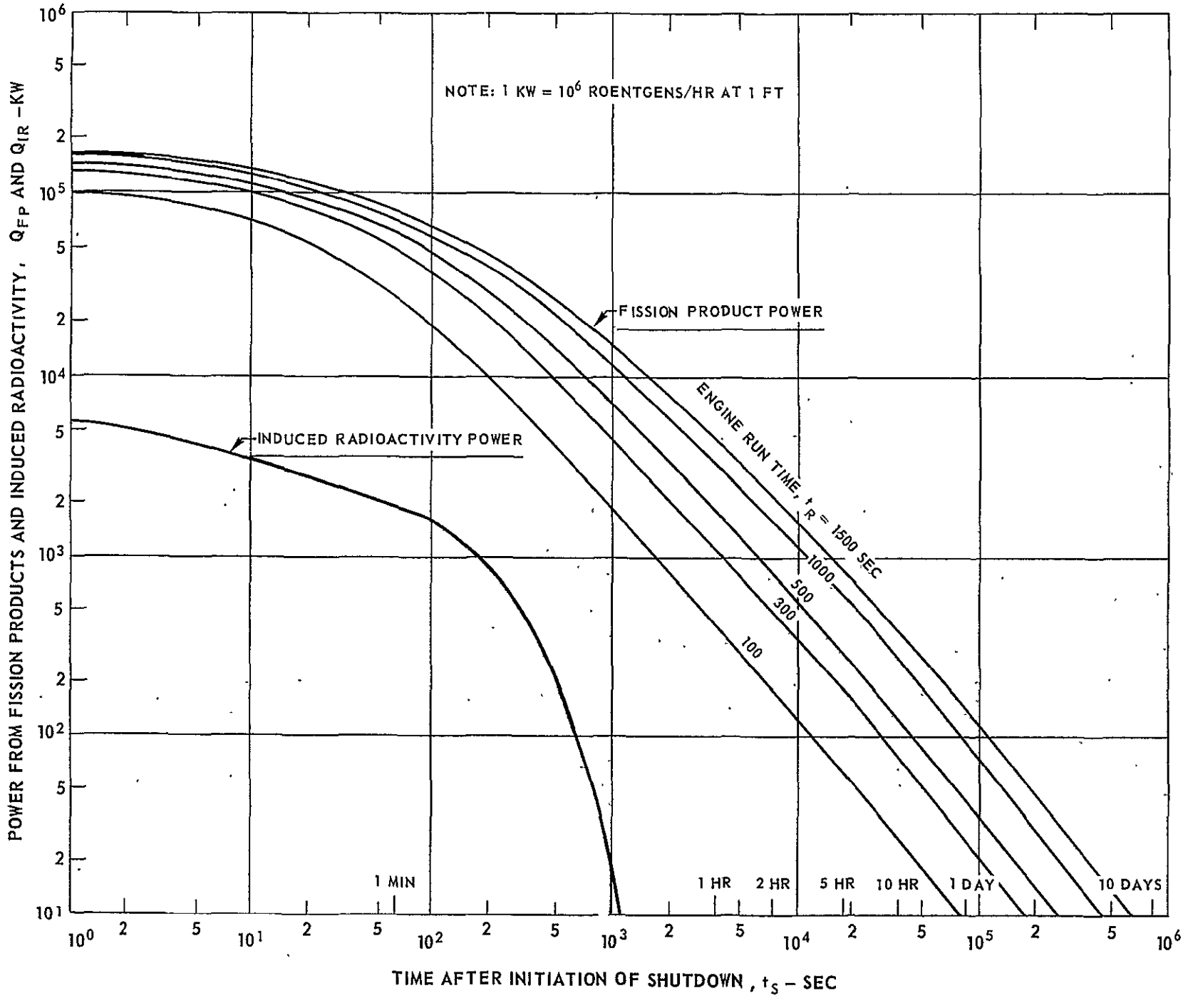
VARIATION OF FISSION-PRODUCT AND INDUCED RADIOACTIVITY POWER WITH TIME AFTER ENGINE SHUTDOWN
NOTE: 1 KW = 10^6 ROENTGENS/HR AT 1 FT
FISSION PRODUCT POWER
INDUCED RADIOACTIVITY POWER
ENGINE RUN TIME, t_R = 1500 SEC
1000
500
300
100
1 MIN
1 HR
2 HR
5 HR
10 HR
1 DAY
10 DAYS
POWER FROM FISSION PRODUCTS AND INDUCED RADIOACTIVITY, Q_FP AND Q_IR - KW
TIME AFTER INITIATION OF SHUTDOWN, t_S - SEC

FIG. 8

VARIATION OF TOTAL HEAT RELEASE FROM FISSION PRODUCTS AND INDUCED RADIOACTIVITY WITH TIME AFTER ENGINE SHUTDOWN

1.0 BTU = 1.055 KW–SEC

$$E = \int_{t_o}^{t_s} Q\,dt$$

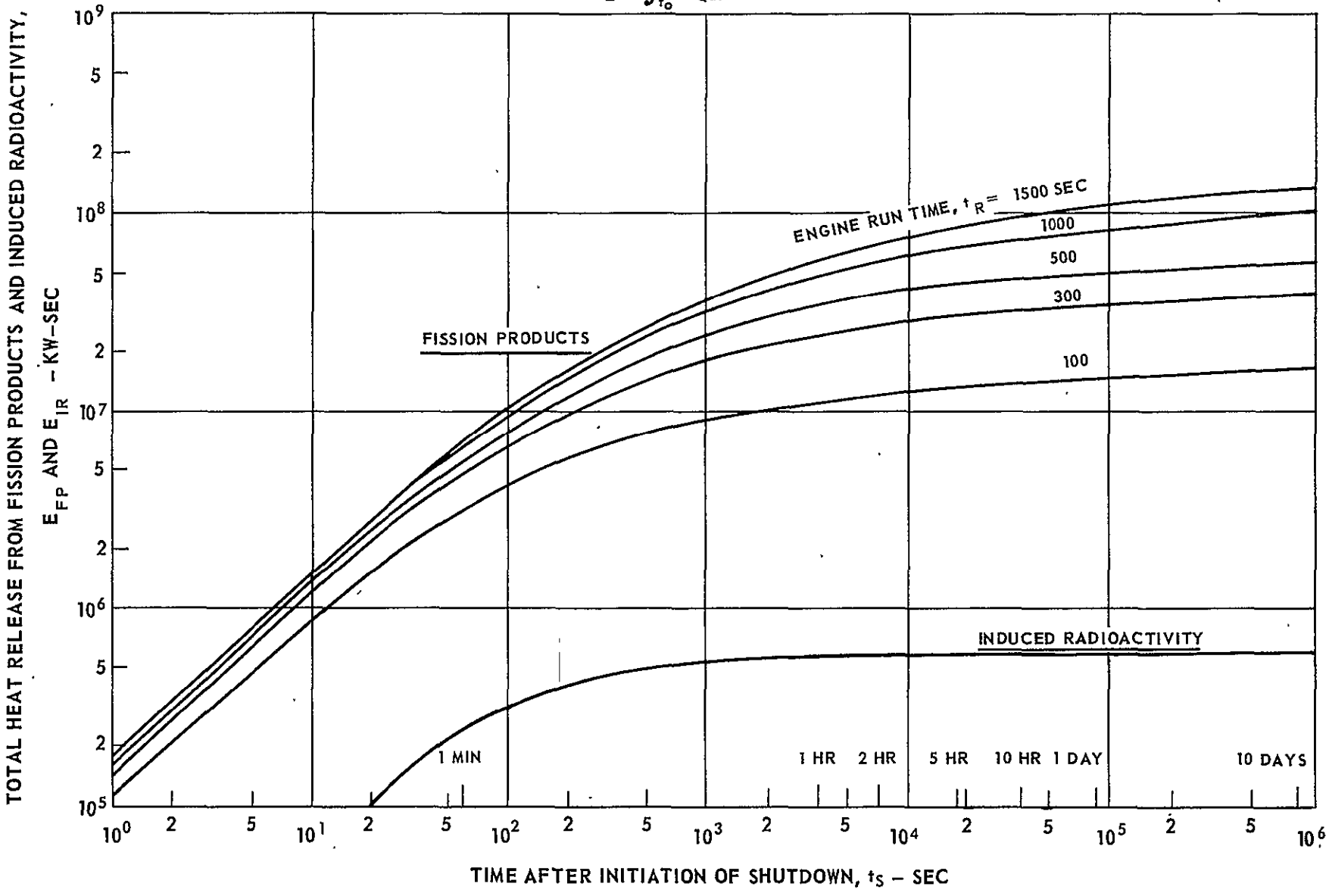

FIG. 9

EFFECT OF RADIATOR COOLANT OUTLET TEMPERATURE ON SPACE RADIATOR WEIGHT

HYDROGEN COOLANT

POWER REJECTED BY RADIATOR = 115 MEGW (2.5 PERCENT OF REFERENCE ENGINE TOTAL POWER)

TUBE ID = 0.61 CM (0.24 IN.), NUMBER OF TUBES = 6000

INLET TEMPERATURE BASED ON MAXIMUM ALLOWABLE TEMPERATURE FOR RADIATOR MATERIAL

TUBE WALL THICKNESS BASED ON TENSILE STRENGTH REQUIRED FOR INTERNAL PRESSURE OF 100 ATM

SYMBOL	RADIATOR MATERIAL	RADIATOR INLET TEMPERATURE, $(T_R)_{IN}$ DEG K	TUBE WALL AND FIN THICKNESS, CM	MATERIAL DENSITY, GM/CM^3
———	STEEL	1390	0.0795	7.85
— — —	ALUMINUM	833	0.0795	2.72
— — —	TUNGSTEN	1945	0.0397	19.05

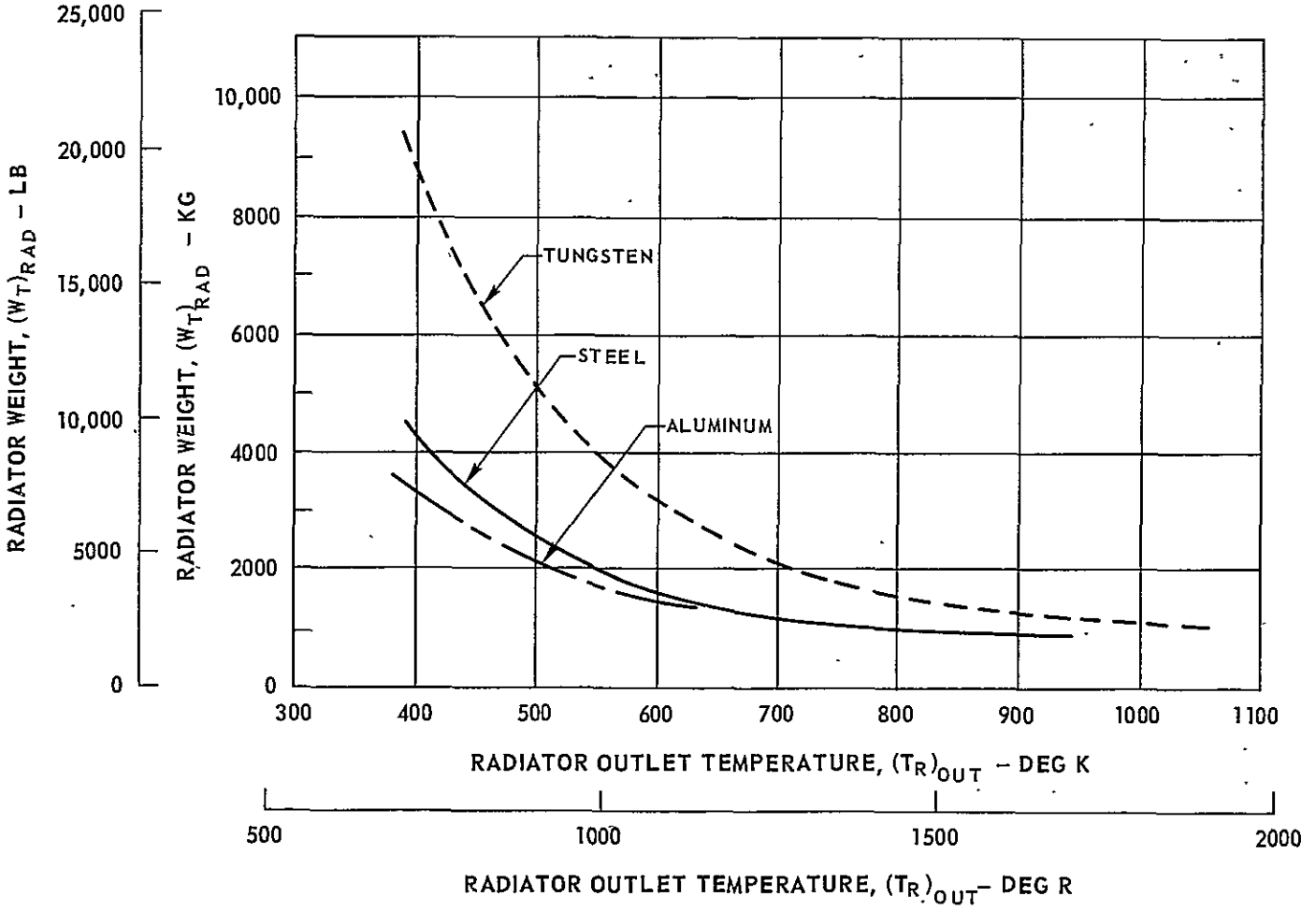

EFFECT OF RADIATOR COOLANT OUTLET TEMPERATURE ON PRESSURE LOSS IN SPACE RADIATOR

HYDROGEN COOLANT

POWER REJECTED BY RADIATOR = 115 MEGW (2.5 PERCENT OF REFERENCE ENGINE TOTAL POWER)

TUBE ID = 0.61 CM (0.24 IN.), NUMBER OF TUBES = 6000

MAXIMUM OPERATING PRESSURE = 100 ATM

INLET TEMPERATURE BASED ON MAXIMUM ALLOWABLE TEMPERATURE FOR RADIATOR MATERIAL

TUBE WALL THICKNESS BASED ON TENSILE STRENGTH REQUIRED FOR INTERNAL PRESSURE OF 100 ATM

SYMBOL	RADIATOR MATERIAL	RADIATOR INLET TEMPERATURE, $(T_R)_{IN}$ DEG K	TUBE WALL AND FIN THICKNESS, CM	MATERIAL DENSITY, GM/CM^3
———	STEEL	1390	0.0795	7.85
— — —	ALUMINUM	833	0.0795	2.72
— — —	TUNGSTEN	1945	0.0397	19.05

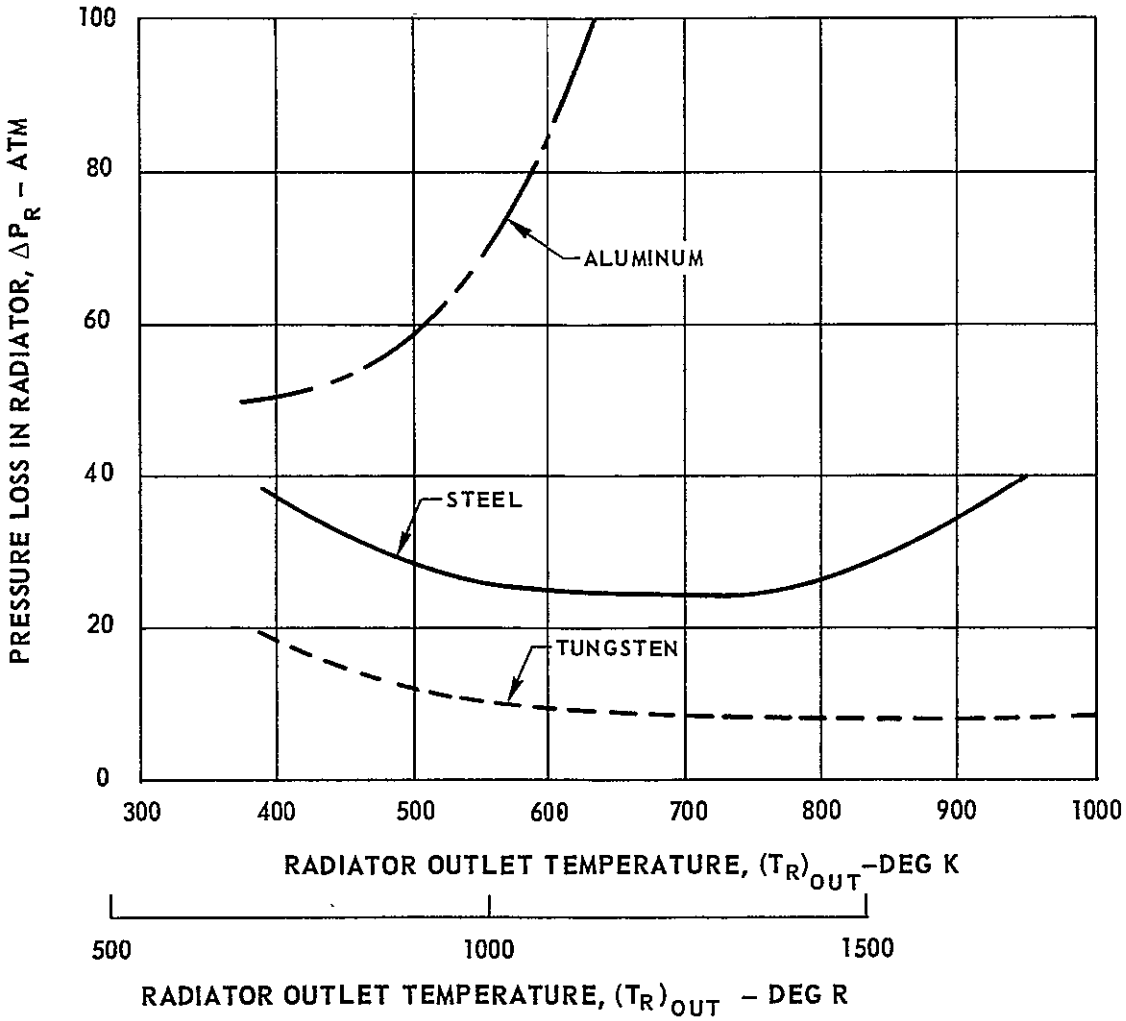

FIG. 12

VARIATION OF ENGINE POWER LEVEL DURING SHUTDOWN

TIME TO ZERO POWER = 6 SEC

STEADY-STATE ENGINE POWER LEVEL, Q_O = 4600 MEGW

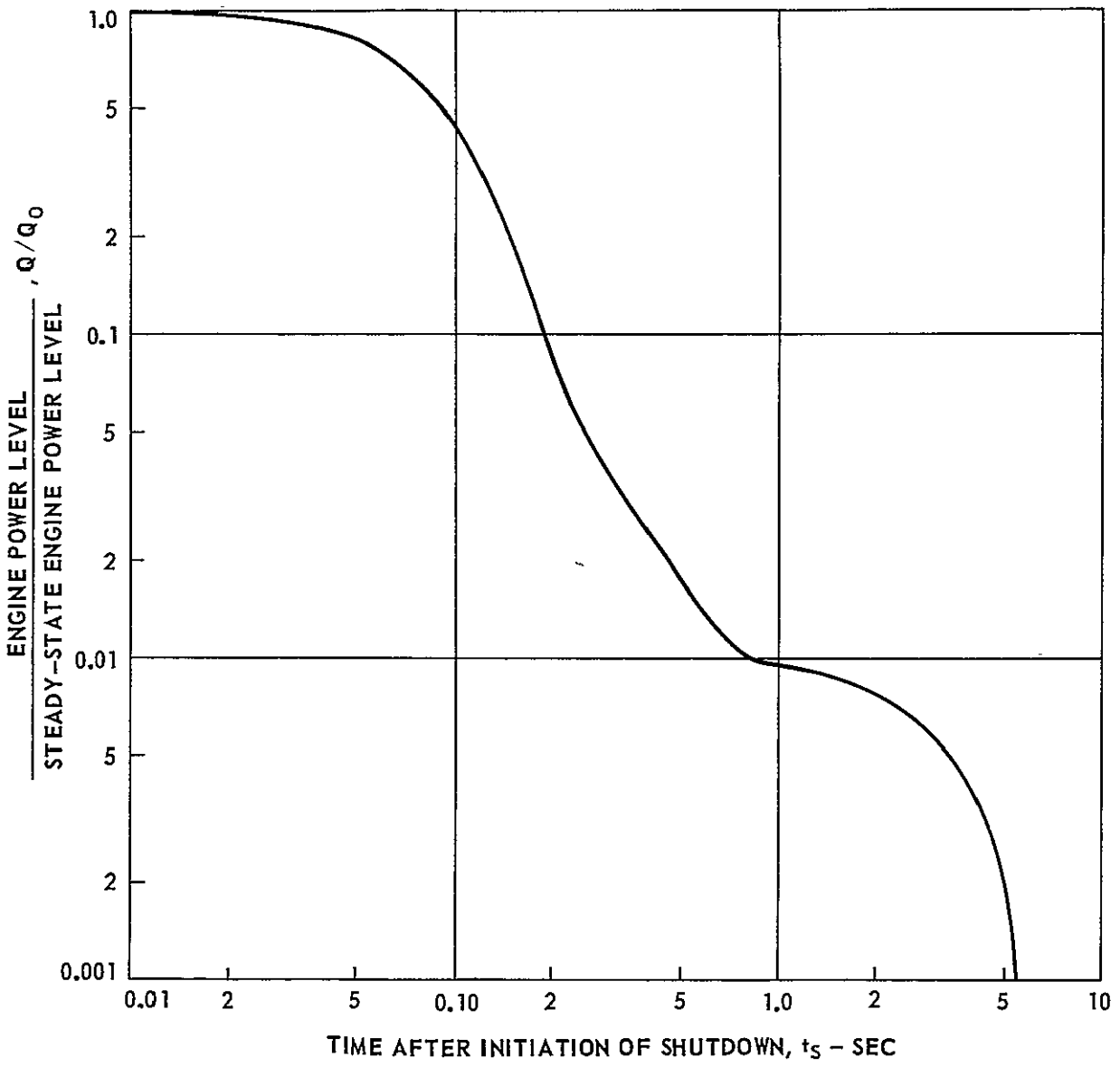

AVERAGE FUEL TEMPERATURE DURING ENGINE SHUTDOWN

SEE FIG. 12 FOR SHUTDOWN POWER PROFILE

TIME TO ZERO FISSION POWER = 6 SEC

SEE FIG. 14 FOR COOLANT FLOW SCHEDULES

STEADY-STATE AVERAGE FUEL TEMPERATURE, T_{F_0} = 25,000 K

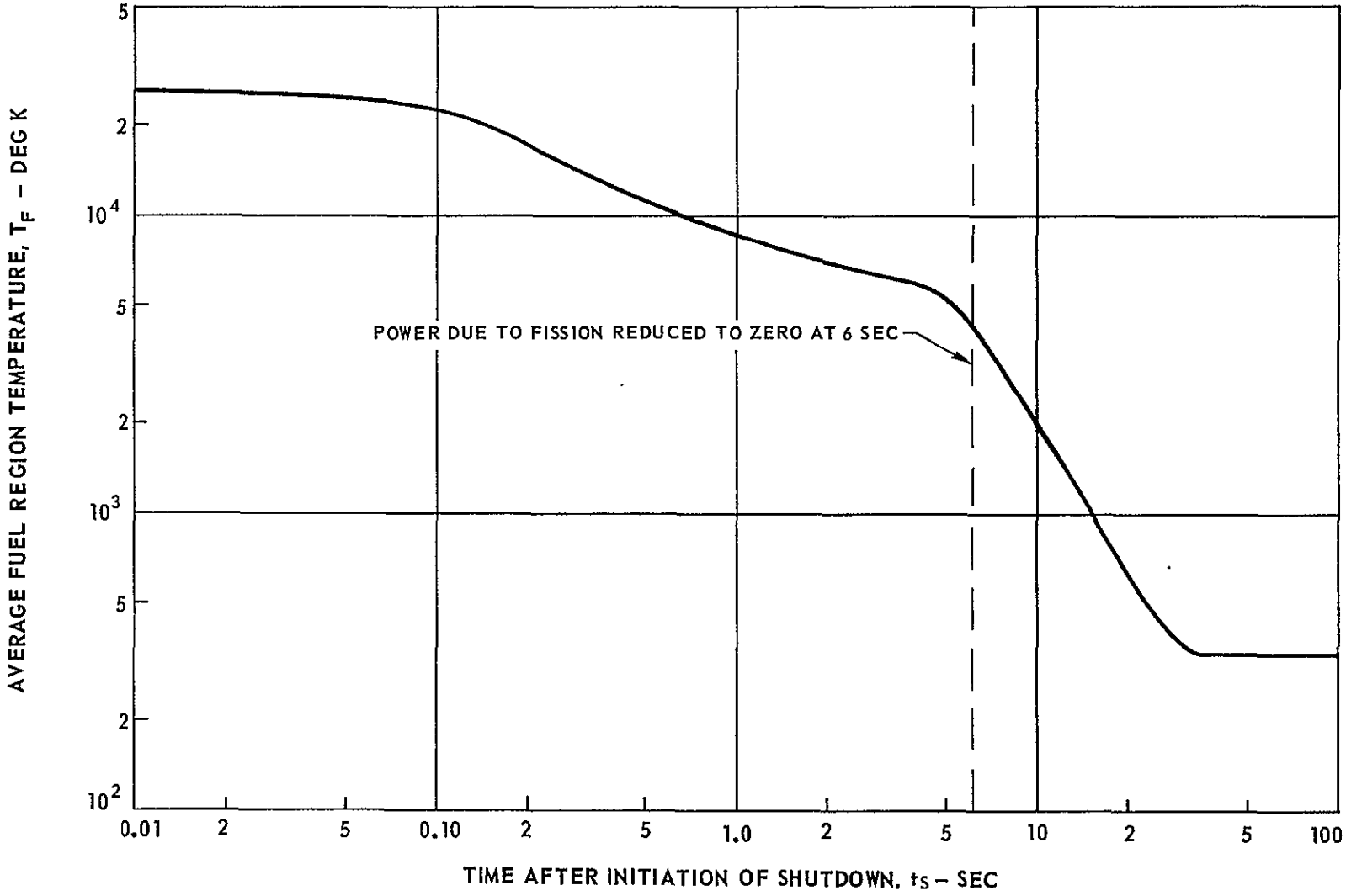

FIG. 13

PROPELLANT AND RADIATOR HYDROGEN FLOW RATES DURING ENGINE SHUTDOWN

SPACE RADIATOR COOLING LOOP PASSES THROUGH H_2 – Ne AND H_2 – H_2 HEAT EXCHANGERS

AND THEN TO SPACE RADIATOR – SEE FIG. 3 FOR HEAT EXCHANGER LOCATIONS

STEADY-STATE PROPELLANT FLOW RATE, W_{H_O} = 19.3 KG/SEC

SECONDARY HYDROGEN COOLANT FLOW RATE CONSTANT DURING SHUTDOWN, W_{H_S} = 19.3 KG/SEC

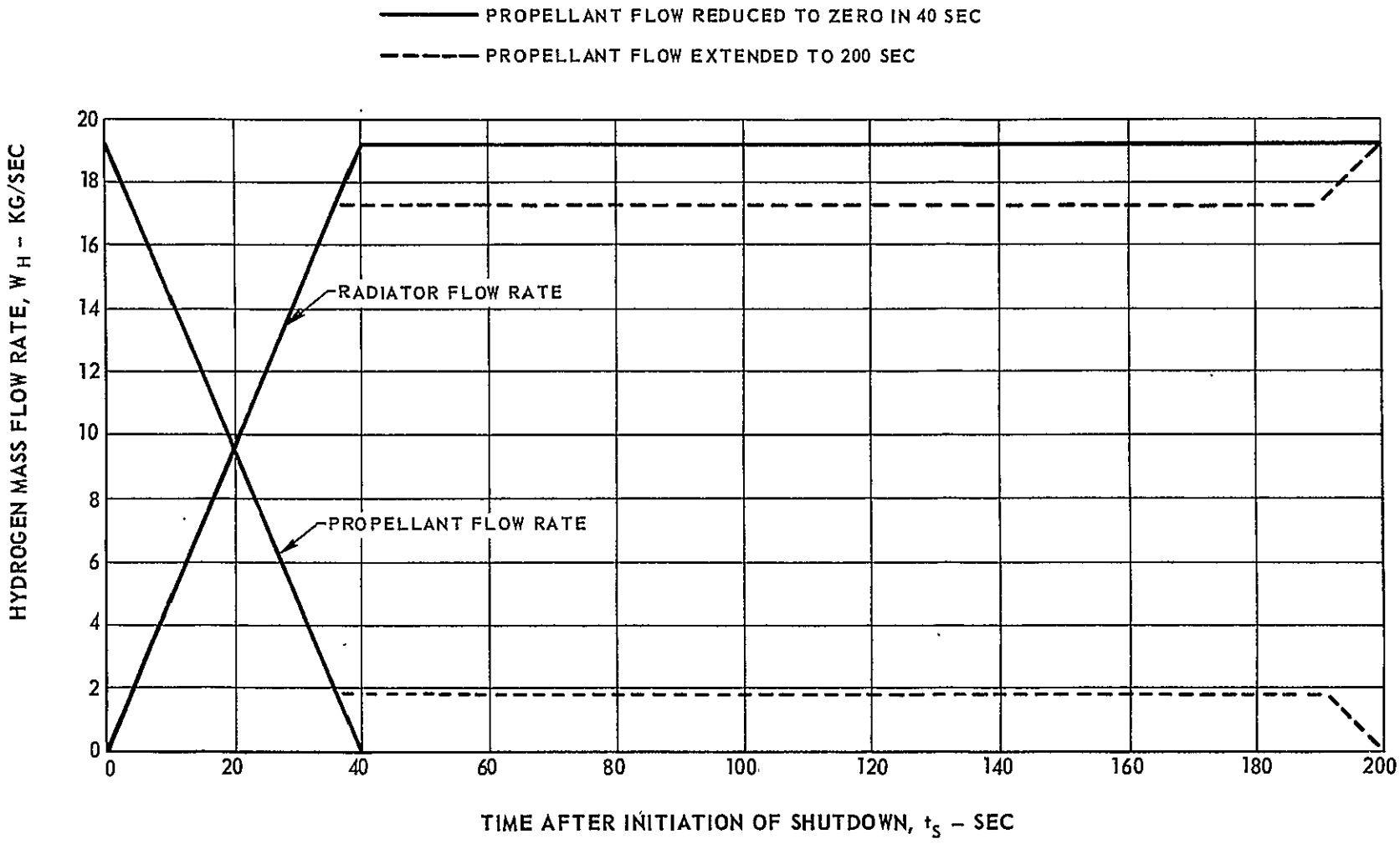

FIG. 114

POWER DEPOSITION IN FUEL AND NEON CIRCUIT DURING ENGINE SHUTDOWN

TIME TO ZERO FISSION POWER = 6 SEC

SEE FIG. 3 FOR REFERENCE ENGINE FLOW DIAGRAM

SEE FIG. 13 FOR AVERAGE FUEL TEMPERATURE

SEE FIG. 12 FOR SHUTDOWN POWER PROFILE

SEE FIG. 8 FOR FISSION PRODUCT AND INDUCED RADIOACTIVITY POWER

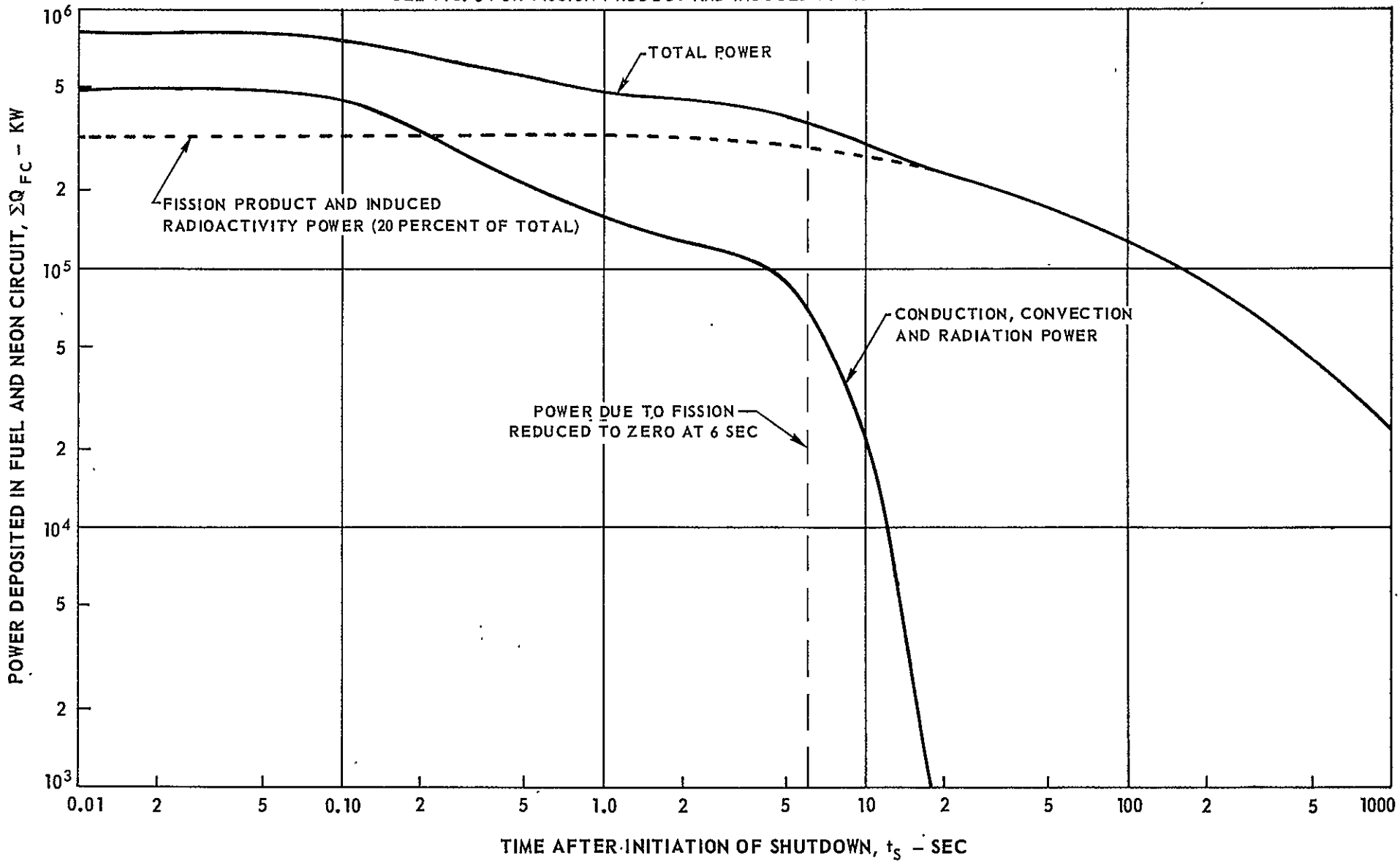

FIG. 15

POWER DEPOSITED IN SECONDARY HYDROGEN CIRCUIT DURING ENGINE SHUTDOWN

TIME TO ZERO FISSION POWER = 6 SEC

SEE FIG. 12 FOR SHUTDOWN POWER PROFILE

SEE FIG. 14 FOR FLOW SCHEDULES

SEE FIG. 3 FOR REFERENCE ENGINE FLOW DIAGRAM

SEE FIG. 8 FOR FISSION PRODUCT AND INDUCED RADIOACTIVITY POWER

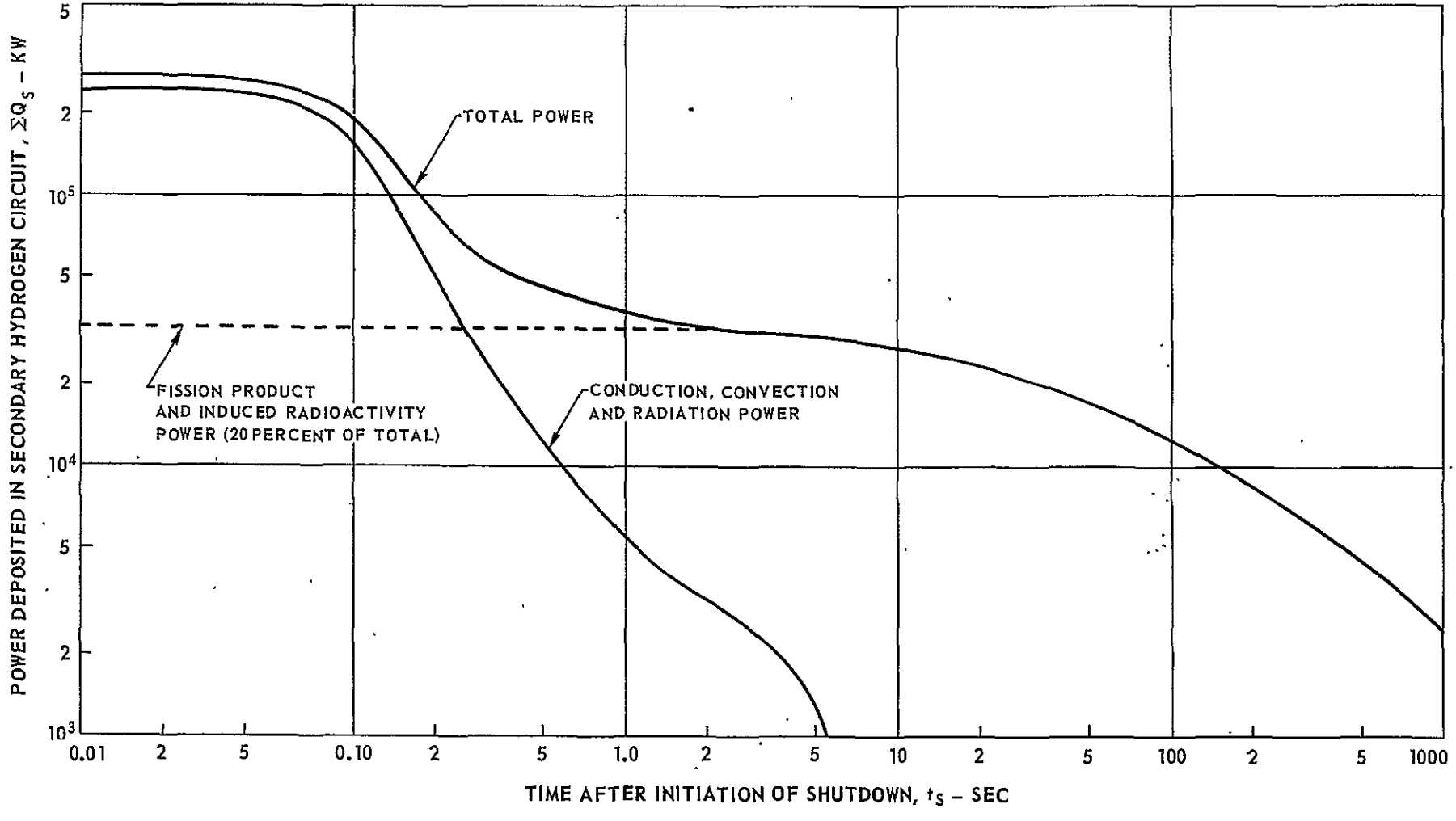

FIG. 16

TEMPERATURES IN BERYLLIUM OXIDE REGION DURING ENGINE SHUTDOWN

SEE FIG. 3 FOR REFERENCE ENGINE FLOW DIAGRAM

SEE FIG. 14 FOR FLOW SCHEDULES

SEE FIG. 12 FOR SHUTDOWN POWER PROFILE

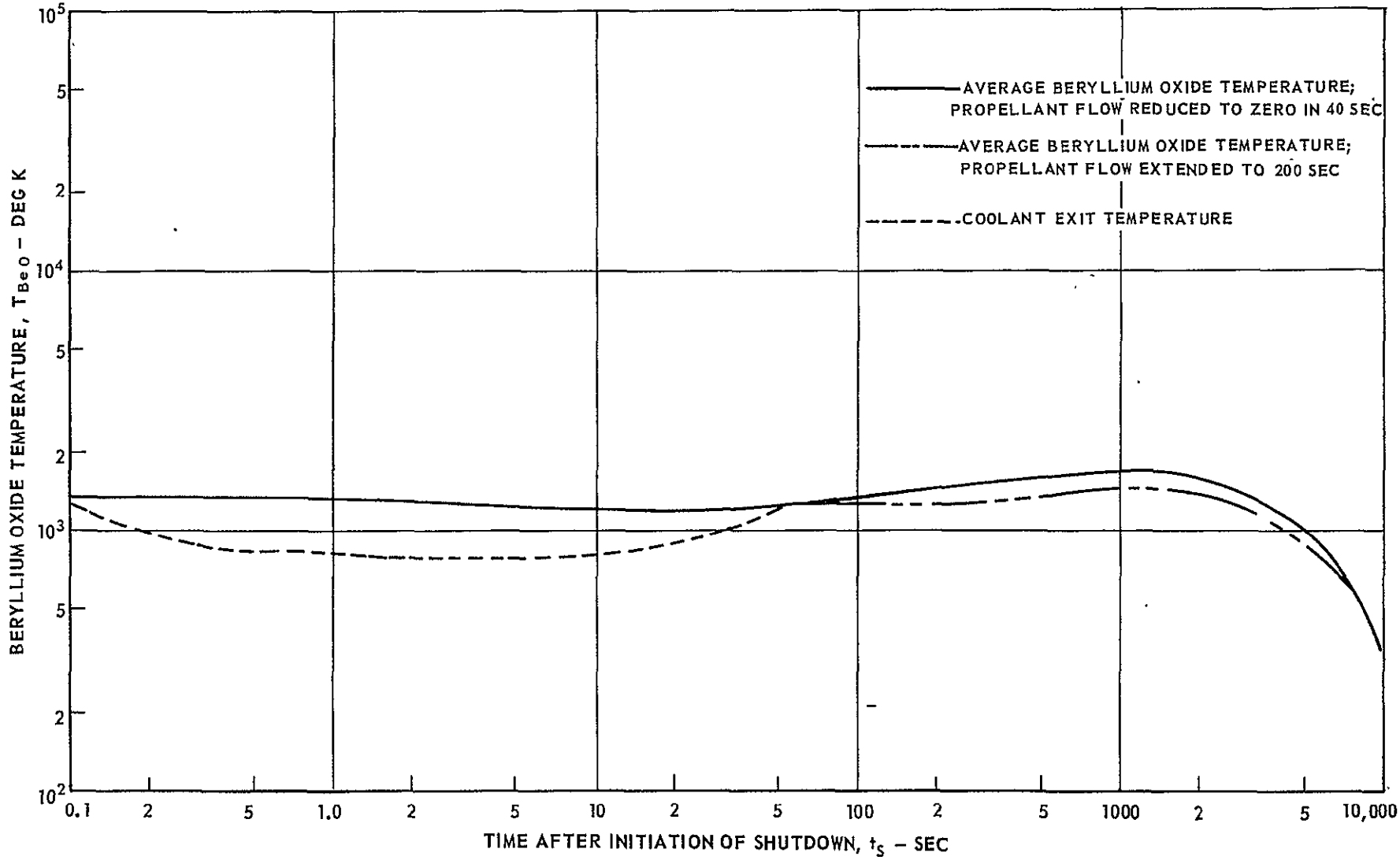

FIG. 17

TEMPERATURES IN GRAPHITE REGION DURING SHUTDOWN

SEE FIG. 3 FOR REFERENCE ENGINE FLOW DIAGRAM

SEE FIG. 14 FOR FLOW SCHEDULES

SEE FIG. 12 FOR SHUTDOWN POWER PROFILE

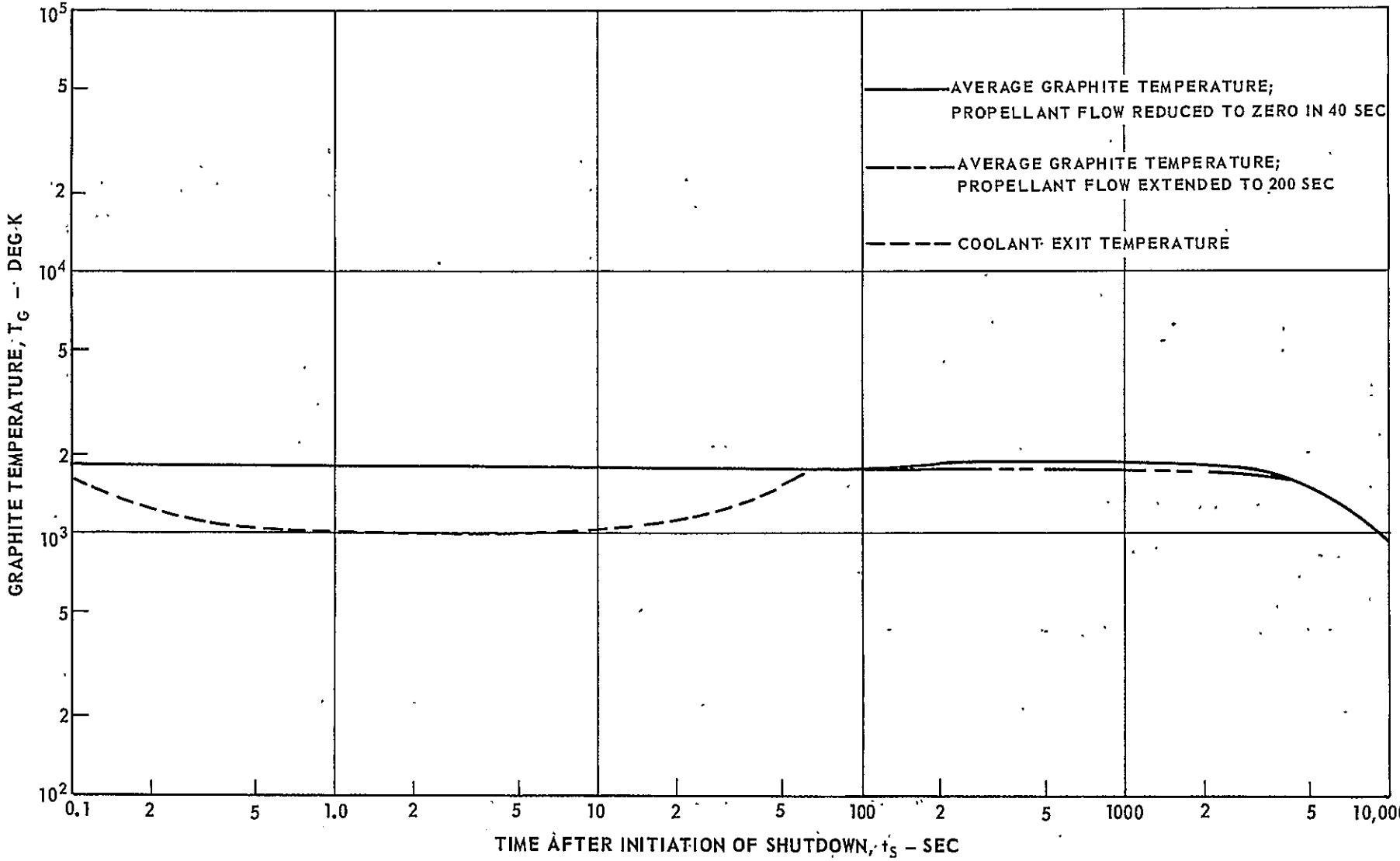

FIG. 18

ENGINE PRESSURE VARIATION DURING SHUTDOWN

SEE FIG. 14 FOR FLOW SCHEDULES

SEE FIG. 12 FOR SHUTDOWN POWER PROFILE

——— CAVITY PRESSURE WITH CONSTANT NOZZLE AREA (37.2 CM^2) ;
NOZZLES CLOSED AFTER $t_S \approx 200$ SEC, $P_T = 18$ ATM

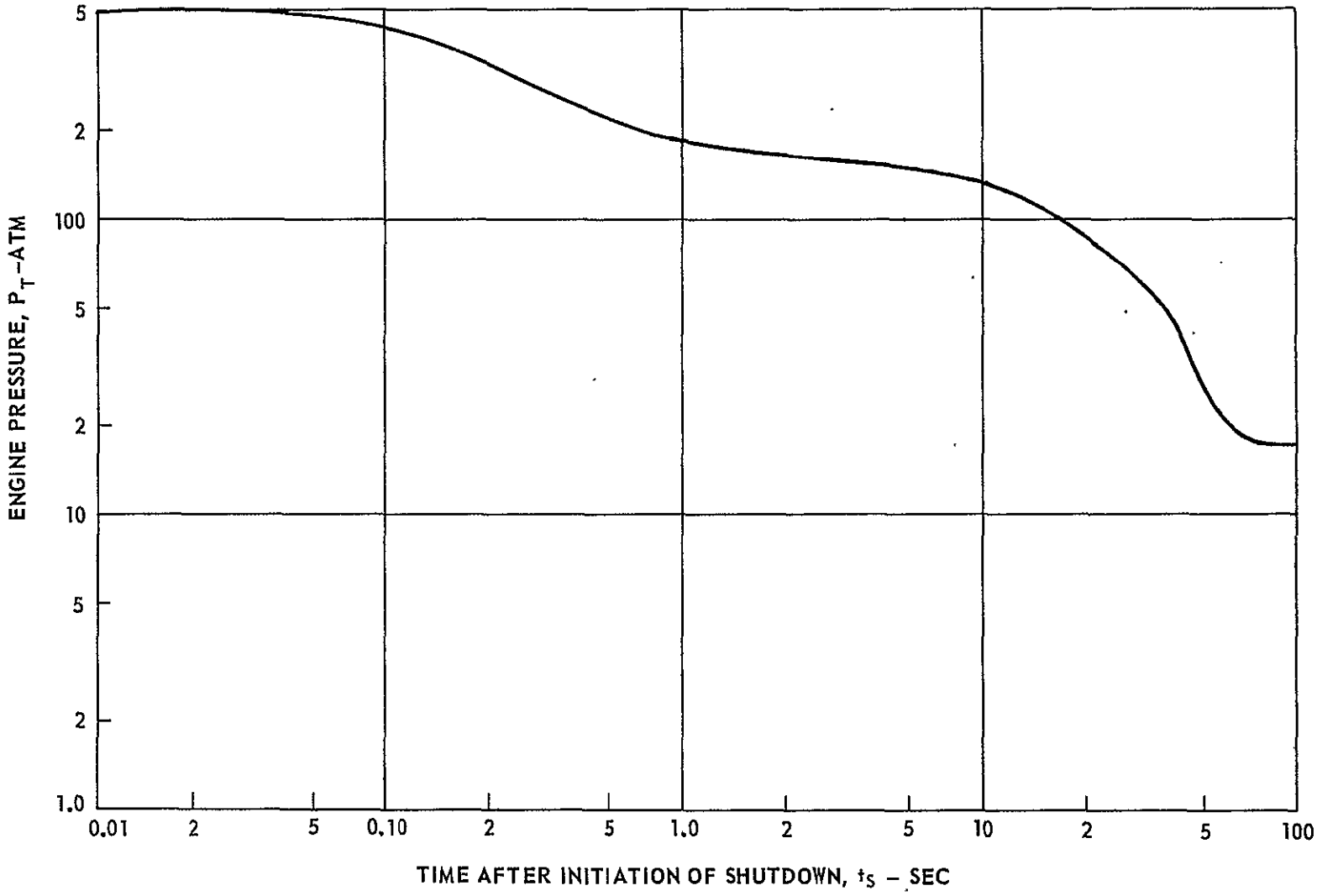

FIG. 19

FIG. 20

MODEL OF NUCLEAR LIGHT BULB ENGINE UNIT CAVITY USED IN FUEL AND BUFFER REGION RADIANT HEAT TRANSFER CALCULATIONS

(a) AXIAL CROSS-SECTION

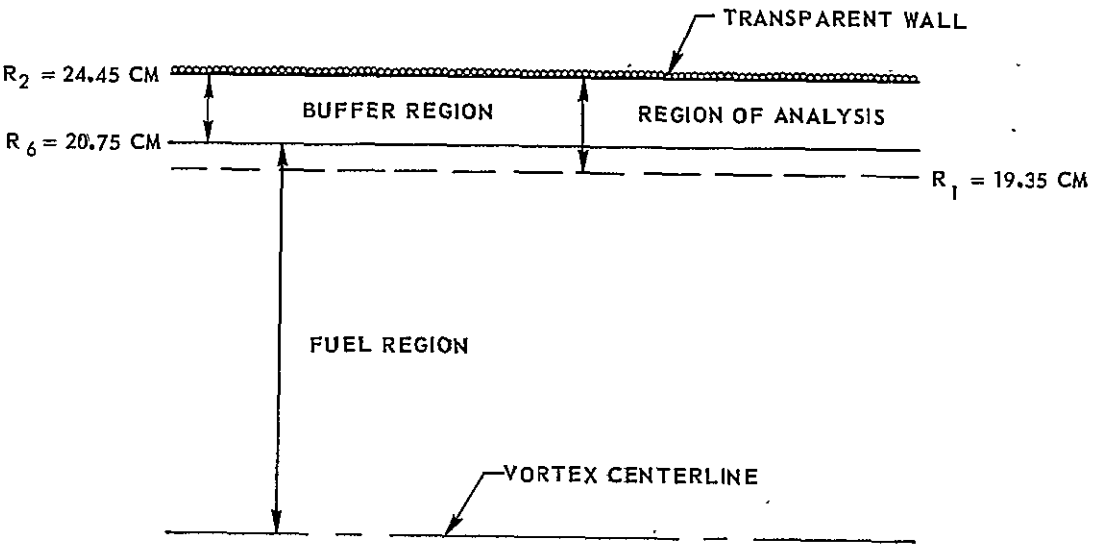

(b) CYLINDRICAL CROSS-SECTION

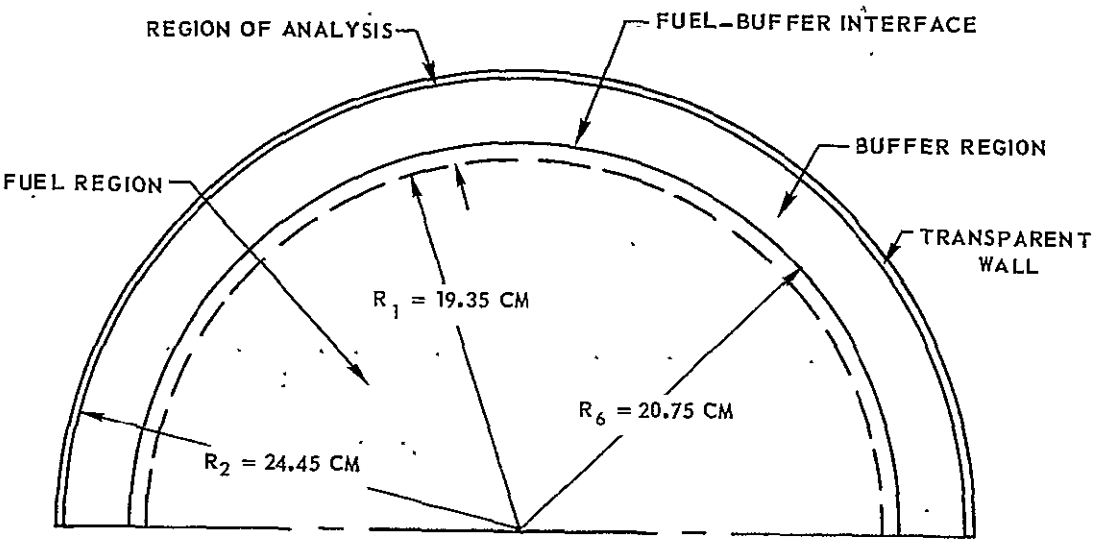

TYPICAL FUEL, SEED, AND NEON RADIAL PARTIAL PRESSURE DISTRIBUTIONS USED FOR RADIANT HEAT TRANSFER CALCULATIONS

$$P_T = P_F + P_N + P_S$$

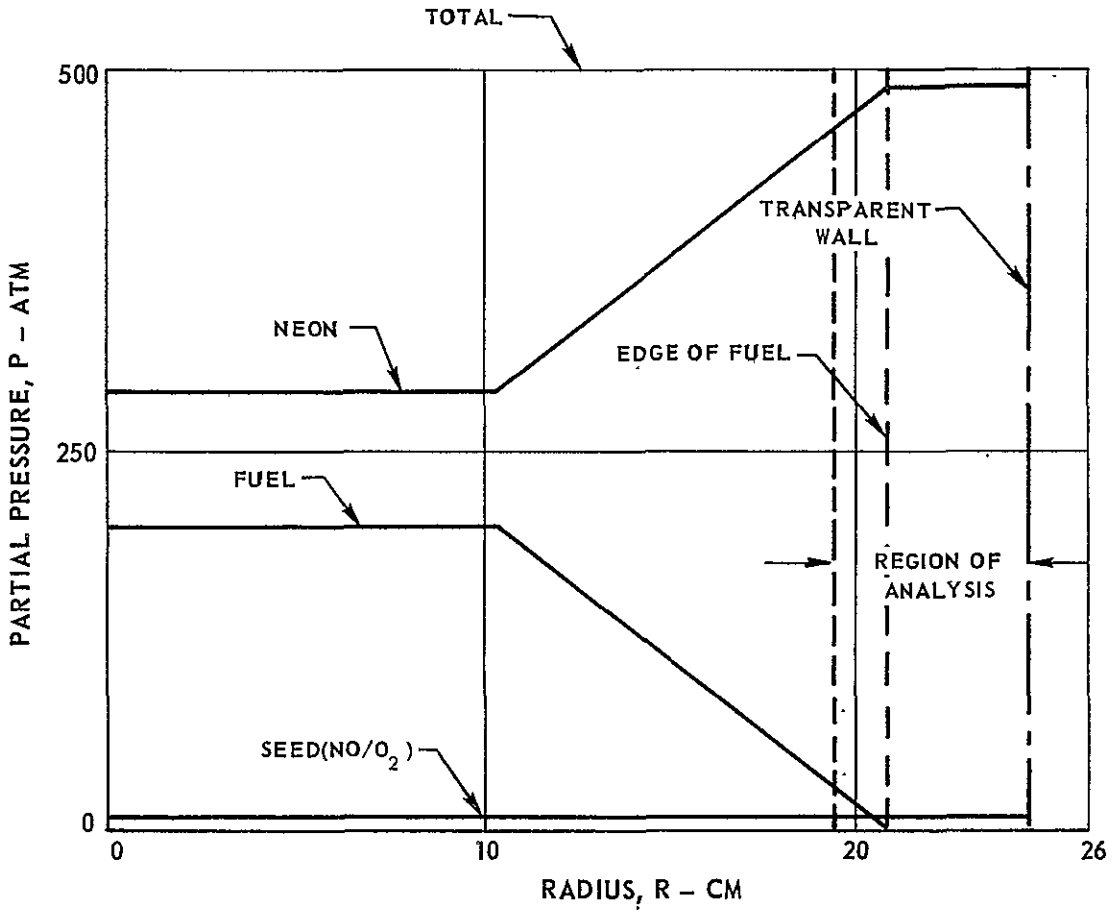

BUFFER-GAS FLOW PATTERN ASSUMED IN ANALYSIS OF CONVECTION AND TEMPERATURE DISTRIBUTIONS IN BUFFER REGION

SEE FIG. 20 FOR DIMENSIONS AND GEOMETRY OF REGION OF ANALYSIS

SEE FIG. 21 FOR FUEL, BUFFER GAS, AND SEED RADIAL PARTIAL PRESSURE DISTRIBUTIONS IN REGION OF ANALYSIS

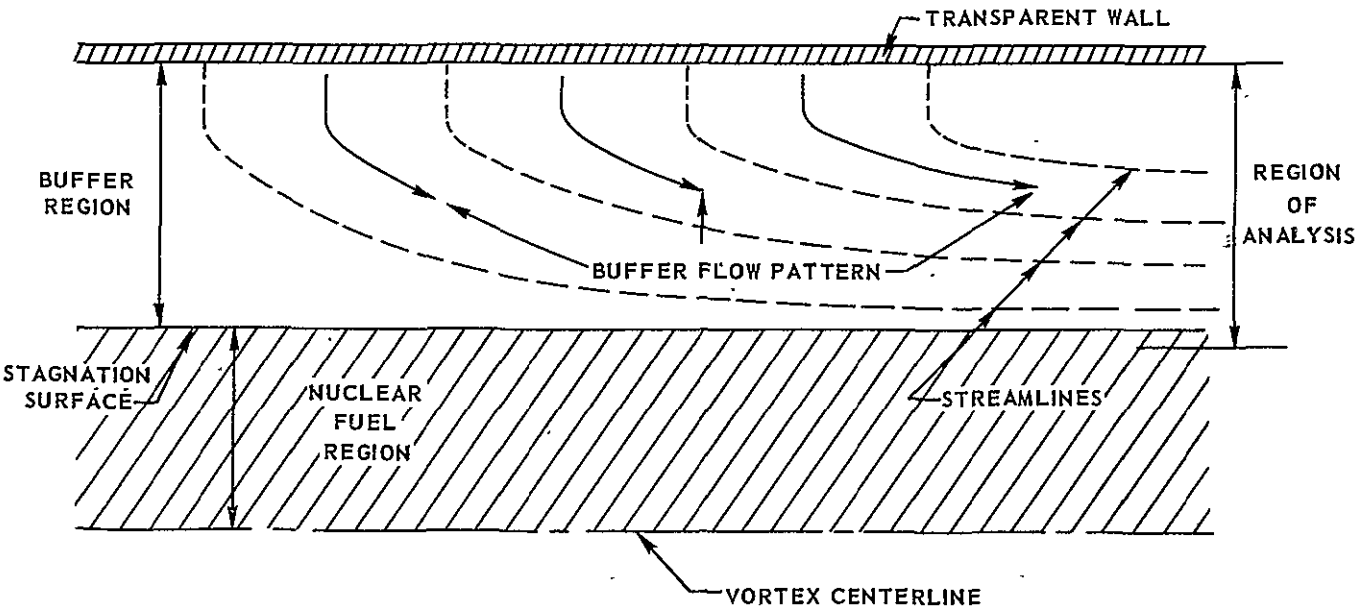

ILLUSTRATION OF CONVECTION REGION ITERATION TECHNIQUE

——— TEMPERATURE DISTRIBUTION, ITERATION 1
—— —— TEMPERATURE DISTRIBUTION, ITERATION 2
—— —— —— TEMPERATURE DISTRIBUTION, ITERATION 3

$$\begin{matrix}\text{ENERGY} \\ \text{ABSORBED}\end{matrix} - \begin{matrix}\text{ENERGY} \\ \text{CONVECTED}\end{matrix} - \begin{matrix}\text{ENERGY} \\ \text{RE-EMITTED}\end{matrix} \leqq |\epsilon|$$

$$\sum_j (a_\omega)_i^j \phi_i^j V_i \bar{E}^j - (W_{BR})_i (C_p)_i \Delta T_i - \sum_j S_i^j V_i \bar{E}^j \leqq |\epsilon|$$

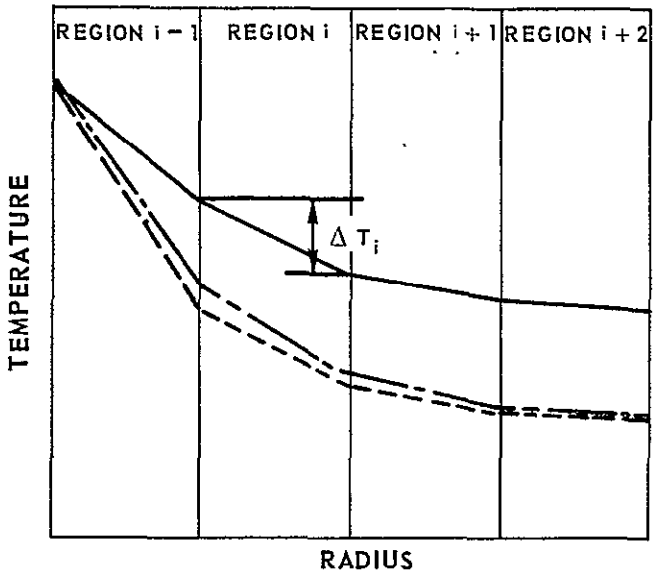

$(W_{BR})_i = \sum_{i=1}^{i} \rho_i (v_z)_i dA_i$, WHERE $(v_z)_i$ IS SET BY THE CONDITION THAT AXIAL DYNAMIC PRESSURE IS HELD CONSTANT IN BUFFER-GAS REGION,

$$\Delta P_z = \frac{\rho v_z^2}{2g} = \text{CONSTANT}$$

FIG. 24

FUEL REGION TEMPERATURE DISTRIBUTIONS FOR RANGE OF POWER LEVELS FROM 1 TO 100 TIMES REFERENCE ENGINE POWER LEVEL WITH UNSEEDED NEON BUFFER GAS

REFERENCE ENGINE POWER LEVEL, $Q_0 = 4600$ MEGW

REFERENCE ENGINE RADIATION HEAT FLUX, $q_o = 2.73 \times 10^{11}$ ERGS/CM^2-SEC AT EDGE OF FUEL

SEE FIG. 20 FOR GEOMETRY AND DIMENSIONS OF REGION OF ANALYSIS

SEE FIG. 21 FOR TYPICAL FUEL AND BUFFER GAS RADIAL PARTIAL PRESSURE DISTRIBUTIONS IN REGION OF ANALYSIS

TOTAL PRESSURES CORRESPONDING TO EACH POWER LEVEL TAKEN FROM FIG. 16 OF REF. 14 ASSUMING CONSTANT AVERAGE FUEL DENSITY IN FUEL REGION

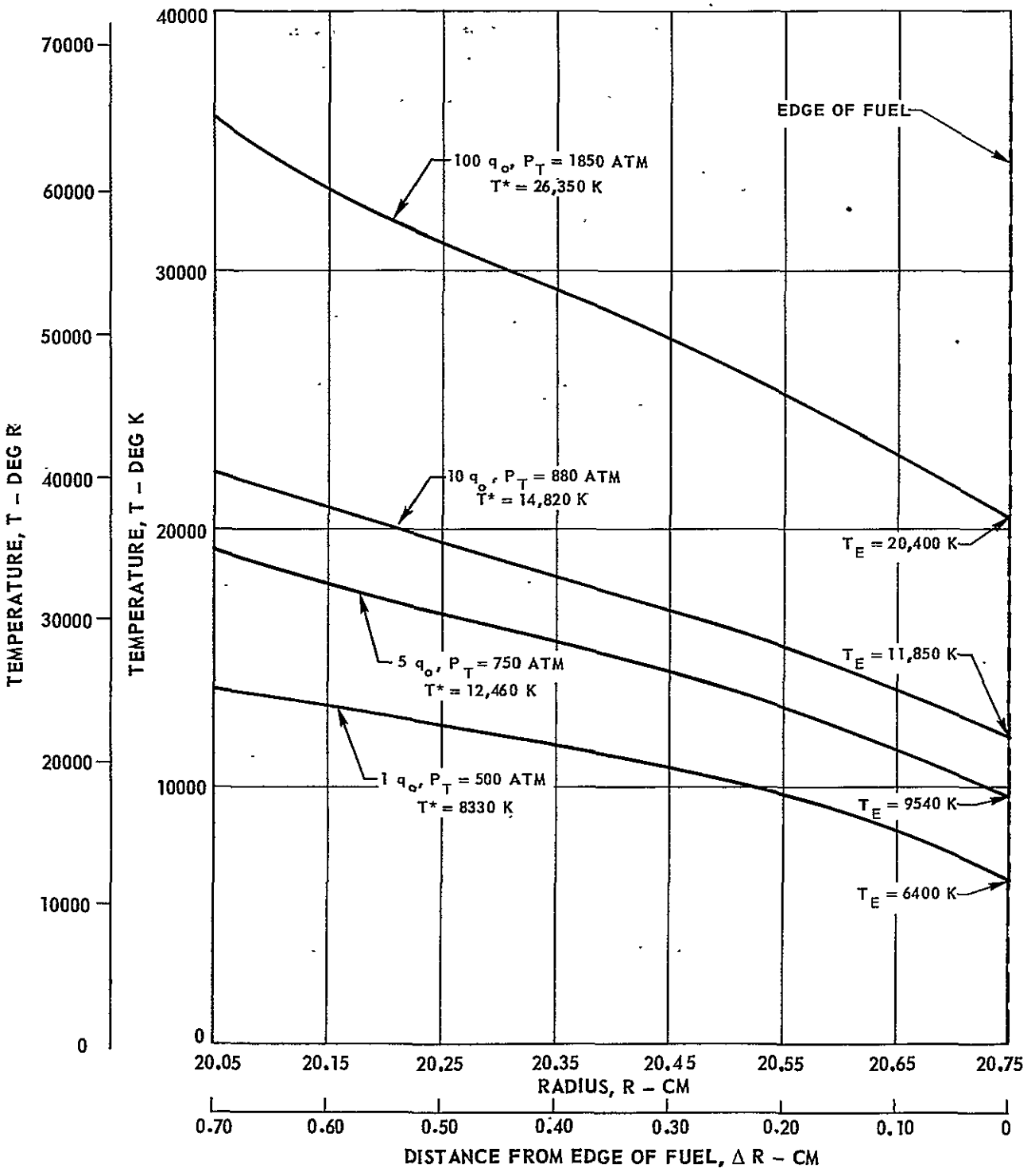

FIG. 25

SPECTRAL FLUX EMITTED FROM NUCLEAR FUEL FOR 1, 5, 10 AND 100 TIMES REFERENCE ENGINE RADIATION HEAT FLUX WITH UNSEEDED BUFFER GAS

REFERENCE ENGINE RADIATION HEAT FLUX AT EDGE OF FUEL, $q_o = 2.73 \times 10^{11}$ ERGS/CM^2 – SEC

SEE FIG. 24 FOR TEMPERATURE DISTRIBUTIONS IN EDGE-OF-FUEL REGION

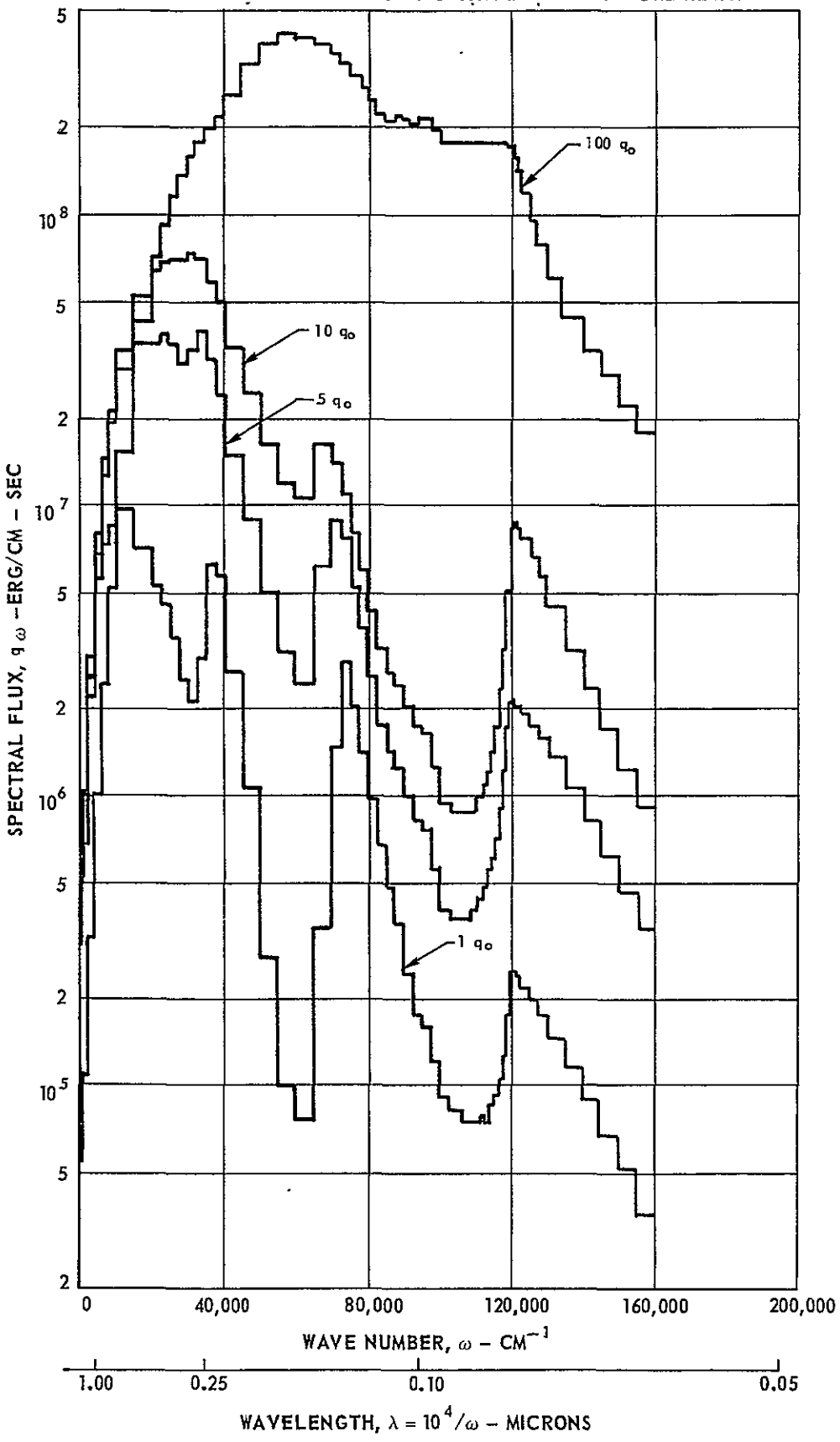

FIG. 26

FRACTIONAL HEAT FLUX DISTRIBUTIONS EMITTED FROM NUCLEAR FUEL FOR 1, 5, 10 AND 100 TIMES REFERENCE ENGINE RADIATION HEAT FLUX WITH UNSEEDED BUFFER GAS

REFERENCE ENGINE RADIATION HEAT FLUX AT EDGE OF FUEL, $q_o = 2.73 \times 10^{11}$ ERGS/CM^2 – SEC

SEE FIG. 24 FOR TEMPERATURE DISTRIBUTIONS IN EDGE-OF-FUEL REGION

SEE FIG. 25 FOR CORRESPONDING SPECTRAL HEAT FLUXES

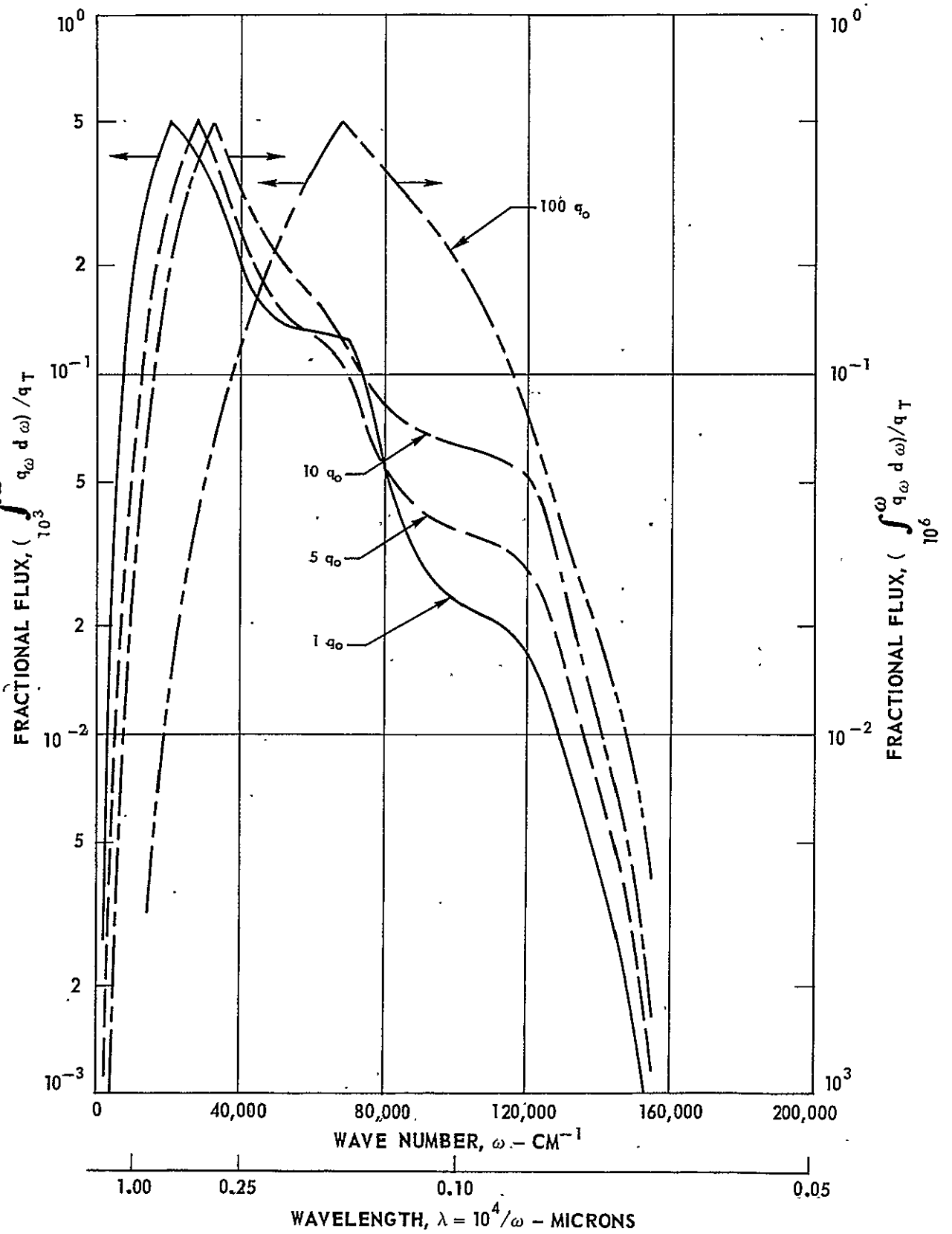

OPTICAL DEPTH DISTRIBUTIONS FOR DIFFERENT WAVE NUMBER INTERVALS FOR REFERENCE ENGINE RADIATION HEAT FLUX

$q_o = 2.73 \times 10^{11}$ ERGS/CM^2 – SEC

SEE FIG. 24 FOR TEMPERATURE DISTRIBUTION IN EDGE-OF-FUEL REGION

SEE FIG. 25 FOR CORRESPONDING SPECTRAL HEAT FLUX

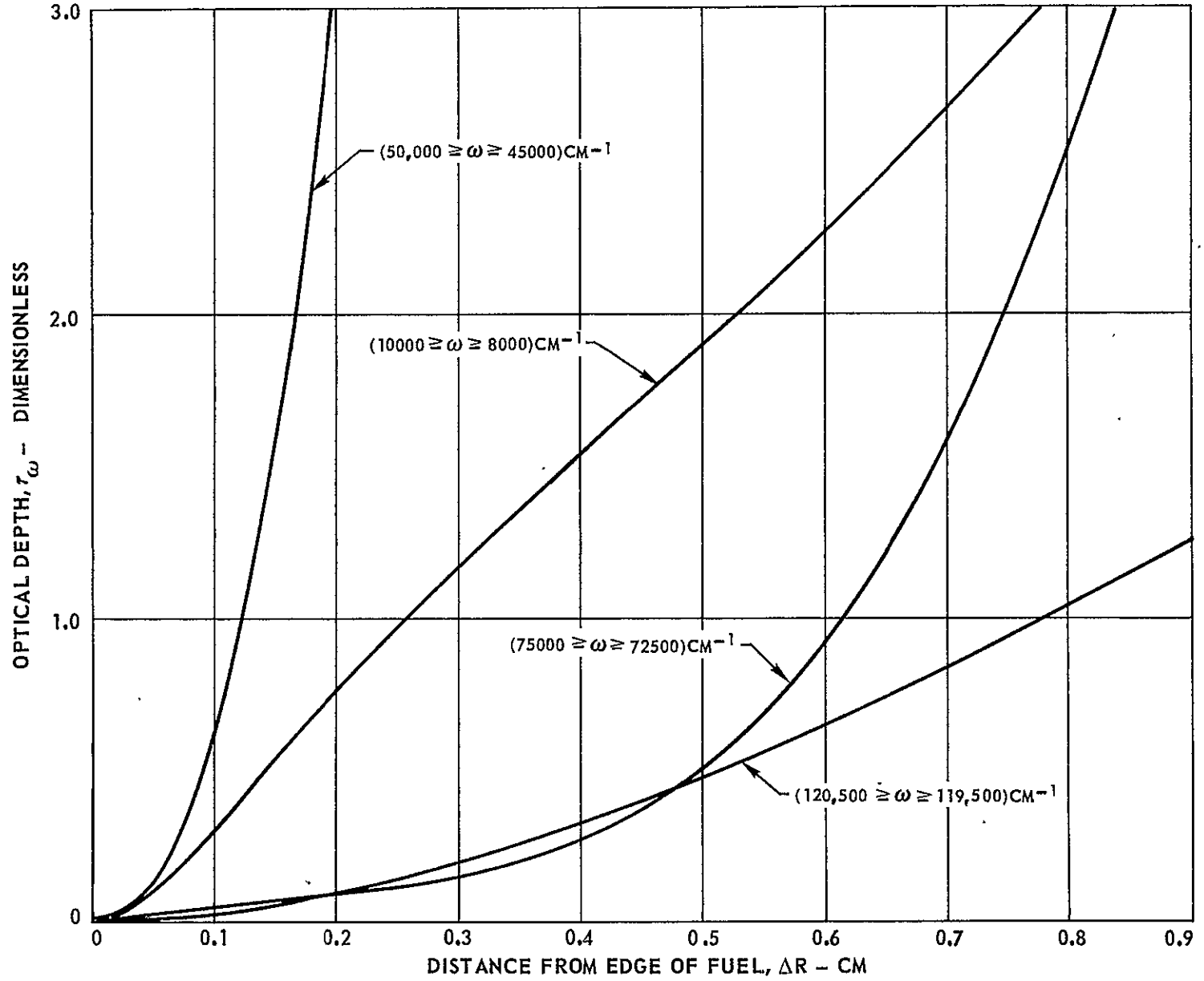

FIG. 27

OPTICAL DEPTH DISTRIBUTIONS FOR DIFFERENT WAVE NUMBER INTERVALS FOR 10 TIMES REFERENCE ENGINE RADIATION HEAT FLUX

$10\ q_o = 2.73 \times 10^{12}$ ERGS/CM^2 – SEC

SEE FIG. 24 FOR TEMPERATURE DISTRIBUTION IN EDGE-OF-FUEL REGION

SEE FIG. 25 FOR CORRESPONDING SPECTRAL HEAT FLUX

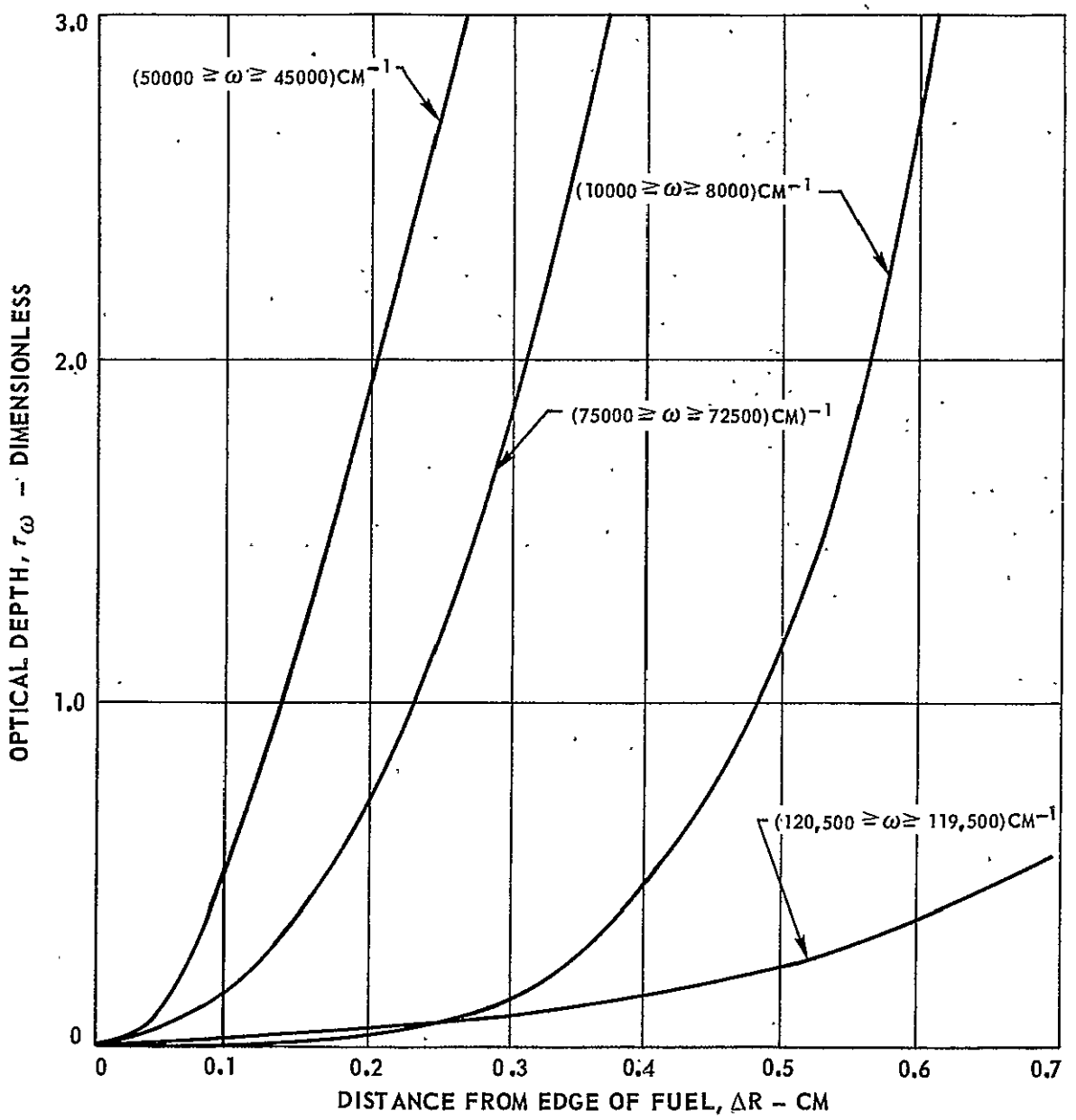

VARIATION OF EFFECTIVE SPECTRAL BLACK BODY RADIATING TEMPERATURE WITH WAVE NUMBER FOR 1, 5 AND 10 TIMES REFERENCE ENGINE HEAT FLUX

REFERENCE ENGINE RADIATION HEAT FLUX, $q_o = 2.73 \times 10^{11}$ ERGS/CM^2 – SEC

SEE FIG. 24 FOR TEMPERATURE DISTRIBUTIONS IN EDGE-OF-FUEL REGION

SEE FIG. 25 FOR CORRESPONDING SPECTRAL HEAT FLUXES

T_ω^{bb} DEFINED AS THAT TEMPERATURE FOR WHICH $q_\omega^{bb} = q_\omega^{n\, q_o}$ AT EDGE OF FUEL

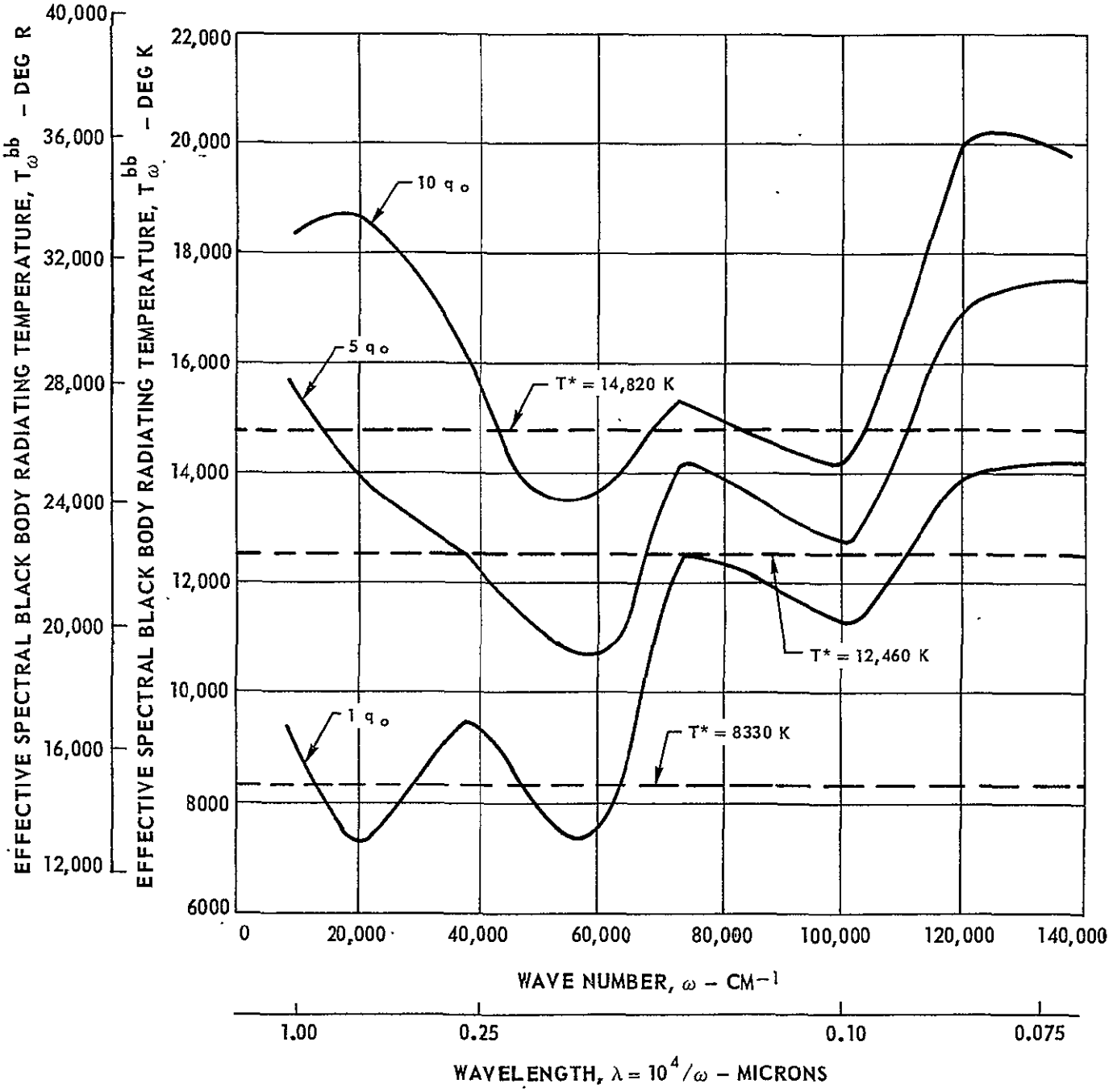

FRACTION OF RADIATED ENERGY IN UV AT TRANSPARENT WALL FOR POWER LEVELS FROM 1 TO 100 TIMES REFERENCE ENGINE POWER LEVEL WITH UNSEEDED NEON BUFFER GAS

TRANSPARENT WALL THICKNESS = 0.0127 CM (0.005 IN.)

REFERENCE ENGINE POWER LEVEL, Q_0 = 4600 MEGW

FOR BeO, $\lambda_{CUTOFF} = 0.125$ MICRONS

FOR SiO_2, $\lambda_{CUTOFF} = 0.180$ MICRONS

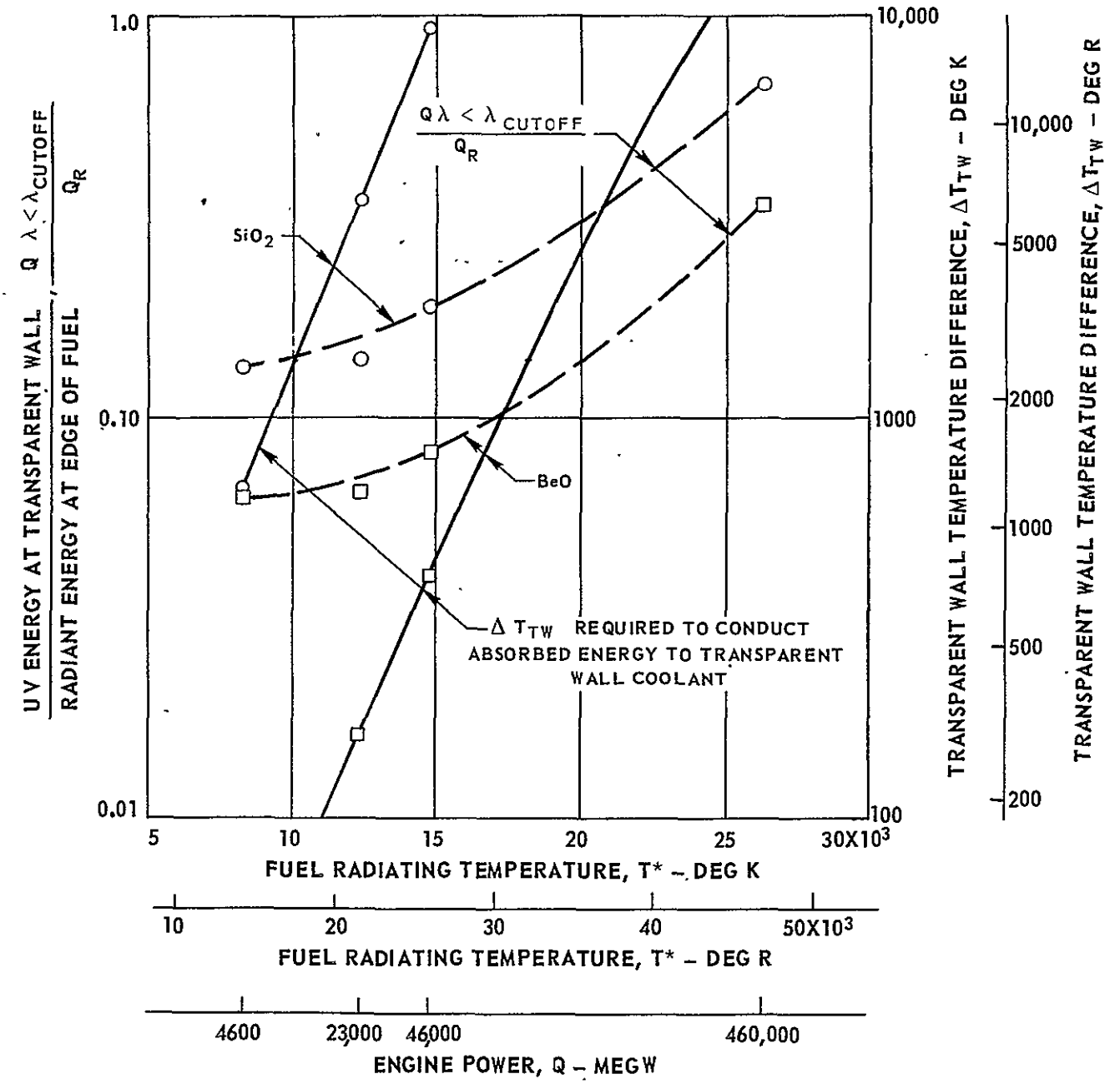

FIG. 31

BUFFER REGION TEMPERATURE DISTRIBUTIONS FOR REFERENCE ENGINE POWER LEVEL FOR VARIOUS NO/O_2 SEED PRESSURES

REFERENCE ENGINE POWER LEVEL, $Q_o = 4600$ MEGW

REFERENCE ENGINE RADIATION HEAT FLUX AT EDGE OF FUEL, $q_o = 2.73 \times 10^{11}$ ERGS/CM^2 – SEC

FUEL REGION TEMPERATURE DISTRIBUTION SHOWN IN FIG. 24 USED FOR ALL CASES WITH NO/O_2 SEED

SEE FIG. 20 FOR GEOMETRY AND DIMENSIONS OF REGION OF ANALYSIS

SEE FIG. 21 FOR FUEL, SEED, AND NEON RADIAL PARTIAL PRESSURE DISTRIBUTIONS IN REGION OF ANALYSIS

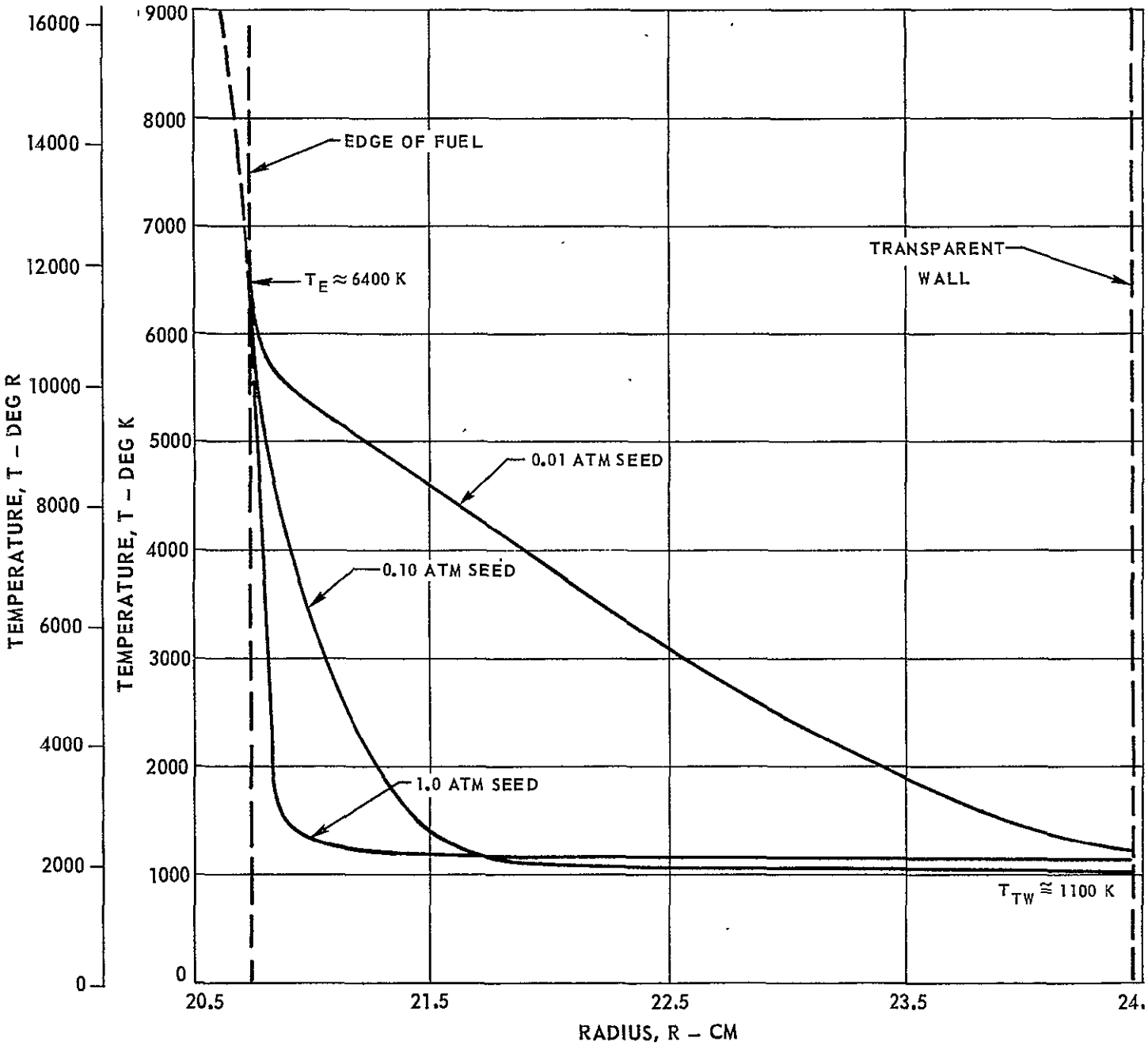

SPECTRAL FLUX EMITTED FROM NUCLEAR FUEL REGION FOR REFERENCE ENGINE WITH 0.01, 0.10, 1.0 ATM OF NO/O_2 SEED IN FUEL AND BUFFER-GAS REGIONS

SEE FIG. 20 FOR GEOMETRY AND DIMENSIONS OF REGION OF ANALYSIS

SEE FIG. 21 FOR FUEL, SEED, AND NEON RADIAL PARTIAL PRESSURE DISTRIBUTIONS IN REGION OF ANALYSIS

SEE FIGS. 24 AND 31 FOR TEMPERATURE DISTRIBUTIONS IN REGION OF ANALYSIS

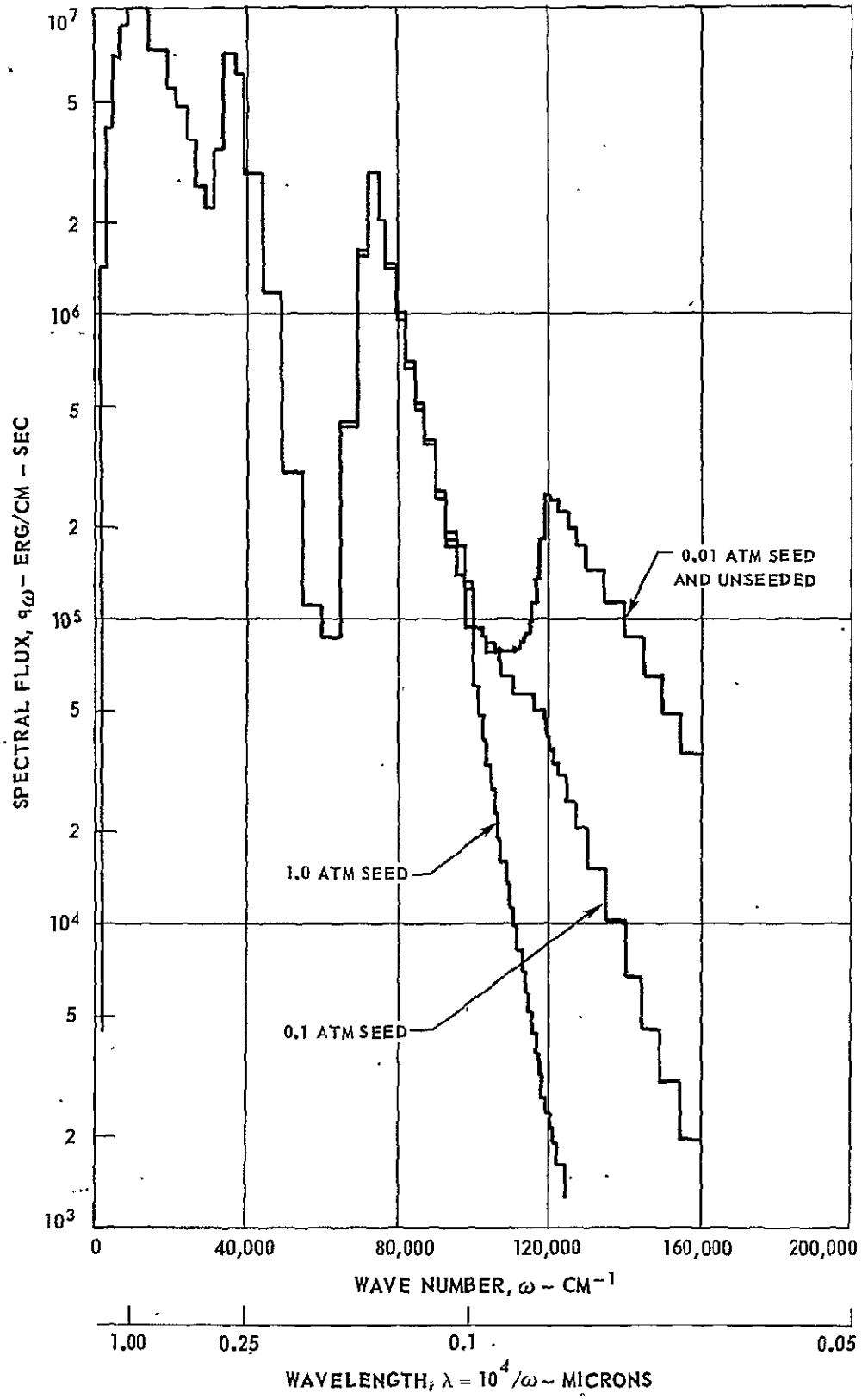

FIG. 33

FRACTIONAL HEAT FLUX DISTRIBUTIONS EMITTED FROM NUCLEAR FUEL REGION OF REFERENCE ENGINE WITH 0.01, 0.10, 1.0 ATM OF NO/O_2 SEED IN FUEL AND BUFFER-GAS REGION

SEE FIG. 32 FOR CORRESPONDING SPECTRAL FLUXES

SEE TABLE VI FOR FRACTIONAL FLUXES IN WAVE NUMBER RANGES BELOW UV CUTOFFS FOR BeO AND SiO_2 TRANSPARENT WALLS FOR 0.01, 0.10, 1.0, 10 AND 200 ATM OF NO/O_2 SEED

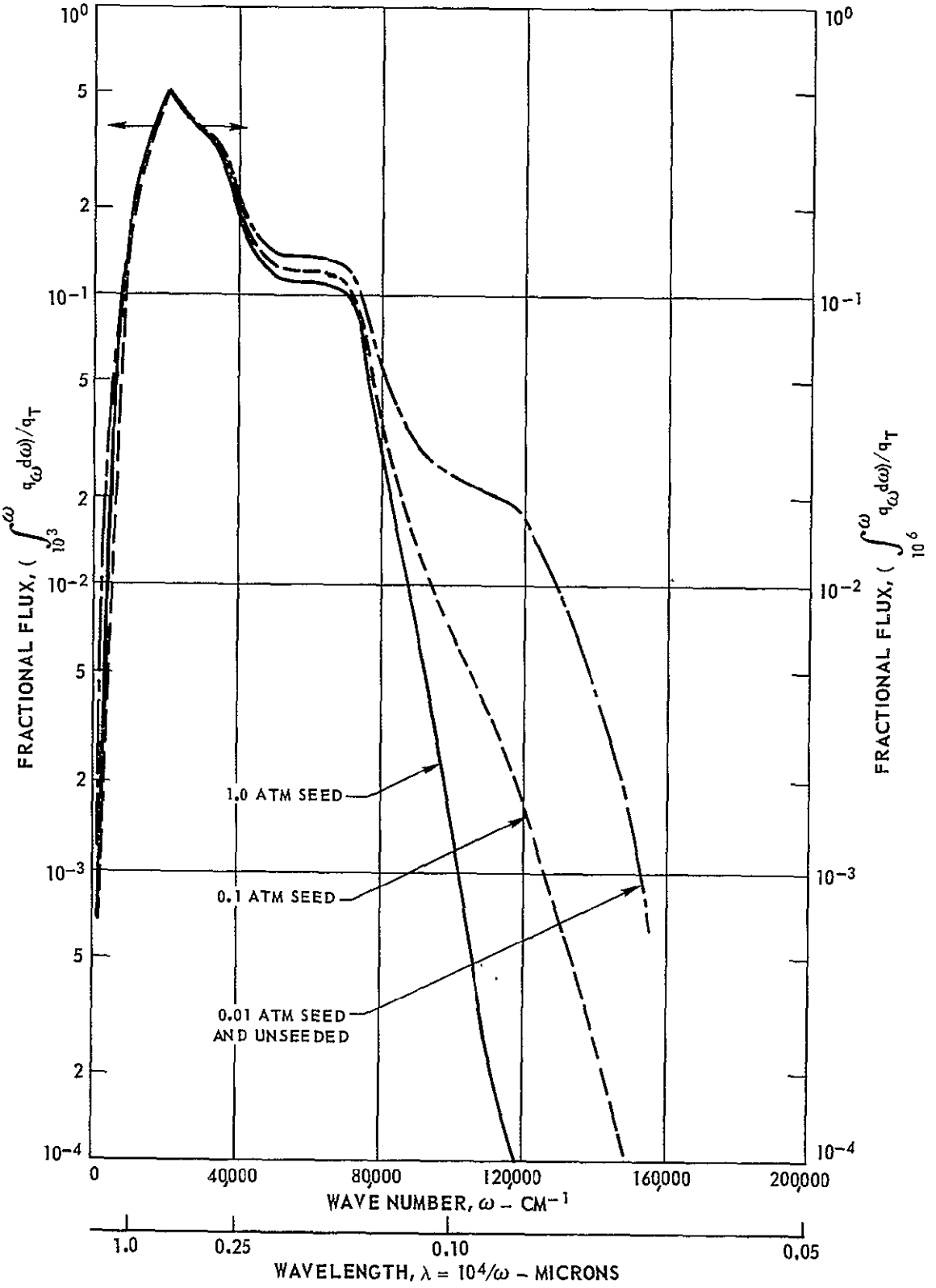

OPTICAL DEPTH DISTRIBUTIONS OF FUEL REGION FOR WAVE NUMBER INTERVAL 120,500 TO 119,500 CM^{-1} AT VARIOUS NO/O_2 SEED PRESSURES FOR REFERENCE ENGINE RADIATION HEAT FLUX

$q_o = 2.73 \times 10^{11}$ ERGS/CM^2 – SEC

SEE FIGS. 24 AND 31 FOR TEMPERATURE DISTRIBUTIONS IN REGION OF ANALYSIS

SEE FIG. 32 FOR CORRESPONDING SPECTRAL HEAT FLUXES

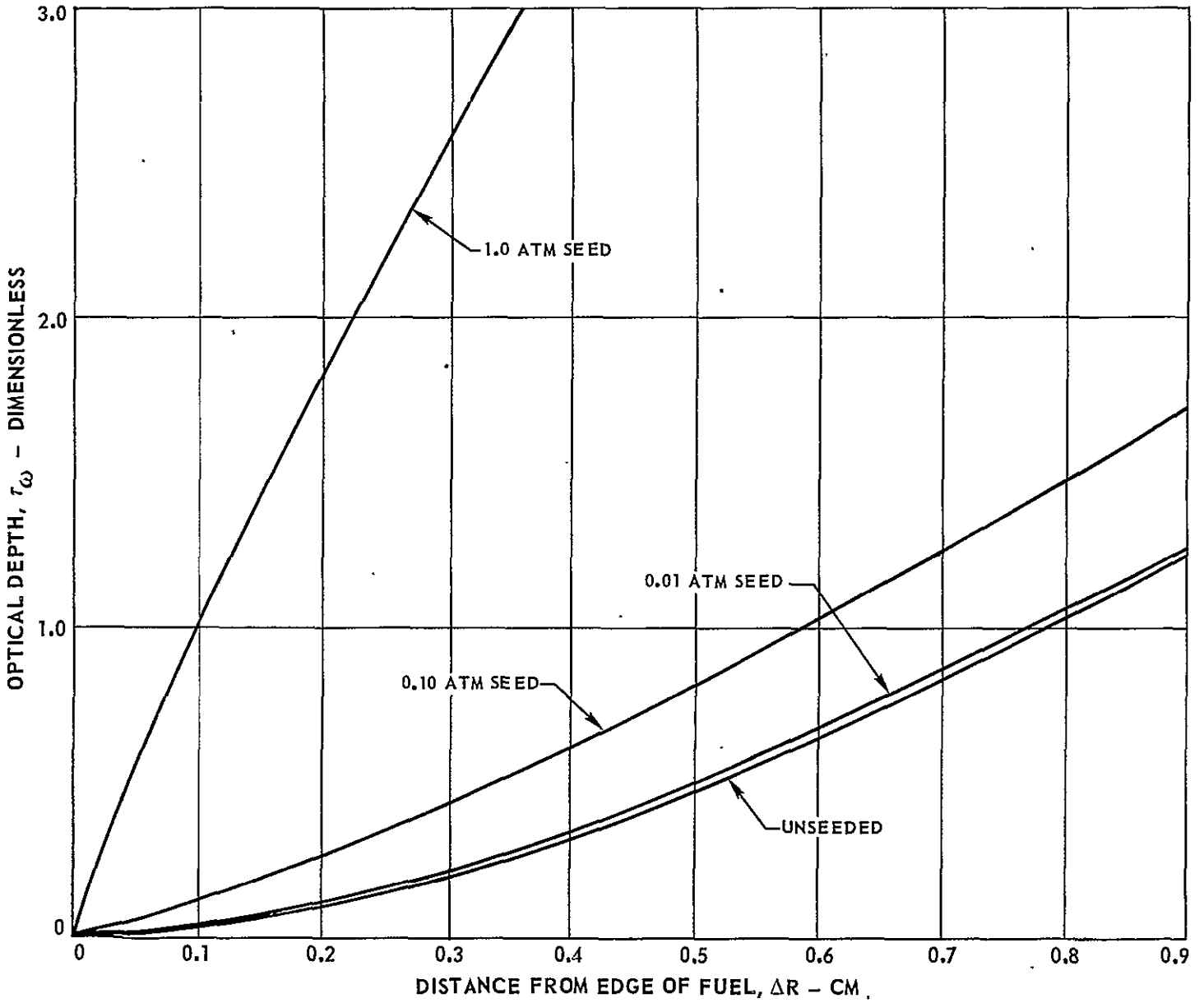

OPTICAL DEPTH DISTRIBUTIONS OF FUEL REGION FOR WAVE NUMBER INTERVAL 75,000 TO 72,500 CM^{-1} AT VARIOUS NO/O_2 SEED PRESSURES FOR REFERENCE ENGINE RADIATION HEAT FLUX

$q_\sigma = 2.73 \times 10^{11}$ ERGS/CM^2 - SEC

SEE FIGS. 24 AND 31 FOR TEMPERATURE DISTRIBUTIONS IN REGION OF ANALYSIS

SEE FIG. 32 FOR CORRESPONDING SPECTRAL HEAT FLUXES

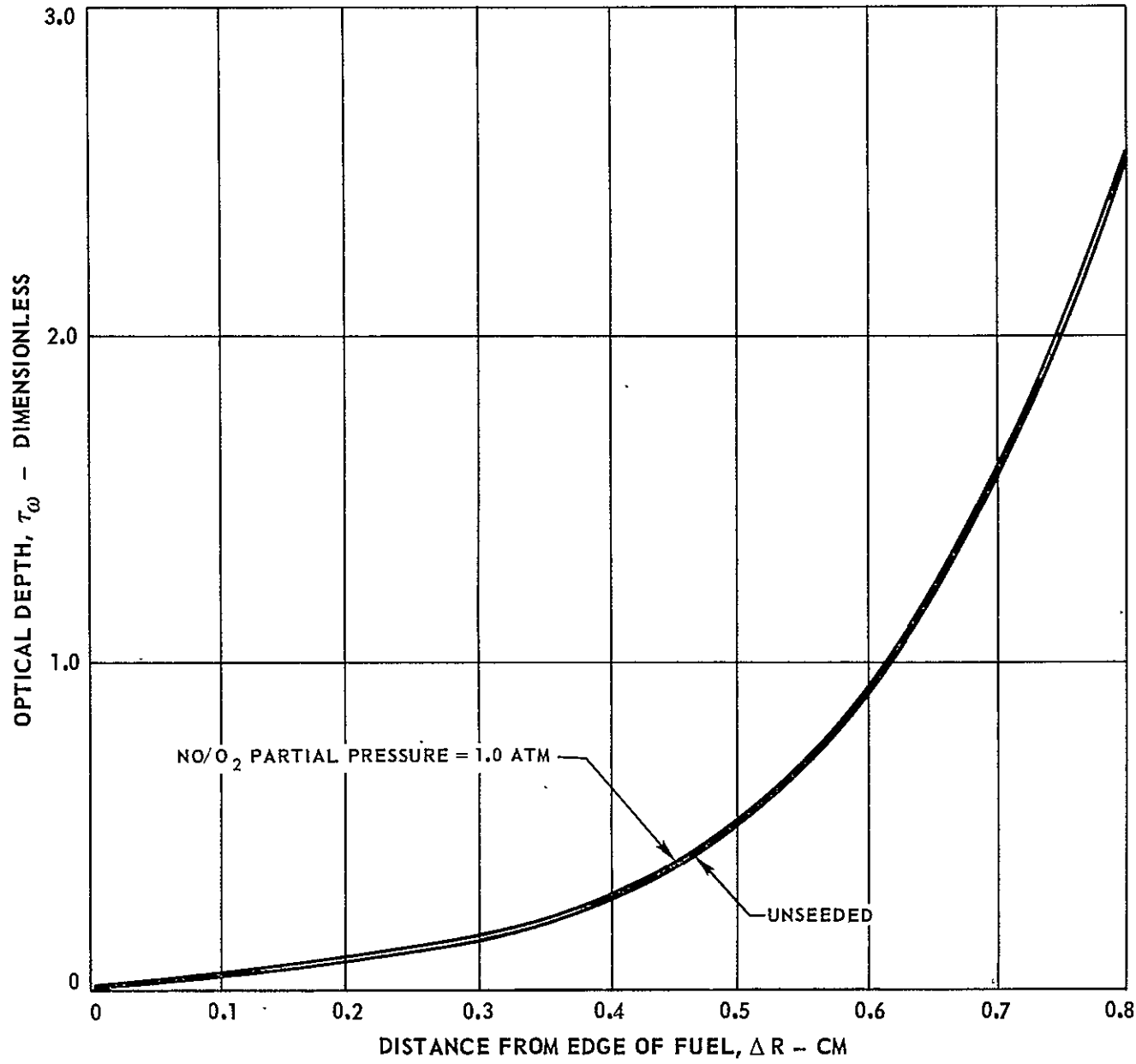

FIG. 36

OPTICAL DEPTH DISTRIBUTIONS OF FUEL REGION FOR WAVE NUMBER INTERVAL 32,500 – 30,000 CM^{-1} AT VARIOUS NO/O_2 SEED PRESSURES FOR REFERENCE ENGINE RADIATION HEAT FLUX

$q_o = 2.73 \times 10^{11}$ ERGS/CM^2 – SEC

SEE FIGS. 24 AND 31 FOR TEMPERATURE DISTRIBUTIONS IN REGION OF ANALYSIS

SEE FIG. 32 FOR CORRESPONDING SPECTRAL HEAT FLUX

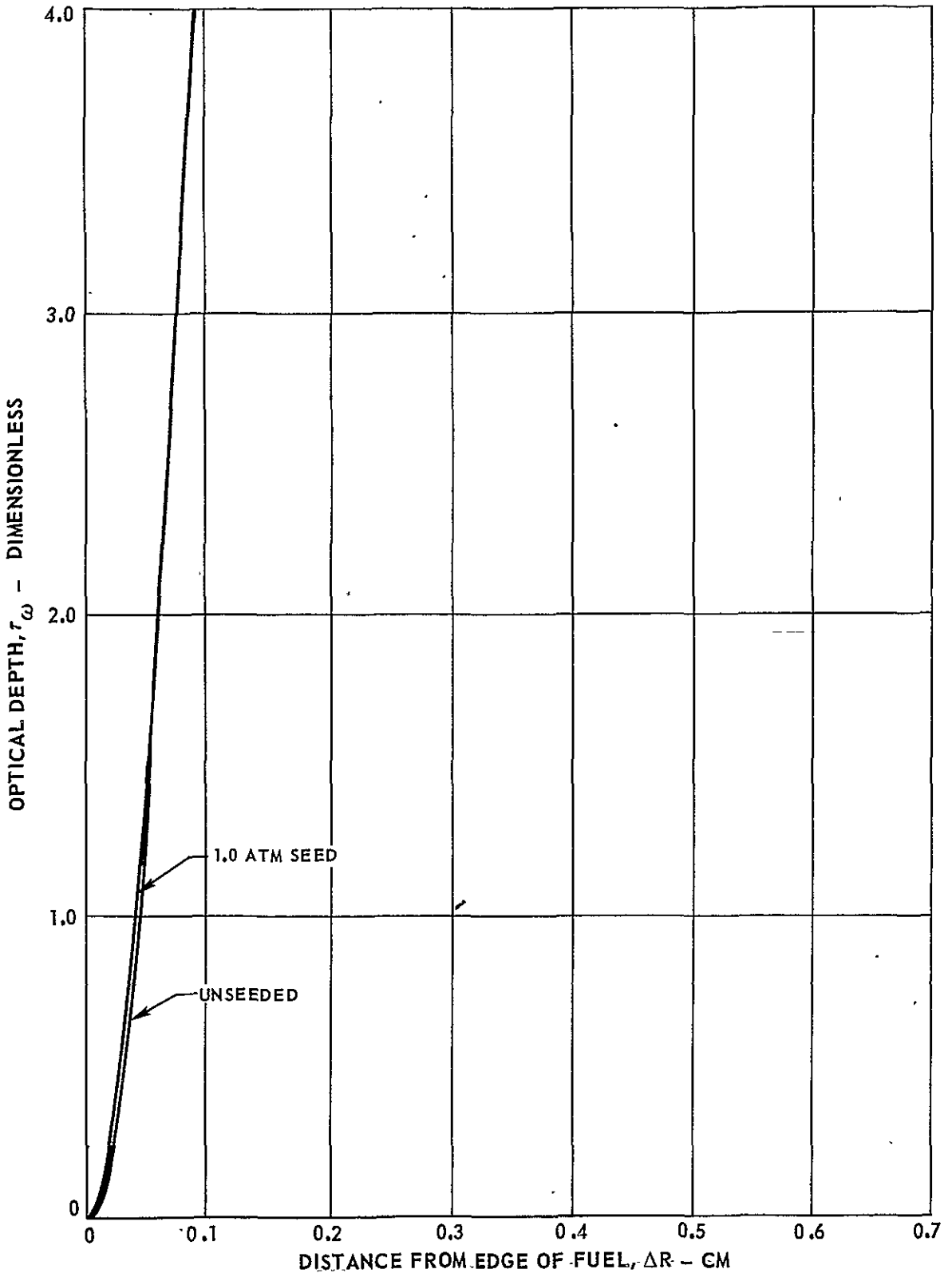

FIG. 37

VARIATION OF EFFECTIVE SPECTRAL BLACK BODY RADIATING TEMPERATURE WITH WAVE NUMBER FOR REFERENCE ENGINE SEEDED WITH 0.01, 0.10 AND 1.0 ATM OF NO/O_2

REFERENCE ENGINE RADIATION HEAT FLUX, $q_o = 2.73 \times 10^{11}$ ERGS/CM^2 – SEC

SEE FIGS. 24 AND 31 FOR TEMPERATURE DISTRIBUTIONS IN REGION OF ANALYSIS

SEE FIG. 32 FOR CORRESPONDING SPECTRAL HEAT FLUXES

T_ω^{bb} DEFINED AS THAT TEMPERATURE FOR WHICH $q_\omega^{bb} = q_\omega^{SEED}$ AT EDGE OF FUEL

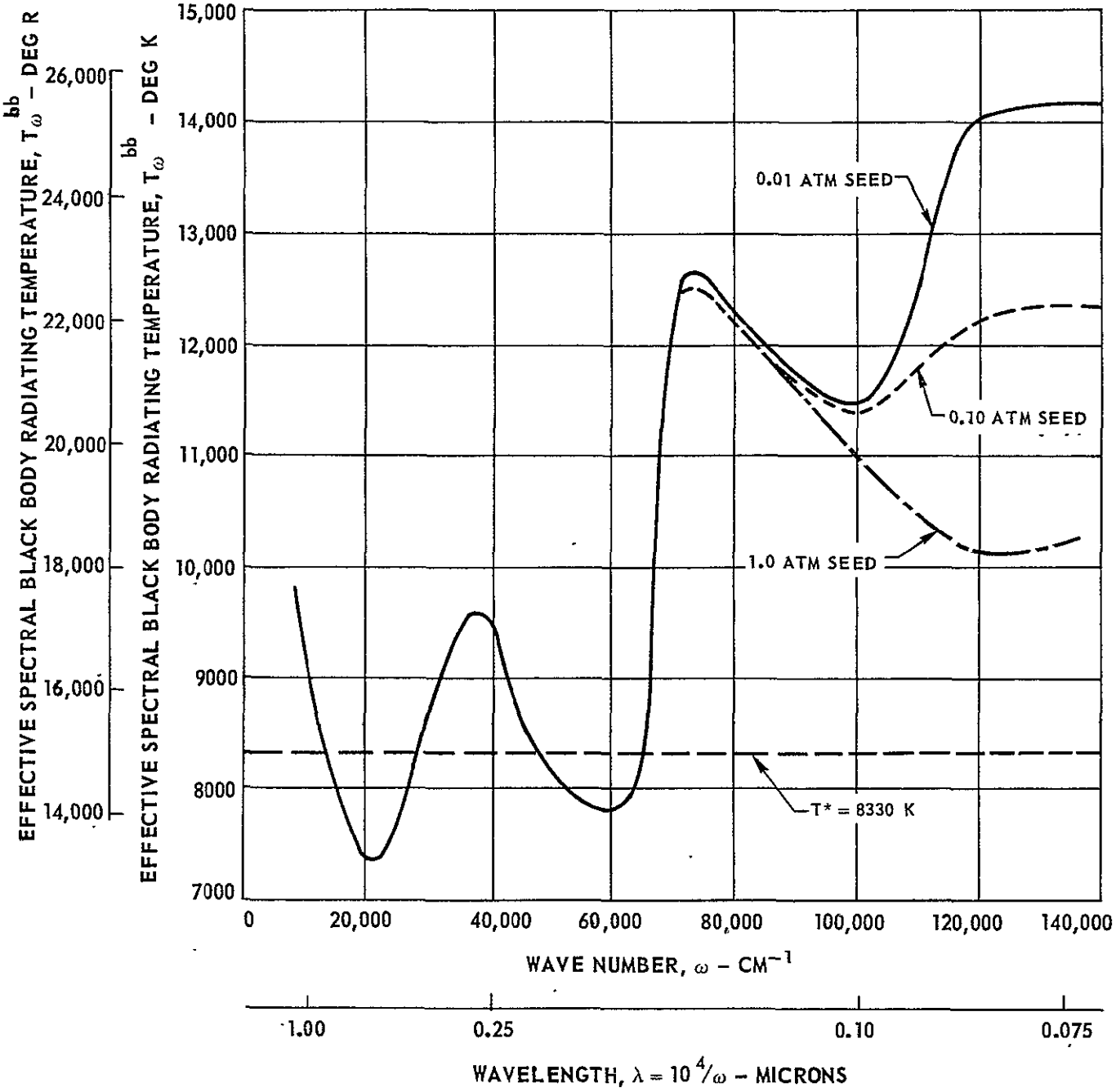

FRACTIONAL ATTENUATION OF UV ENERGY BY NO/O_2 SEEDING OF NEON BUFFER GAS FOR REFERENCE ENGINE RADIATION HEAT FLUX

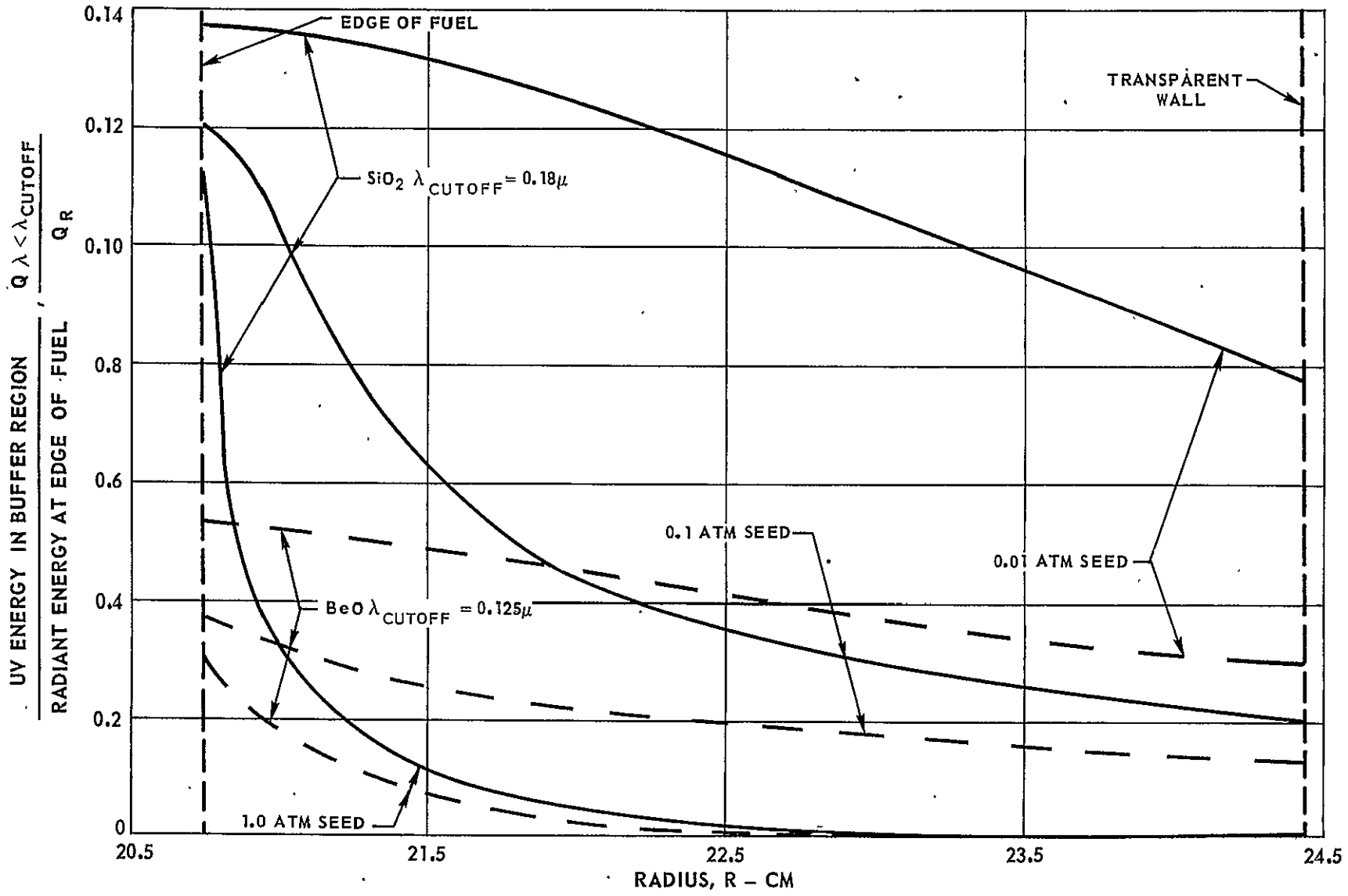

FIG. 38

RADIAL WEIGHT FLOW, CONVECTED ENERGY AND AXIAL VELOCITY DISTRIBUTIONS IN BUFFER REGION FOR REFERENCE ENGINE SEEDED WITH 0.01 ATM NO/O_2

AXIAL PRESSURE DROP, $\Delta P_Z = 0.025$ ATM

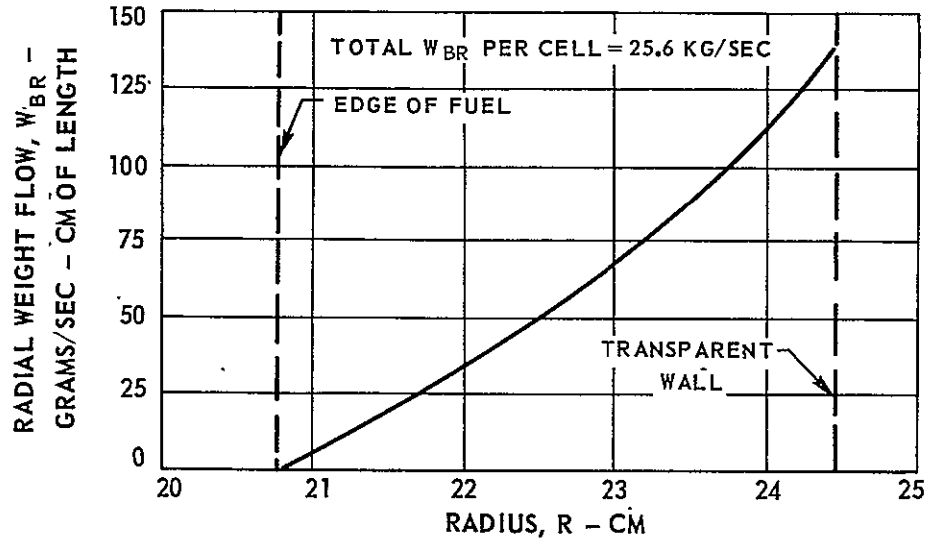

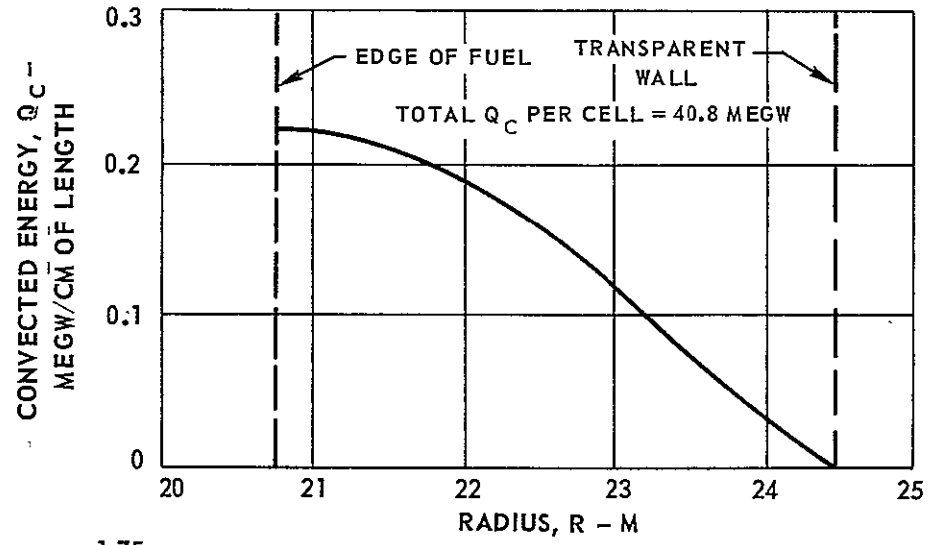

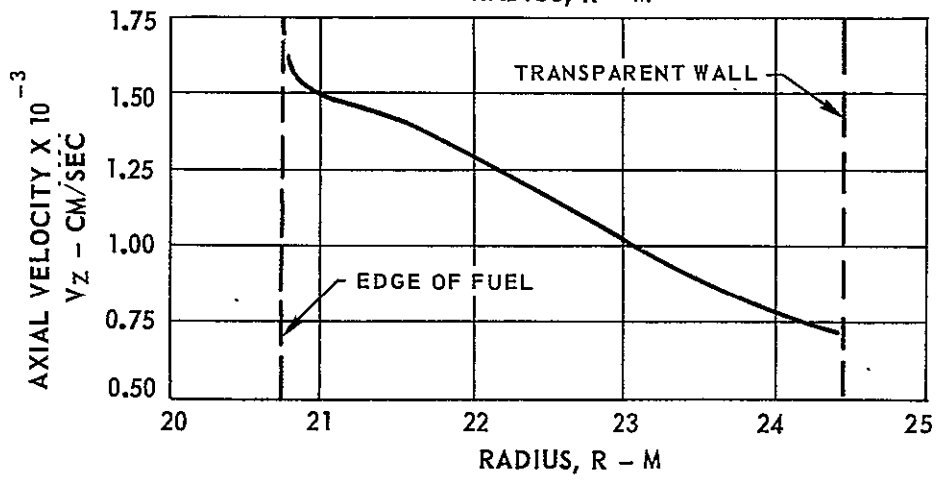

RADIAL WEIGHT FLOW, CONVECTED ENERGY AND AXIAL VELOCITY DISTRIBUTIONS IN BUFFER REGION FOR REFERENCE ENGINE SEEDED WITH 0.1 ATM NO/O_2

AXIAL PRESSURE DROP, ΔP_Z = 1.33 ATM

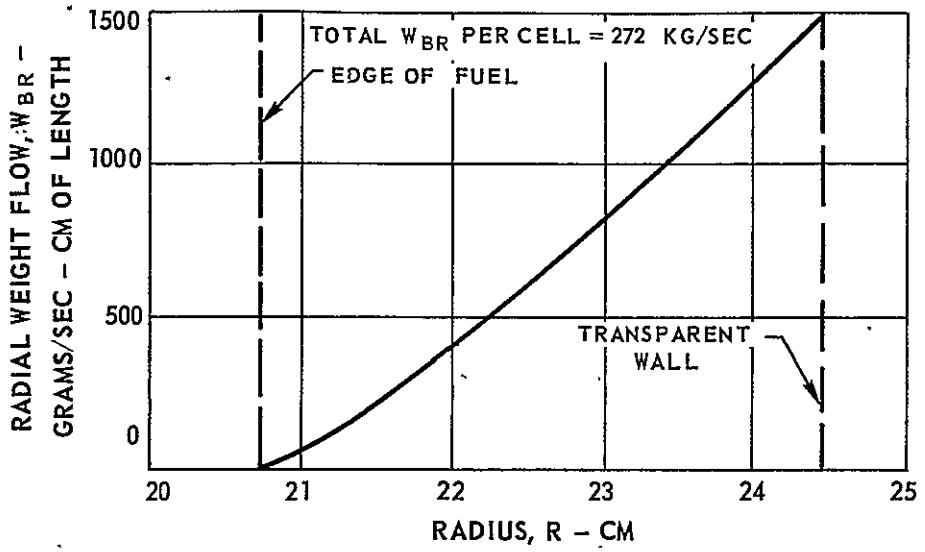

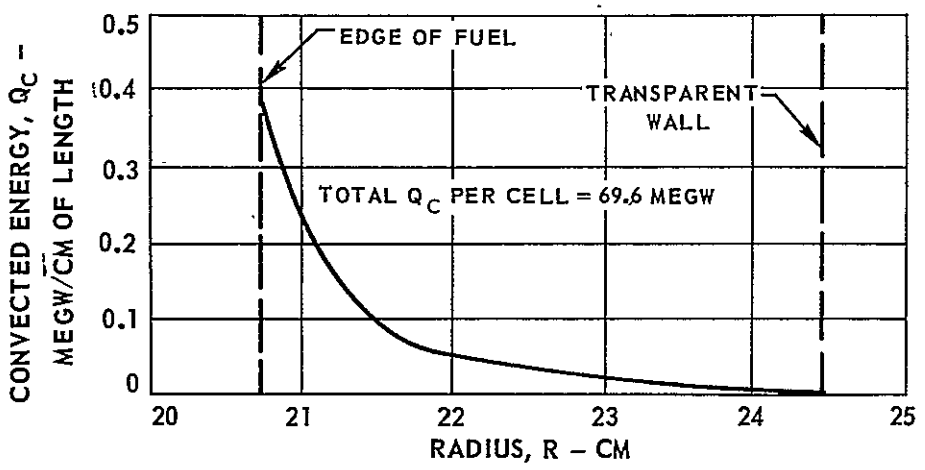

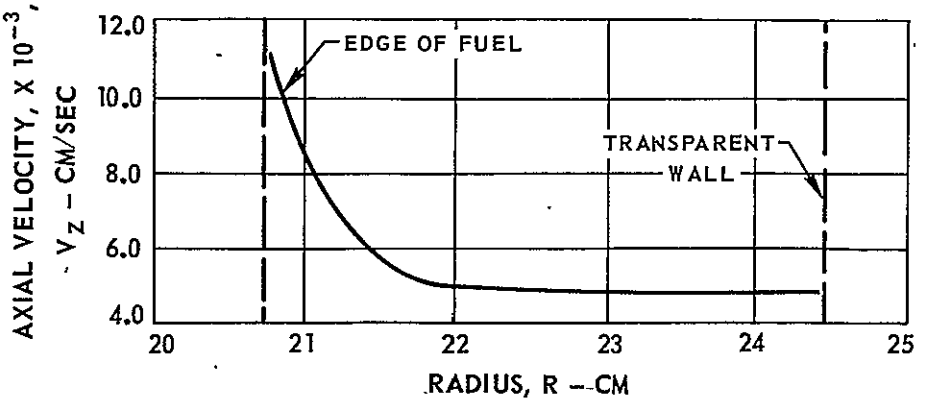

RADIAL WEIGHT FLOW, CONVECTED ENERGY AND AXIAL VELOCITY DISTRIBUTIONS IN BUFFER REGION FOR REFERENCE ENGINE SEEDED WITH 1.0 ATM NO/O_2

AXIAL PRESSURE DROP, ΔP_Z = 40.7 ATM

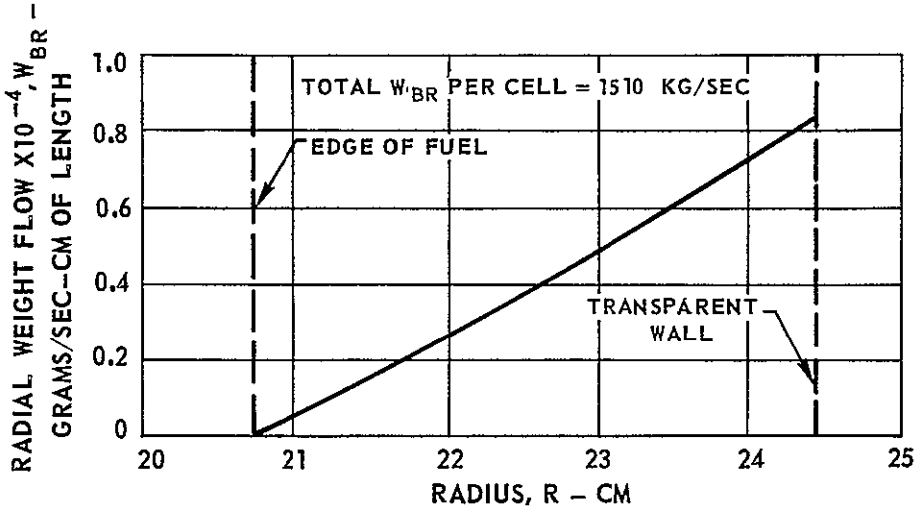

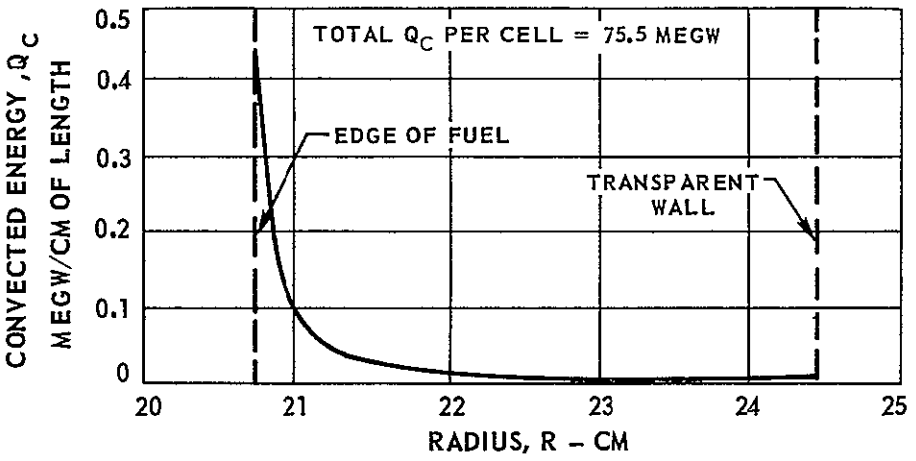

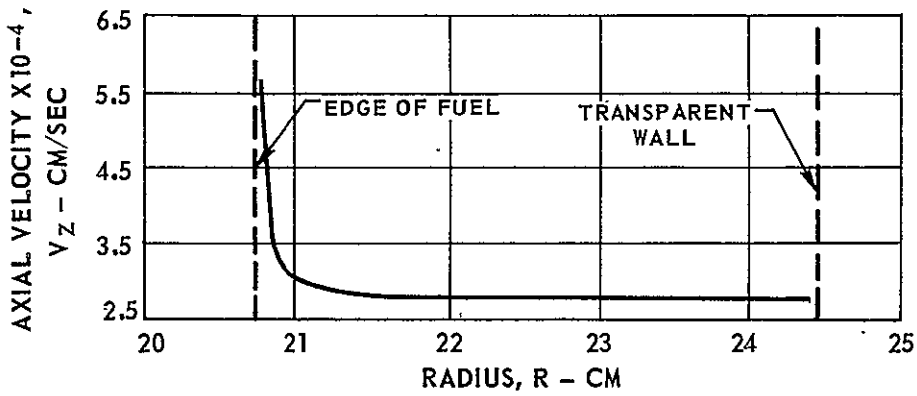

VARIATION OF TOTAL BUFFER GAS WEIGHT FLOW WITH TEMPERATURE AT EDGE OF TRANSPARENT WALL FOR VARIOUS NO/O_2 SEED PARTIAL PRESSURES

SEE FIG. 31 FOR CORRESPONDING BUFFER REGION TEMPERATURE DISTRIBUTIONS WHEN $T_{TW} \cong 1100$ DEG K

SEE FIGS. 39, 40, AND 41 FOR CORRESPONDING RADIAL WEIGHT FLOW, CONVECTED ENERGIES, AND AXIAL VELOCITY DISTRIBUTIONS WHEN $T_{TW} \cong 1100$ DEG K

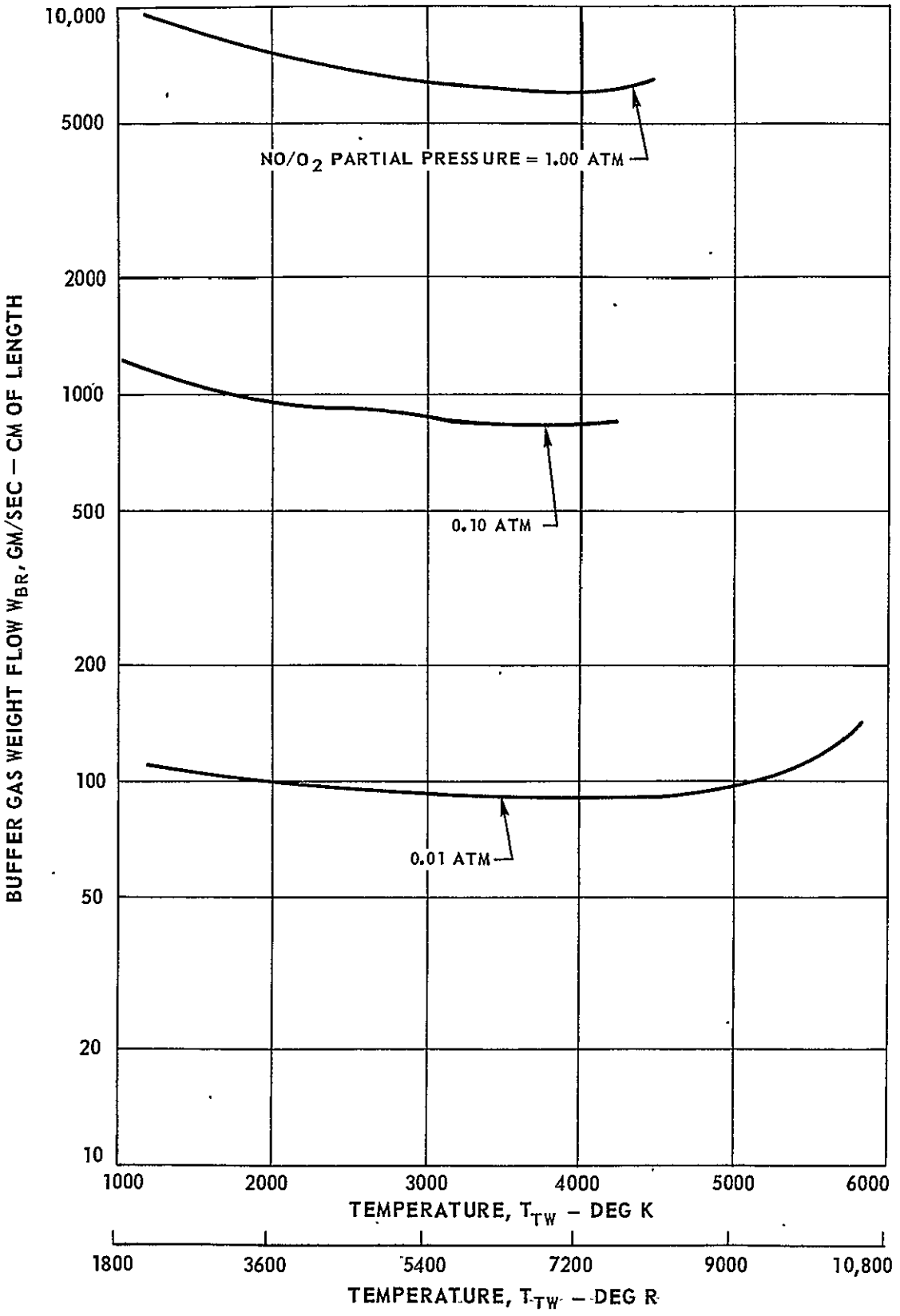

VARIATION OF REQUIRED AXIAL DYNAMIC PRESSURE IN BUFFER REGION TO REMOVE RADIANT ENERGY ABSORBED IN BUFFER GAS WITH VARIOUS NO/O_2 SEED PARTIAL PRESSURES

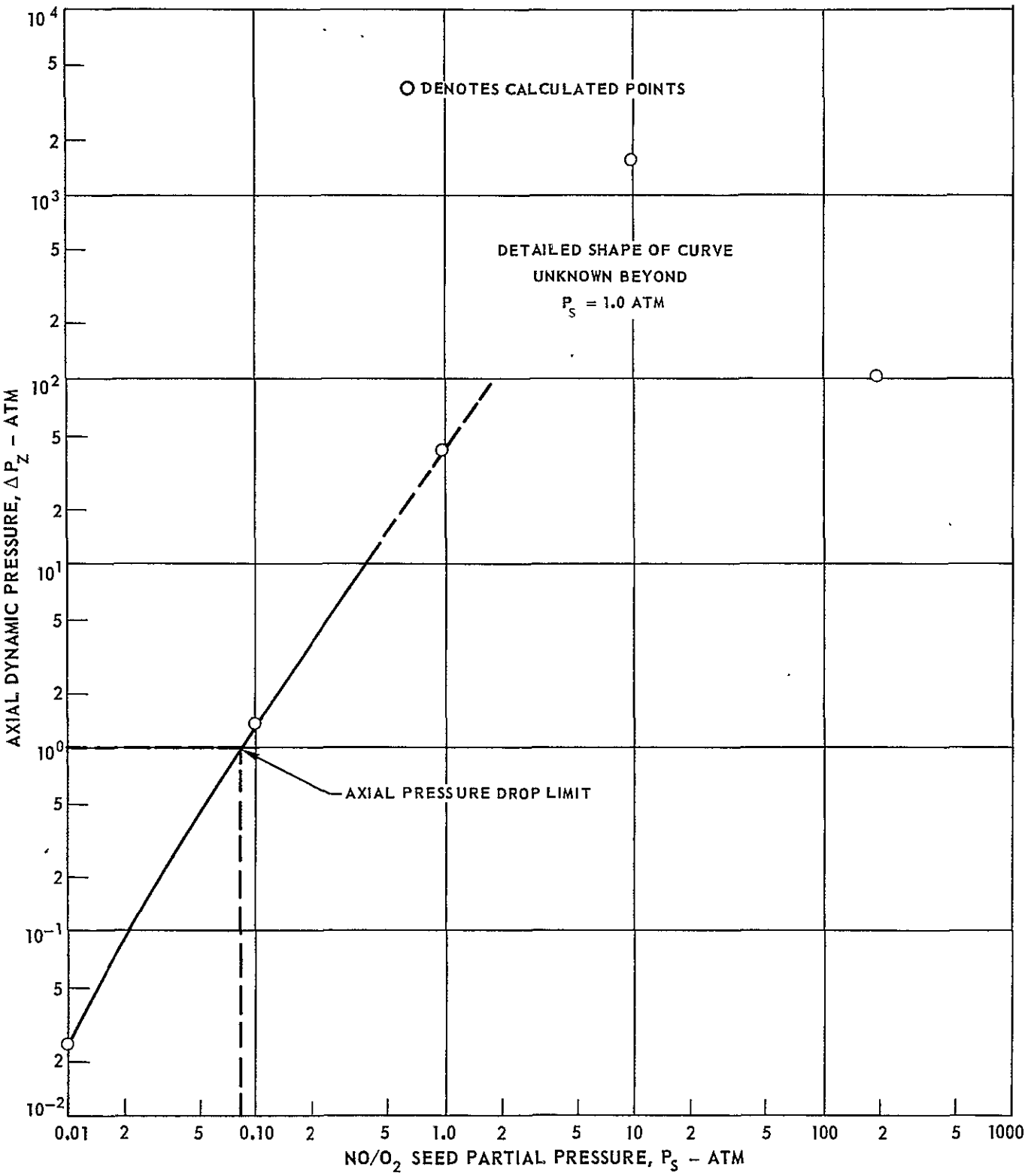

VARIATION OF CONVECTED ENERGY DENSITY IN BUFFER REGION NEAR EDGE OF FUEL WITH NO/O_2 SEED PARTIAL PRESSURE

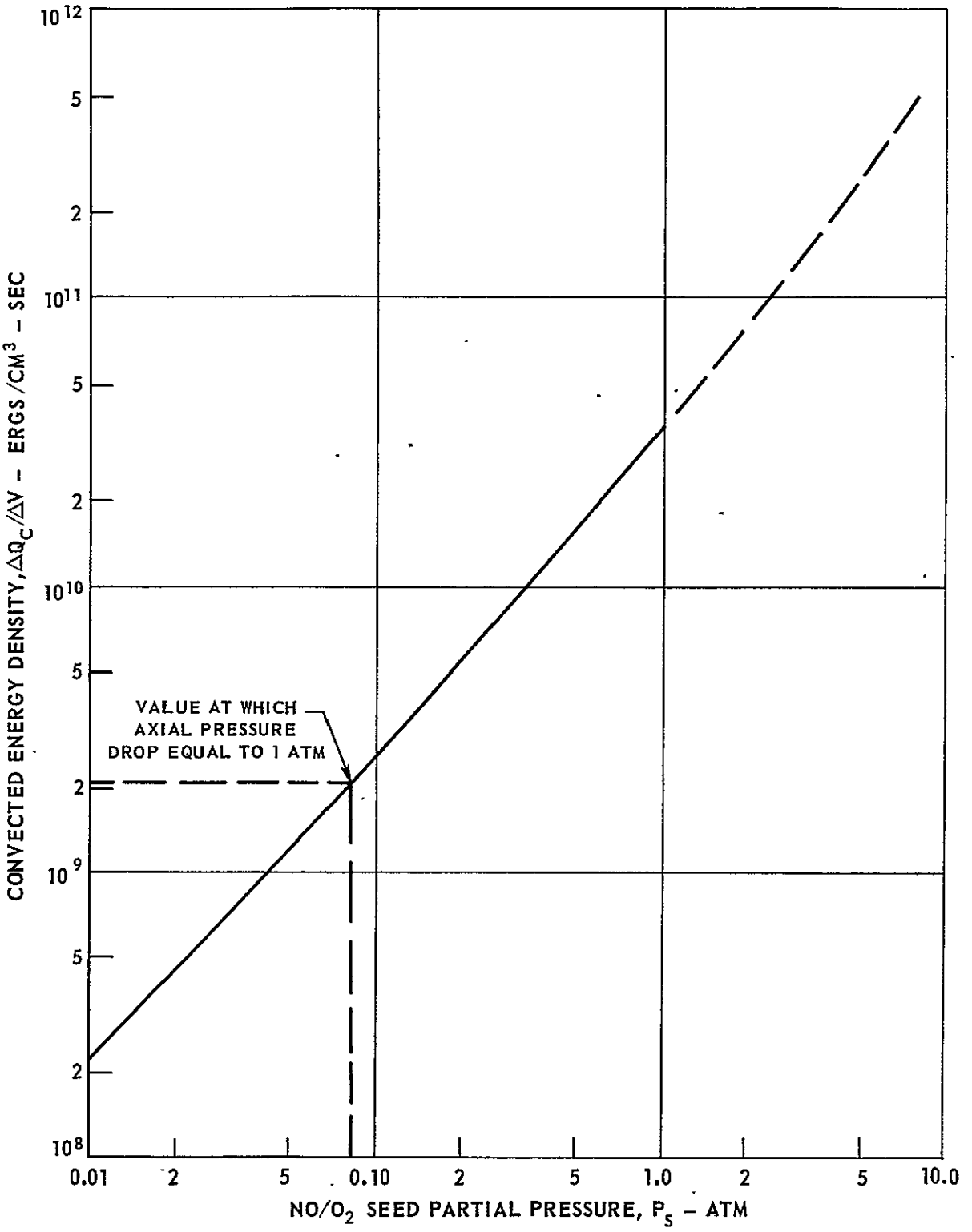

FIG. 45

VARIATION OF ENERGY FRACTIONS WITH NO/O_2 SEED PARTIAL PRESSURE FOR RADIANT HEAT LOADS IN BUFFER REGION AND BeO AND SiO_2 TRANSPARENT WALLS

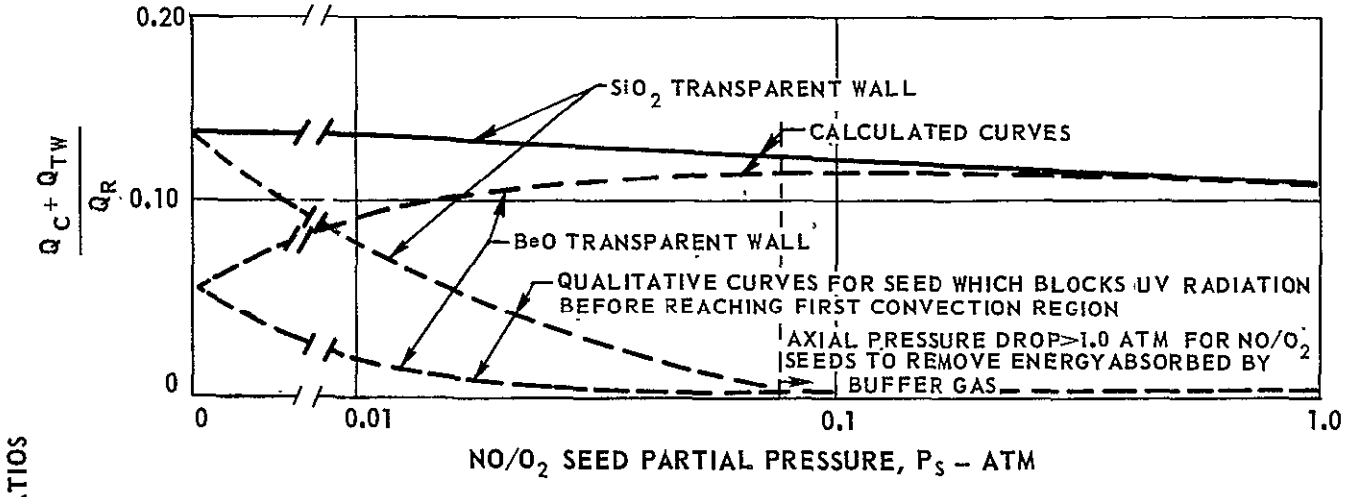

ENERGY DEPOSITION RATIOS

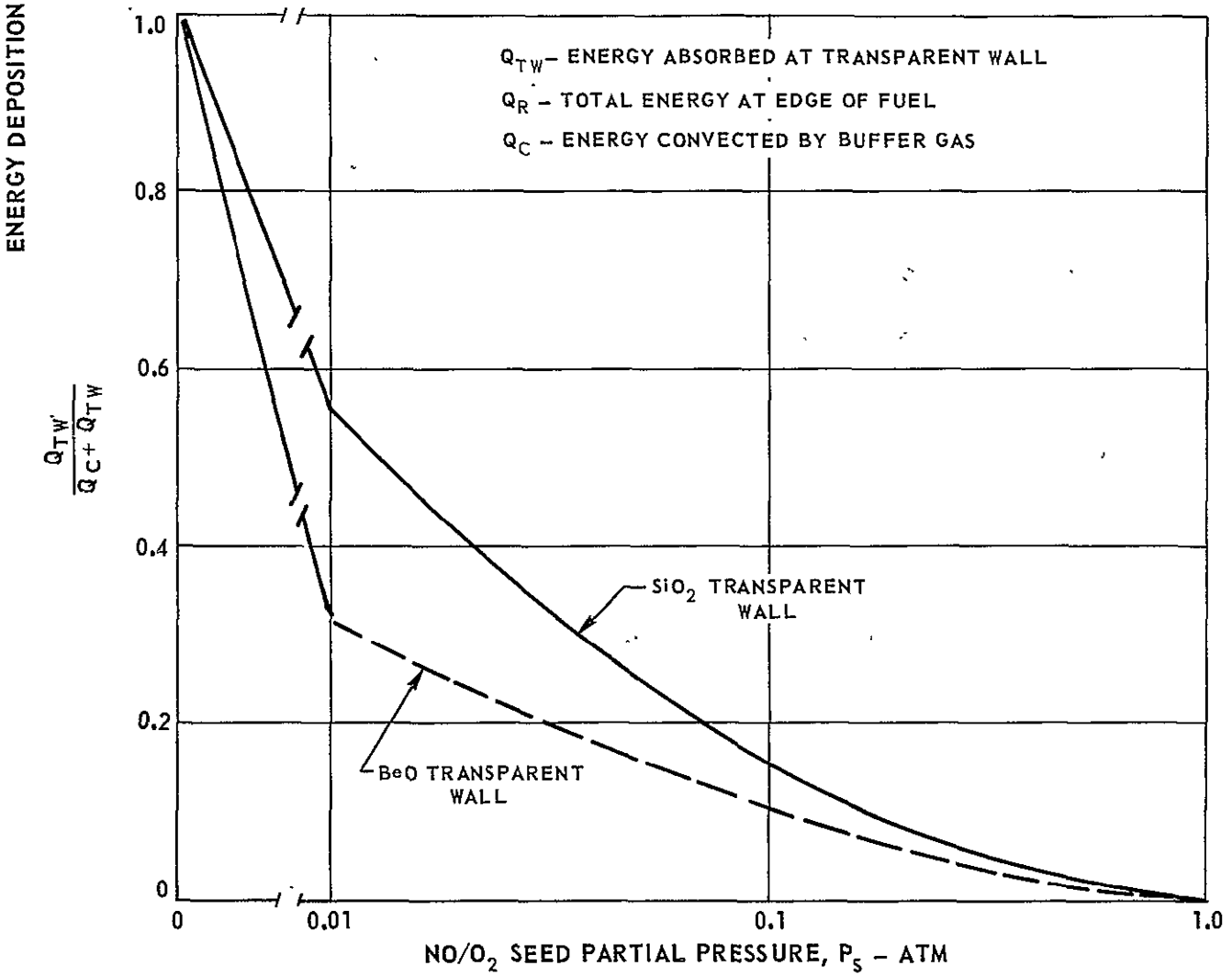

DISTRIBUTION LIST

NASA/AEC	Copy No.
Mr. Milton Klein Space Nuclear Systems Office U. S. Atomic Energy Commission Washington, D. C. 20545	1
Mr. F. C. Schwenk Space Nuclear Systems Office U. S. Atomic Energy Commission Washington, D. C. 20545	2
Dr. Karlheinz Thom Space Nuclear Systems Office U. S. Atomic Energy Commission Washington, D. C. 20545	3
Mr. M. Gruber Space Nuclear Systems Office U. S. Atomic Energy Commission Washington, D. C. 20545	4
Mr. R. F. Dickson Director of Technical Division Space Nuclear Systems Office c/o Nevada Operations Office U. S. Atomic Energy Commission Las Vegas, Nevada	5
U. S. Atomic Energy Commission Headquarters Library, Reports Section Mail Station G-017 Washington, D. C. 20545	6
Atomic Energy Commission Division of Technical Information Extension P. O. Box 62 Oak Ridge, Tennessee	7
Mr. John Marchaterre Argonne National Laboratory 9700 South Cass Avenue Argonne, Illinois	8

Copy No.

Mr. L. P. Hatch 9
Brookhaven National Laboratory
Upton, Long Island, New York 11101

Los Alamos Scientific Laboratory 10
P. O. Box 1663
Los Alamos, New Mexico 87544
Attention: N Division

Mr. Keith Boyer 11
N Division
Los Alamos Scientific Laboratory
Los Alamos, New Mexico 87544

Mr. T. R. Cotter 12
Los Alamos Scientific Laboratory
Los Alamos, New Mexico 87544

Dr. R. D. Cowan 13
Los Alamos Scientific Laboratory
Los Alamos, New Mexico 87544

Dr. Douglas Balcomb 14
N-5
Los Alamos Scientific Laboratory
P. O. Box 1663
Los Alamos, New Mexico 87544

Dr. William Kirk 15
Los Alamos Scientific Laboratory
P. O. Box 1663
Los Alamos, New Mexico 87544

Mr. John D. Orndoff 16
N Division
Los Alamos Scientific Laboratory
Los Alamos, New Mexico 87544

Dr. L. J. Radziemski 17
Los Alamos Scientific Laboratory
Los Alamos, New Mexico 87544

Copy No.

Dr. D. W. Steinhaus 18
Los Alamos Scientific Laboratory
Los Alamos, New Mexico 87544

Dr. T. F. Stratton 19
Los Alamos Scientific Laboratory
Los Alamos, New Mexico 87544

Mr. E. A. Franco-Ferreira 20
Metals & Ceramics Division
Oak Ridge National Laboratory
P. O. Box X
Oak Ridge, Tennessee 37831

Mr. A. P. Fraas 21
Oak Ridge National Laboratory
P. O. Box Y
Oak Ridge, Tennessee 37831

Dr. John J. Keyes, Jr. 22
Reactor Division
Oak Ridge National Laboratory
P. O. Box Y
Oak Ridge, Tennessee 37831

Mr. P. Patriarca 23
Oak Ridge National Laboratory
P. O. Box X
Oak Ridge, Tennessee 37831

NASA Headquarters 24
Washington, D. C. 20546
Attention: New Technology Representative, Code UT

NASA Headquarters 25
Washington, D. C. 20546
Attention: OART

National Aeronautics and Space Administration 26
Office of Scientific and Technical Information
Washington, D. C. 20546
Attention: AFSS-LL

	Copy No.
National Aeronautics and Space Administration Washington, D. C. 20546 Attention: Office of Technical Information and Educational Programs, Code ETL	27
NASA Scientific and Technical Information Facility (2 copies) Post Office Box 33 College Park, Maryland 20740	28 29
Mr. Richard J. Wisniewski, Code RX Office of Advanced Research and Technology NASA Headquarters 1520 H Street, NW Washington, D. C. 20546	30
Mr. A. E. Gessow NASA Headquarters Office of Advanced Research and Technology Washington, D. C. 20546	31
Mr. R. W. Ziem (RPS) National Aeronautics and Space Administration Washington, D. C. 20546	32
Mr. H. Hornby NASA Ames Research Center Mission Analysis Division Moffett Field, California 94035	33
Dr. W. L. Love NASA Ames Research Center Magnetoplasmadynamics Branch Mail Stop N-229-2 Moffett Field, California 94035	34
Dr. Chul Park NASA Ames Research Center Magnetoplasmadynamics Branch Mail Stop N-299-2 Moffett Field, California 94035	35

Copy No.

Mr. Jerome Deerwester 36
Advanced Concepts and Mission Division
NASA Ames Research Center
Moffett Field, California 94035

NASA Goddard Space Flight Center 37
Glenn Dale Road
Greenbelt, Maryland
Attention: Librarian

Jet Propulsion Laboratory/CAL TECH 38
4800 Oak Grove Drive
Pasadena, California 91103
Attention: Library Section 111-113

Mr. D. R. Bartz 39
Manager, Research and Advanced Concepts Section
Propulsion Division
Jet Propulsion Laboratory
Pasadena, California 91103

Dr. Clifford J. Heindl 40
Building 180-805
Jet Propulsion Laboratory
4800 Oak Grove Drive
Pasadena, California 91103

Dr. Robert V. Meghreblian 41
Jet Propulsion Laboratory
4800 Oak Grove Avenue
Pasadena, California 91103

Mr. L. E. Newlan 42
Chief, Reports Groups
Jet Propulsion Laboratory
4800 Oak Grove Drive
Pasadena, California 91103

Copy No.

Mr. Gary R. Russell 43
Jet Propulsion Laboratory
California Institute of Technology
4800 Oak Grove Drive
Pasadena, California 91103

National Aeronautics and Space Administration 44
Langley Research Center
Langley Air Force Base
Virginia
Attention: Library

Dr. F. Allario 45
National Aeronautics & Space
Administration
Langley Research Center
Langley Station
Hampton, Virginia 23365

Dr. R. V. Hess 46
National Aeronautics & Space
Administration
Langley Research Center
Langley Station
Hampton, Virginia 23365

Mr. R. A. Lucht 47
National Aeronautics & Space
Administration
Langley Research Center
Langley Station
Hampton, Virginia 23365

Major R. C. Chaplin, AFSC/STLO 48
NASA-Lewis Research Center
21000 Brookpark Road
Cleveland, Ohio 44135

Copy No.

Dr. J. C. Evvard 49
Associate Director
Mail Stop 3-5
NASA-Lewis Research Center
21000 Brookpark Road
Cleveland, Ohio 44135

Dr. Richard W. Patch 50
Nuclear Systems Division
Mail Stop 106-1
NASA-Lewis Research Center
21000 Brookpark Road
Cleveland, Ohio 44135

Mr. Robert G. Ragsdale 51
Nuclear Systems Division
Mail Stop 106-1
NASA-Lewis Research Center
21000 Brookpark Road
Cleveland, Ohio 44135

Mr. Frank E. Rom 52
Nuclear Systems Division
Mail Stop 106-1
NASA-Lewis Research Center
21000 Brookpark Road
Cleveland, Ohio 44135

National Aeronautics and Space Administration 53
Manned Spacecraft Center
P. O. Box 1537
Houston, Texas
Attention: Library

National Aeronautics and Space Administration 54
George C. Marshall Space Flight Center
Huntsville, Alabama 35812
Attention: Library

Mr. Ronald J. Harris 55
Chief, Planetary & Nuclear Systems Group
Advanced Systems Office R-AS
George C. Marshall Space Flight Center
Huntsville, Alabama 35812

DOD	Copy No.
Dr. U. Bauder Thermomechanics Research Lab Department of the Air Force Aerospace Research Lab (OAR) Wright-Patterson AFB, Ohio 45433	56
Col. W. Jakomis Department of the Air Force Aerospace Research Lab (OAR) Wright-Patterson AFB, Ohio 45433	57
Dr. H. Schrade Thermomechanics Research Lab Department of the Air Force Aerospace Research Lab (OAR) Wright-Patterson AFB, Ohio 45433	58
Mr. Erich E. Soehngen, Director Thermomechanics Research Lab Code ARN Aerospace Research Lab Wright-Patterson AFB, Ohio 45433	59
Lt. B. Turman Thermomechanics Research Lab Department of the Air Force Aerospace Research Lab (OAR) Wright-Patterson AFB, Ohio 45433	60
Dr. Hans von Ohain Aerospace Research Lab (ARD-1) Wright-Patterson AFB, Ohio 45433	61
Mr. E. C. Perkins AUL (AUL3T-7143) Maxwell Air Force Base Alabama	62
Dr. Charles J. Bridgman Associate Professor of Physics Air Force Institute of Technology Wright-Patterson AFB, Ohio 45433	63

Copy No.

Captain E. N. Kemler 64
Office of Research Analysis
Holloman Air Force Base
New Mexico

Dr. J. F. Masi (SREP) 65
Department of the Air Force
Air Force Office of Scientific Research
1400 Wilson Boulevard
Arlington, Virginia 22209

Mr. L. J. Edwards 66
Air Force Rocket Propulsion Laboratory
Edwards AFB, California 93523

Mr. G. Sayles (RPRRA) 67
Air Force Rocket Propulsion Laboratory
Edwards AFB, California 93523

HQ-SAMSO (SMAAP/Capt. Yepp) 68
Air Force Unit Post Office
Los Angeles Air Force Station
California 90045

AFSC (SCTD) 69
Andrews Air Force Base
Washington, D. C.

Commander 70
AFSC
Foreign Technology Division
Wright-Patterson AFB, Ohio 45433
Attention: RTD (TD-E3b)

Aerospace Corporation 71
P. O. Box 95085
Los Angeles, California 90045
Attention: Library-Documents

Dr. Robert F. Trapp 72
Chief, Research Division
Weapons Evaluation and Control Bureau
Arms Control and Disarmament Agency
320 21st Street, NW
Washington, D. C. 20451

	Copy No.
Mr. J. E. Jackson DDR&E (OAP) Washington, D. C.	73
DDR&E (WSEG) Washington, D. C. Attention: OSD	74
Dr. Theodore B. Taylor Defense Atomic Support Agency The Pentagon Washington, D. C. 20301	75
Mr. Philip G. Berman Defense Intelligence Agency The Pentagon, Attn: DIAST-2C2 Washington, D. C. 20301	76
Dr. Robert H. Fox Institute for Defense Analysis 400 Army Navy Drive Arlington, Virginia 22202	77
Dr. W. N. Podney Institute for Defense Analysis 400 Army Navy Drive Arlington, Virginia 22202	78
Superintendent U. S. Naval Postgraduate Naval Academy Monterey, California	79
Mr. George T. Lalos U. S. Naval Ordnance Laboratory White Oaks, Silver Springs Maryland 20900	80
Naval Plant Representative Office c/o UAC Pratt & Whitney Aircraft Division East Hartford, Connecticut 06108 Attention: Mr. R. F. Parslow	81

Copy No.

The Rand Corporation
1700 Main Street
Santa Monica, California 90406 — 82

Mr. E. C. Gritton
The Rand Corporation
1700 Main Street
Santa Monica, California 90406 — 83

Mr. Ben Pinkel
The Rand Corporation
1700 Main Street
Santa Monica, California 90406 — 84

OTHERS

Dr. J. W. Hilborn
Reactor Physics Branch
Advanced Projects & Reactor Physics Division
Atomic Energy of Canada Limited
Chalk River, Ontario, Canada — 85

National Aeronautics and Space Council
Attention: W. E. Berg
Executive Office of the President
Washington, D. C. 20502 — 86

Dr. Charles Beckett
Heat Division
National Bureau of Standards
Washington, D. C. — 87

Mr. Frederick C. Durant, III
Assistant Director, Astronautics
National Air Museum
Smithsonian Institute
Washington, D. C. 20560 — 88

INDUSTRY	Copy No.
Aerojet-General Corporation P. O. Box 1947 Sacramento, California 95809 Attention: Technical Information Office	89
Mr. William J. Houghton Department 7830, Building 2019A2 Aerojet-General Corporation P. O. Box 15847 Sacramento, California 95813	90
Mr. Joseph J. Peterson Aerojet-General Corporation Department 700, Building 2019A2 P. O. Box 15847 Sacramento, California 95813	91
Mr. W. L. Snapp Aerojet-General Corporation 20545 Center Ridge Road Cleveland, Ohio 44116	92
Dr. J. J. Stewart Department 7040, Building 2019A2 Aerojet-General Corporation Sacramento, California 95813	93
Florence Walsh, Librarian Aerojet-General Corporation 11711 South Woodruff Avenue Downey, California	94
Mr. D. F. Vanica Aerojet Nuclear Systems Company Department 7020, Building 2019A2 P. O. Box 15847 Sacramento, California 95813	95

Copy No.

Mr. Michael J. Monsler 96
AVCO-Everett Research Laboratory
2385 Revere Beach Parkway
Everett, Massachusetts 02149

Dr. Richard Rosa 97
AVCO-Everett Research Laboratory
2385 Revere Beach Parkway
Everett, Massachusetts 02149

Mr. Jerrold M. Yos 98
AVCO Corporation
Research & Advanced Development Division
201 Lowell Street
Wilmington, Massachusetts 01887

Bell Aerosystems 99
Box 1
Buffalo, New York
Attention: T. Reinhardt

Mr. R. R. Barber 100
Boeing Company
Aerospace Division
P. O. Box 3707
Seattle, Washington 98124

Mr. J. A. Brousseau 101
Chief, Propulsion Systems Technology
Mail Stop 47-18
The Boeing Company
Seattle, Washington 98124

Mr. Richard W. Carkeek 102
The Boeing Company
P. O. Box 3868
Mail Stop 85-85
Seattle, Washington 98124

Dr. Jacob B. Romero 103
The Boeing Company
Mail Stop 84-66
Kent, Washington

Copy No.

Chrysler Corporation — 104
Defense Operations Division
Box 757
Detroit 31, Michigan

Mr. Arthur Sherman — 105
Computer & Applied Sciences, Inc.
9425 Stenton Avenue
Philadelphia, Pennsylvania 19118

Dr. Robert W. Bussard — 106
Corporation Chief Scientist
CSI Corporation
1801 Avenue of the Stars
Suite 934
Los Angeles, California 90067

Dr. Ralph S. Cooper — 107
Donald W. Douglas Laboratories
2955 George Washington Way
Richland, Washington 99352

Dr. D. E. Knapp — 108
Donald W. Douglas Laboratories
2955 George Washington Way
Richland, Washington 99352

Dr. R. J. Holl — 109
Missiles & Space Systems Division
Douglas Aircraft Company
Santa Monica, California 90405

Dr. Kurt P. Johnson — 110
Advanced Space Technology, A2-263
Douglas Missiles & Space Systems Division
Santa Monica, California 90405

Mr. J. L. Waisman — 111
Douglas Aircraft Company
Santa Monica, California 90405

Copy No.

General Atomics Division 112
General Dynamics Corporation
P. O. Box 1111
San Diego, California 92112

Mr. Louis Canter 113
General Dynamics/Astronautics
Technical Library
San Diego, California 92112

Mr. John Peak 114
General Atomics Division
General Dynamics Corporation
P. O. Box 608
San Diego, California 92112

Dr. John Romanko, Staff Scientist 115
Y-128, Building 197
General Dynamics
Ft. Worth Division, Box 740
Ft. Worth, Texas 76101

General Electric Company 116
MSVD Library Documents Group, RM 3446
3198 Chestnut Street
Philadelphia, Pennsylvania 19101

General Electric Company 117
Cincinnati, Ohio 45215
Attention: Technical Information Center

Mr. Carmen B. Jones 118
H63 - General Electric Company
North I-75
Cincinnati, Ohio 45215

Copy No.

Dr. S. M. Scala 119
Manager, Theoretical Fluid Physics Section
General Electric Company
Space Sciences Laboratory
P. O. Box 8555
Philadelphia, Pennsylvania 19101

Mr. J. W. Stephenson 120
General Electric Company, NMPO
P. O. Box 15132
Cincinnati, Ohio 45215

R. R. Blackwell 121
Allison Division
General Motors Corporation
P. O. Box 24013
Indianapolis, Indiana 46206

Mr. David Mallon 122
Allison Division
General Motors Corporation
2355 S. Tibbs Avenue
Indianapolis, Indiana 46206

Dr. Jerry Grey 123
Grey-Rad Corporation
12 Station Drive
Princeton, New Jersey 08540

Mr. M. O. Friedlander 124
Engineering Library, Plant 5
Grumman Aircraft Engineering Corporation
Bethpage, Long Island, New York

Mr. Thomas N. Delmer 125
Gulf General Atomic, Inc.
P. O. Box 608
San Diego, California 92112

Copy No.

Dr. J. F. Kunze, Manager — 126
Operations & Analysis
Idaho Test Station
Idaho Nuclear Corporation
P. O. Box 1845
Idaho Falls, Idaho 83401

Dr. J. W. Morfitt, Manager — 127
Idaho Test Station
Idaho Nuclear Corporation
P. O. Box 1845
Idaho Falls, Idaho 83401

Isotopes — 128
Nuclear Systems Division
110 West Timonium Road
Timonium, Maryland 21093
Attention: Library

Miss Belle Berlad, Librarian — 129
Lockheed Propulsion Company
P. O. Box 111
Redland, California

Mr. Holmes F. Crouch — 130
Lockheed Missiles & Space Company
Space System Division, Dept. 62-90, Building 104
Sunnyvale, California 94408

Mr. Maxwell Hunter — 131
Department 50-01, Building 102
Lockheed Missiles & Space Company
P. O. Box 504
Sunnyvale, California 94408

Dr. Larry Kaufman — 132
Director of Research
Manlabs, Inc.
21 Erie Street
Cambridge, Massachusetts 02139

Copy No.

Mr. J. J. Norton 133
Marquardt Corporation
16555 Saticoy Street
Van Nuys, California

Mr. W. H. Morita 134
North American Aviation, Inc.
Space & Information Systems Division
12214 Lakewood Boulevard
Downey, California

North American Aviation, Inc. 135
Space & Information Systems Division
12214 Lakewood Boulevard
Downey, California
Attention: Technical Information
Center (L. M. Foster)

Professor Abraham Hyatt 136
North American Rockwell Corporation
Aerospace & Systems Group
1700 E. Imperial Highway
El Segundo, California 90246

Dr. A. G. Randol III 137
Nuclear Fuel Services
Wheaton Plaza Building
Wheaton, Maryland 20902

Rocketdyne 138
6633 Canoga Park, California 91303
Attention: Library, Dept. 596-306

Mr. C. C. Bennett 139
Rocketdyne
P. O. Box 552
Canoga Park, California 91303

Copy No.

Dr. S. V. Gunn 140
Rocketdyne
6633 Canoga Avenue
Canoga Park, California 91303

Space Technology Laboratories 141
One Space Park
Redondo Beach, California 90277
Attention: STL Technical Library Doc.
Acquisitions

Mr. Merle Thorpe 142
TAFA Division
Humphreys Corporation
180 North Main Street
Concord, New Hampshire 03301

Thompson Ramo Wooldridge 143
23555 Euclid Avenue
Cleveland, Ohio
Attention: Librarian

Mr. Walter F. Krieve 144
Building S
TRW Systems
One Space Park
Redondo Beach, California 90278

Dr. D. W. Drawbaugh 145
Astronuclear Laboratory
Westinghouse Electric Corporation
Pittsburgh, Pennsylvania 15236

Mr. Jack Felchtner 146
Westinghouse Research Labs
Churchill Borough
Pittsburgh, Pennsylvania 15285

Mr. M. R. Keller 147
Westinghouse Electric Corporation
Astronuclear Laboratory
Pittsburgh, Pennsylvania 15200

Copy No.

Mr. F. McKenna
Astronuclear Laboratory
Westinghouse Electric Corporation
P. O. Box 10864
Pittsburgh, Pennsylvania 15236 — 148

Dr. Jack Ravets
Westinghouse Astronuclear Laboratory
P. O. Box 10864
Pittsburgh, Pennsylvania 15236 — 149

Dr. Henry Stumpf
Astronuclear Laboratory
Westinghouse Electric Corporation
Pittsburgh, Pennsylvania 15236 — 150

Mr. Y. S. Tang
Westinghouse Electric Corporation
Astronuclear Laboratory
Pittsburgh, Pennsylvania 15200 — 151

UNIVERSITIES

Dr. John Hanlin
College of Engineering
Auburn University
Auburn, Alabama 36833 — 152

Dr. Ken Pell
College of Engineering
Auburn University
Auburn, Alabama 36833 — 153

Dr. C. C. Chang
Head, Space Sciences & Applied Physics
Catholic University of America
Washington, D. C. 20017 — 154

Professor Robert A. Gross
School of Engineering & Applied Science
Columbia University
New York, New York 10027 — 155

Copy No.

Professor Chieh Ho
Division of Nuclear Science
Room 287, Mudd Building
Columbia University
New York, New York 10027
156

Professor Terence Cool
Thermal Engineering Department
Cornell University
Ithaca, New York 14850
157

Dr. G. H. Miley
Ward Reactor Laboratory
Department of Applied Physics
College of Engineering
Cornell University
Ithaca, New York 14850
158

Dr. Franklin K. Moore, Head
Thermal Engineering Department
Cornell University
Ithaca, New York 14850
159

Mr. D. J. Strobel
Department of Thermal Engineering
Cornell University
208 Upson Hall
Ithaca, New York 14850
160

Dr. Joseph Clement
Nuclear Engineering Department
Georgia Institute of Technology
Atlanta, Georgia 30332
161

Dr. W. R. Jacobs
School of Nuclear Engineering
Georgia Institute of Technology
Atlanta, Georgia 30332
162

Professor Clyde Orr, Jr.
Chemical Engineering Department
Georgia Institute of Technology
Atlanta, Georgia 30332
163

Copy No.

Dr. S. V. Shelton
School of Nuclear Engineering
Georgia Institute of Technology
Atlanta, Georgia 30332 — 164

Dr. J. Richard Williams
Nuclear Engineering Department
Georgia Institute of Technology
Atlanta, Georgia 30332 — 165

Dr. Glenn A. Greathouse
P. O. Box 332
Ormond Beach, Florida 32074 — 166

Dr. Peter Chiarulli
Head, Mechanics Department
Illinois Institute of Technology
Chicago, Illinois 60616 — 167

Dr. Andrew Fejer
Head, Mechanical & Aerospace Engineering Department
Illinois Institute of Technology
Chicago, Illinois 60616 — 168

Dr. Zalman Lavan
Illinois Institute of Technology
M.A. E. Department
Technology Center
Chicago, Illinois 60616 — 169

Dr. T. P. Torda
Illinois Institute of Technology
M.A. E. Department
Technology Center
Chicago, Illinois 60616 — 170

Dr. Herbert Weinstein
Chemical Engineering Department
Illinois Institute of Technology
Chicago, Illinois 60616 — 171

Copy No.

Dr. B. D. Goracke 172
Massachusetts Institute of
Technology
Aeronautics & Astronautics
Room 37-371
Cambridge, Massachusetts 02139

Professor Elias P. Gyftopoulos 173
Room 24-109
Massachusetts Institute of Technology
Cambridge, Massachusetts 02139

Dr. A. Javan 174
Massachusetts Institute of Technology
Cambridge, Massachusetts 02139

Professor J. L. Kerrebrock 175
Room 33-115
Massachusetts Institute of Technology
Cambridge, Massachusetts 02139

Dr. W. S. Lewellen 176
Room 33-119
Massachusetts Institute of Technology
Cambridge, Massachusetts 02139

Professor Edward Mason 177
Room NW12
Massachusetts Institute of Technology
Cambridge, Massachusetts 02139

Dr. C. K. W. Tam 178
Aeronautics & Astronautics
Massachusetts Institute of Technology
Room 37-371
Cambridge, Massachusetts 02139

Dr. Friedwardt Winterberg 179
Nevada Southern University
Professor of Physics
Director of Laboratory for Space Research
Desert Research Institute
Las Vegas, Nevada 89109

Copy No.

Dr. H. A. Hassan 180
Department of Mechanical Engineering
North Carolina State University
Raleigh, North Carolina 27607

Dr. H. E. Unger 181
Technological Institute Engineering Sciences
Northwestern University
Evanston, Illinois 60201

Professor E. P. Wigner 182
Department of Physics
Princeton University
Princeton, New Jersey 08540

Dr. Bruce A. Reese, Director 183
Jet Propulsion Center
Mechanical Engineering Department
Purdue University
Lafayette, Indiana 47907

Professor M. J. Zucrow 184
Atkins Professor of Engineering
Mechanical Engineering Department
Purdue University
Lafayette, Indiana 47907

Mr. H. J. Ramm 185
606 Larrymore Drive
Manchester, Tennessee 37355

Professor C. N. Shen 186
Rensselaer Polytechnic Institute
Troy, New York

Dr. W. H. Bostick 187
Stevens Institute of Technology
Hoboken, New Jersey 07030

Dr. A. V. Grosse 188
Research Institute of Temple University
4150 Henry Avenue
Philadelphia, Pennsylvania 19144

Copy No.

Dr. George Nelson 189
University of Arizona
Nuclear Engineering Department
Tucson, Arizona 85721

Professor H. C. Perkins 190
Energy, Mass & Momentum Transfer Laboratory
Aerospace & Mechanical Engineering Department
University of Arizona
Tucson, Arizona 85721

Dr. Paul T. Bauer 191
Research Institute
University of Dayton
300 College Park
Dayton, Ohio 45409

Professor Ron Dalton 192
Department of Nuclear Engineering
University of Florida
Gainesville, Florida 32601

Dr. D. Keefer 193
Aerospace Engineering Department
Department of Nuclear Engineering Sciences
University of Florida
Gainesville, Florida 32601

Dr. M. J. Ohanian 194
Department of Nuclear Engineering Sciences
University of Florida
Gainesville, Florida 32601

Professor Rafael Perez 195
Nuclear Engineering Department
University of Florida
Gainesville, Florida 32601

Dr. Richard T. Schneider 196
202 Nuclear Sciences Building
Department of Nuclear Engineering Sciences
University of Florida
Gainesville, Florida 32601

Copy No.

Professor Glen J. Schoessow 197
Department of Nuclear Engineering Sciences
202 Nuclear Sciences Building
University of Florida
Gainesville, Florida 32601

Dr. Robert Uhrig 198
Chairman, Department of Nuclear Engineering
University of Florida
Gainesville, Florida 32601

Dr. T. Ganley 199
College of Engineering
University of Illinois
Urbana, Illinois 61801

Dr. G. C. Guyot 200
College of Engineering
University of Illinois
Urbana, Illinois 61801

Mr. Paul E. Thiess 201
Direct Energy Conversion
Nuclear Engineering Program
University of Illinois
Urbana, Illinois 61801

Dr. J. T. Verden 202
Gaseous Electronic Lab
University of Illinois
Urbana, Illinois 61801

Dr. K. Almenas 203
Department of Chemical Engineering
University of Maryland
College Park, Maryland 20742

Dr. D. Tidman 204
Institute for Fluid Mechanics
University of Maryland
College Park, Maryland 20742

Copy No.

Dr. T. D. Wilkerson 205
Institute for Fluid Dynamics and Applied Mathematics
University of Maryland
College Park, Maryland 20742

Dr. J. N. Davidson 206
University of Michigan
Ann Arbor, Michigan 48103

Dr. D. H. Timmons 207
Nuclear Engineering Program
University of Missouri
Columbia, Missouri 65201

Mr. L. H. Bettenhausen 208
Department of Nuclear Engineering
Reactor Facility
University of Virginia
Charlottesville, Virginia 22901

Mr. Stanley Bull 209
Assistant Professor
Nuclear Engineering Program
University of Missouri
Columbia, Missouri 65201